Nanosenzor temeljen na grafenu za detekciju plinova

Anđelić, Nikola

UNIVERSITY OF RIJEKA
FACULTY OF ENGINEERING

Nikola Anđelić

NANOSENSOR BASED ON GRAPHENE SHEET FOR DETECTION OF GAS MOLECULES

DOCTORAL THESIS

Thesis Supervisor: Prof. D. Sc. Marko Čanađija
Thesis Co-supervisor: Prof. D. Sc. Zlatan Car

Rijeka, 2021.

SVEUČILIŠTE U RIJECI
TEHNIČKI FAKULTET

Nikola Anđelić

NANOSENZOR TEMELJEN NA GRAFENU ZA DETEKCIJU PLINOVA

DOKTORSKA DISERTACIJA

Mentor: prof. dr. sc. Marko Čanađija
Komentor: prof. dr. sc. Zlatan Car

Rijeka, 2021.

Thesis supervisor:	Prof. D. Sc. Marko Čanađija, University of Rijeka, Faculty of Engineering
Thesis Co-supervisor:	Prof. D. Sc. Zlatan Car, University of Rijeka, Faculty of Engineering

This doctoral thesis was discussed on _____ at the University of Rijeka, Croatia, Faculty of Engineering in front of the following Evaluation Committee:

1. Assist. Prof. D. Sc. Marino Brčić, University of Rijeka, Faculty of Engineering, Croatia
2. Prof. D. Sc. Zdenko Tonković, University of Zagreb, Faculty of Mechanical Engineering and Naval Architecture, Croatia
3. Prof. D. Sc. Dražan Kozak, University of Slavonski Brod, Mechanical Engineering Faculty in Slavonski Brod, Croatia

“I think it's much more interesting to live not knowing than to have answers which might be wrong. I have approximate answers and possible beliefs and different degrees of uncertainty about different things, but I am not absolutely sure of anything and there are many things I don't know anything about, such as whether it means anything to ask why we're here. I don't have to know an answer. I don't feel frightened not knowing things, by being lost in a mysterious universe without any purpose, which is the way it really is as far as I can tell.”

Richard P. Feynman

Dedication

The development of this thesis took a very long time. During my Ph.D. studies, there are a lot of people who supported and encourage me to finish what I've started. First of all, I want to thank my parents who supported me through my education and my wife who had tremendous patience and support during thesis development.
I also want to thank my mentor, prof. dr. sc. Marko Canadija who introduced me to the field of nanotechnology, helped me to change the field of my Ph.D. studies, had tremendous patience during the thesis development and constructive suggestions that helped in shaping this thesis.
Special thanks to my co-mentor prof. dr. sc. Zlatan Car who offered me a research/teaching assistant job at his department and who encouraged me to find practical implementation in my Ph.D. investigation and implement Artificial Intelligence methods to the thesis. Without him, this thesis would not materialize.
This thesis is dedicated to all those people.

Abstract

Nanosensor for mass detection is a mechanical sensor that from an experimental and theoretical point of view proved to be an excellent candidate in the detection of atoms and molecules. The basic idea of these sensors is the frequency shift method. This method is based on the difference between the resonant frequency of graphene with and without added mass in the form of atoms and molecules bonded with carbon atoms.
Natural frequencies, and the frequency shift method used in atom/molecule detection will be analyzed using molecular dynamics (MD) simulation and non-local theory of plates. Numerical results obtained using MD (natural frequencies) will be used to adjust the non-local parameter value in non-local thin plate theory in such a way that the frequency from non-local thin plate theories will be equated with the natural frequencies from MD by modifying the non-local parameter value. This will create a dataset for the implementation of the genetic programming algorithm in order to establish approximate correlations between the input data (mechanical characteristics of graphene, graphene dimensions, temperature and natural frequencies) with the output data (non-local parameter).
Since most sensors have a specified temperature range and pressure at which the sensor can perform detection, it was initially assumed that graphene as a sensing element of the nanosensor can detect gas molecules in the range from 233.15 to 313.15 K and at a pressure in the range from 0 to 1 bar. Before investigating the natural frequencies of one layer of graphene, the mechanical and thermodynamic characteristics of this material were obtained using MD with REBO interatomic potential. The obtained mechanical and thermodynamic parameters were used in non-local thin plate theory to determine the natural frequencies of single-layer graphene as well as to examine the influence of temperature, pressure, size of single-layer graphene, a variation of non-local graphene parameter on natural frequencies caused by gas molecules attached to the surface of the single-layer graphene.
MD was used to determine the natural frequencies of single-layer graphene, to examine the influence of single-layer graphene size on natural frequencies as well as the absolute and relative frequency shift caused by attached gas molecules to the central single-layer graphene atom using the displacement excitation method. The results of the above ana-

lyzes in MD and non-local thin plate theory showed that the size of single-layer graphene has the greatest influence on the natural frequencies of single-layer graphene while temperature has a very small influence on the natural frequencies. MD simulations with NPT ensemble showed that the pressure oscillates a lot during equilibration and vibration simulation and therefore the influence of pressure was omitted from further analyzes. Analyzes performed using non-local thin plate theory also showed that the value of the non-local parameter has a large influence on the natural frequencies of single-layer graphene. The mechanical characteristics are temperature dependent and with increasing temperature, the value of these parameters with small oscillations gradually decreases. Physical data of 3 molecules of chemical weapons of mass destruction were used to investigate the possibility of detecting gas molecules using non-local theory and MD. Both theories have shown that single-layer graphene can detect gas molecules using the absolute and relative frequency shift method.

One of the main shortcomings of the non-local theory of elasticity is the unknown value of the non-local parameter, and in many studies, its value is set in a certain range. Therefore, the goal is to apply a genetic programming algorithm to obtain a symbolic expression by which its value could be determined. The genetic programming algorithm was used to determine the symbolic expression that would connect the input values with mathematical functions, namely: mechanical parameters (modulus of elasticity, shear modulus, Poisson's coefficients and dimensions of graphene), operating conditions (temperature) and natural frequencies obtained by MD with a non-local parameter that represents the output value of this symbolic expression. For a genetic programming algorithm to be able to generate a symbolic expression, it is necessary to develop a data set on which the algorithm can be trained and tested. Three temperatures (233.15, 273.15, and 313.15 K) were used to generate the data set in MD and non-local theory. Graphene models with dimensions ranging from $20\times$ 10 to 40×20 nm were used for these simulations. The natural frequencies obtained by MD were used as reference values for tuning the natural frequencies in non-local theory so that the value of the non-local parameter was adjusted so that the natural frequency value was equivalent to those frequencies obtained in MD. Based on the obtained parameters using MD and non-local theory, a set of data was created which was used in the genetic programming algorithm to determine the equation by which the value of the non-local parameter could be determined. The equation for determining the value of a non-local parameter was chosen based on the highest achieved value of the R^2 correlation coefficient which is equal to 0.9688. The obtained equation for determining the non-local parameter value was used to determine the absolute and relative frequency shift caused by the mass attached in the center of the fully clamped graphene sheet. The obtained results were compared with the averaged absolute and relative frequency shift

values obtained using MD simulations. The results of the comparison showed that on average the calculated values of absolute and relative frequency shift are 5 % lower than those obtained using MD simulations.

Keywords: genetic programming algorithm, graphene, nanosensor, non-local thin plate theory, molecular dynamics.

Sažetak

Nanosenzor za detekciju mase mehanički je senzor koji se s eksperimentalnog i teoretskog stajališta pokazao kao odličan kandidat u detekciji atoma i molekula. Osnovna ideja ovih senzora je metoda frekvencijskog pomaka. Ova metoda bazira se na razlici između vlastite frekvencije grafena sa i bez dodane mase u obliku vezanih atoma/molekula s ugljikovim atomima.

Vlastite frekvencije i metoda frekvencijskog pomaka koja se koristi u detekciji atoma/ molekula bit će analizirana primjenom molekularne dinamike (MD) i ne-lokalne teorije elastičnosti. Numerički rezultati koji su dobiveni primjenom MD-a (vlastite frekvencije) koristiti će se za podešavanje ne-lokalnog parametra u ne-lokalnoj teoriji tankih ploča na način da će se frekvencija iz ne-lokalne teorije tankih ploča izjednačiti s vlastitim frekvencijama iz MD-a podešavanjem ne-lokalnog parametra. Na taj način stvoriti će se skup podataka za implementaciju algoritma genetskog programiranja u cilju uspostavljanja približne korelacije između ulaznih podataka (mehaničke karakteristike grafena, dimenzija grafena, temperature i vlastitih frekvencija) s izlaznim podacima (ne-lokalnim parametrom).

Budući da većina senzora ima specificiran temperaturni raspon i tlak na kojima senzor može vršiti detekciju inicijalno je pretpostavljeno da grafen kao osjetni element nanosenzora može detektirati molekule plina u rasponu od 233.15 do 313.15 K te na tlaku u rasponu od 0 do 1 bar. Prije istraživanja vlastitih frekvencija jednog sloja grafena određene su mehaničke i termodinamičke karakteristike tog materijala primjenom MD-a s REBO međuatomskim potencijalom. Dobiveni mehanički i termodinamički parametri korišteni su u ne-lokalnoj teoriji tankih ploča u cilju određivanja vlastitih frekvencija jednoslojnog grafena kao i ispitivanja utjecaja temperature, tlaka, veličine jednoslojnog grafena, varijacije ne-lokalnog parametra na vlastite frekvencije kao i određivanje apsolutnog i relativnog frekvencijskog pomaka koje uzrokuju molekule plina pričvršćene za površinu jednoslojnog grafena. MD-a se koristila za određivanje vlastitih frekvencija jednoslojnog grafena, ispitivanje utjecaja veličine jednoslojnog grafena na vlastite frekvencije kao i apsolutnog i relativnog frekvencijskog pomaka kojeg uzrokuju pričvršćene molekule plina na centralni atom jednoslojnog grafena primjenom metode pobude brzine koristeći

prethodno spomenuti međuatomski potencijal.
Rezultati prethodno navedenih analiza u MD-u i ne-lokalnoj teoriji tankih ploča pokazali su da veličina jednoslojnog grafena ima najveći utjecaj na vlastite frekvencije jednoslojnog grafena dok temperatura ima jako mali utjecaj na vlastite frekvencije. MD simulacije s NPT ansamblom pokazale su da tlak dosta oscilira tijekom ekvilibracije i simulacije vibracija te je stoga utjecaj tlaka izostavljen iz daljnjih analiza. Analize provedene primjenom ne-lokalne teorije tankih ploča također su pokazale da vrijednost ne-lokalnog parametra ima veliki utjecaj na vlastite frekvencije jednoslojnog grafena. Mehaničke karakteristike ovisne su o temperaturi i sa porastom temperature vrijednost tih parametara se uz male oscilacije, samnjuje. Za ispitivanje mogućnosti detekcije molekula plina primjenom ne-lokalne teorije i MD-a korišteni su fizikalni podatci 3 molekule kemijskog oružja za masovno uništenje. Obje teorije su pokazale da jednoslojni grafen može detektirati molekule plina primjenom metode apsolutnog i relativnog frekvencijskog pomaka.
Jedan od glavnih nedostataka ne-lokalne teorije elastičnosti je nepoznata vrijednost ne-lokalnog parametra te se u mnogim istraživanjima njegova vrijednost postavlja u određenom rasponu. Stoga je cilj primijeniti algoritam genetskog programiranja u cilju dobivanja simboličkog izraza pomoću kojeg bi se mogla odrediti njegova vrijednost. Algoritam genetskog programiranja korišten je za određivanje simboličkog izraza koji bi matematičkim funkcijama povezao ulazne vrijednosti i to: mehaničke parametre (module elastičnosti, modul smicanja, Poissonove koeficijente i dimenzije grafena), eksploatacijske uvjete (temperatura) te vlastite frekvencije dobivene pomoću MD-a s ne-lokalnim parametrom koji predstavlja izlaznu vrijednost ovog simboličkog izraza. Da bi algoritam genetskog programiranja mogao generirati simbolički izraz potrebno je razviti skup podataka na kojem će se algoritam moći trenirati i testirati. Za generiranje skupa podataka u MD-u i ne-lokalnoj teoriji korištene su tri temperature (233.15, 273.15 i 313.15 K). Za ove simulacije korišteni su modeli grafena čije su dimenzije u rasponu od 20×10 do 40×20 nm. Dobivene vlastite frekvencije pomoću MD-a korištene su kao referentne veličine za podešavanje vlastitih frekvencija u ne-lokalnoj teoriji tako da se podešavala vrijednost ne-lokalnog parametra s ciljem da vrijednost vlastitih frekvencija bude ekvivalentna onim frekvencijama dobivenim u MD-u. Na temelju dobivenih parametara pomoću MD-a i ne-lokalne teorije stvoren je skup podataka koji je korišten u algoritmu genetskog programiranja za određivanje jednadžbe pomoću koje bi se mogla odrediti vrijednost ne-lokalnog parametra. Jednadžba za određivanje vrijednosti ne-lokalnog parametra odabrana je na temelju najveće postignute vrijednosti R^2 korelacijskog koeficijenta od 0.9688. Dobivena jednadžba za određivanje ne-lokalnog parametra korištena je za određivanje apsolutnog i relativnog frekvencijskog pomaka koje uzrokuje masa pričvršćena u centru kompletno uklještenog grafena. Dobiveni rezultati uspoređeni su sa srednjim apsolutnim i relativnim

frekvencijskim pomakom koji su određeni pomoću MD simulacija. Rezultati usporedbe pokazali su da su u prosjeku izračunate vrijednosti apsolutnog i relativnog frekvencijskog pomaka 5% manje od onih dobivenih pomoću MD simulacija.

Ključne rječi: algoritam genetskog programiranja, grafen, nanosenzor, ne-lokalna teorija tankih ploča, molekularna dinamika.

Contents

1. Introduction

For a long time, in the science community, it was believed that two-dimensional crystals were thermodynamically unstable and could not exist [1, 2]. The theory states that the thermal fluctuations in two-dimensional crystal lattices would lead to the large displacement of atoms that are equal to interatomic distances at any finite temperature [3]. As the melting temperature of thin films rapidly decreases with decreasing thickness the material begins segregating into islands or decomposes at a thickness of dozens of atomic layers [4, 5]. This is the main reason why atomic mono-layers have been known as an integral part of three-dimensional structures and they were grown on top of mono-crystal with matching crystal lattices. In 2004 [6] single-layer graphene sheet was experimentally obtained. From that point on, graphene established itself as outstanding material for sensing applications due to its properties such as: high charge carrier mobility [7], high thermal conductivity [8], mechanical strength [9] and the slight inertness at room temperature [10]. Since the graphene sheet is essentially a surface, it enables analyte molecules to absorb and produce a change in its physical properties. The carbon-carbon bonds make it sensitive to a large variety of molecules, so graphene suffers from a lack of selectivity. However, these exceptional material properties have lead to the application of graphene-based sensors that are capable of detecting down to single-analyte molecules [10]. After the graphene sheet was experimentally obtained the other 2D nanomaterials were obtained such as: graphyne [11, 12], borophene [13, 14, 15, 16], germanene [17, 18, 19], silicene [20, 21], Si_2BN [22], stanene [23], phosphorene [24], antimonene [25], bismuthene [26, 27], molybdenite [28], hexagonal boron nitride [29] etc.

1.1 Experimental Investigation of Graphene Sheets

Based on its structural features, according to [30], there are three different types of graphene materials including pristine graphene (PG), graphene oxide (GO) and reduced graphene oxide (RGO). Each of these graphene materials has its own distinct sensing capabilities. Since its discovery there were numerous experimental attempts of its implementation as sensing material in physical, chemical and biological nanosensors.

1.1.1 Physical Sensors Based on Graphene Sheet

With the outstanding electronic properties, mechanical strength, and one atom thickness, graphene can be considered as sensing element of the nano-electro-mechanical sensor (NEMS), and these sensors are capable of detecting physical parameters such as pressure, mass, charge, electric potential, temperature and magnetic field. Today there are various successful implementations of graphene in the development of physical nanosensors such as graphene NEMS resonators, magnetic field, infrared (IR) and pressure sensors.
Graphene properties such as high stiffness, Young's modulus, and breaking strength result in very high resonant frequencies, which are in MHz and GHz or in some cases in THz range. This property paved the way for utilizing graphene as the building block of NEMS resonator. With the application of strain, the resonant frequency of the graphene sheet could be tuned [31]. One of the first fabrication of graphene NEMS was done using a mechanical exfoliation method where graphene was positioned on top of etched trenches [32]. The authors have experimentally measured the resonant frequencies of the single layer and multi-layered graphene sheets or in terms of material thickness from 0.3 up to 75 nm. One of the challenges was to measure the thickness of a single layer graphene sheet. For the nanomaterials with thickness greater, the 2 nm the non-contact mode atomic force microscope (AFM) can be utilized. To determine the thickness of graphene sheets and the number of graphene layers deposited on the SiO_2 substrate, the authors have utilized the Raman spectroscopy method. In Fig. 1.1 the schematic view, an optical image of a double-layer graphene sheet, Raman signal from a scan on the graphene sheet, an optical image of few layers, and a scanning electron microscope image of a few-layer graphene resonator are shown.

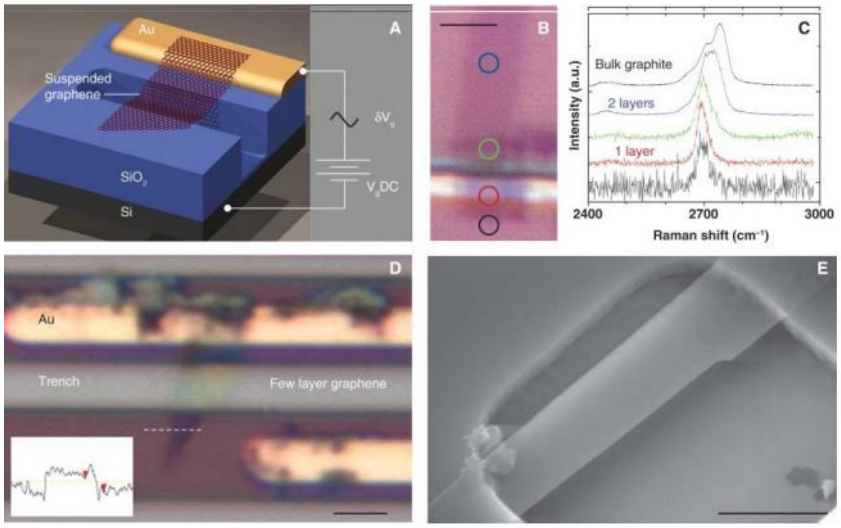

Figure 1.1: (A) Schematic view of graphene based resonator, (B) Optical image of a double layer graphene sheet where each colored circle corresponds to a point where Raman spectrum was measured. (C) Raman signal from a scan of the graphene piece. Each colored curve corresponds to the colored circle dot in (B), (D) Optical image of few-layer graphene suspended over a trench and containing a gold electrode and (E) scanning electron microscope image of the double layer graphene resonator [32].

All experimental investigations and measurements in [32] of graphene resonators where performed at room temperature and pressure of 1.33×10^{-9} bar. The resonators were actuated using electrical or optical modulation. The size of single layer graphene sheet is $1100 \times 1930 \times 0.3$ nm. The sheet is deposited over SiO_2 trench and generated resonant frequency of 70.5 MHz as shown in Fig. 1.2.

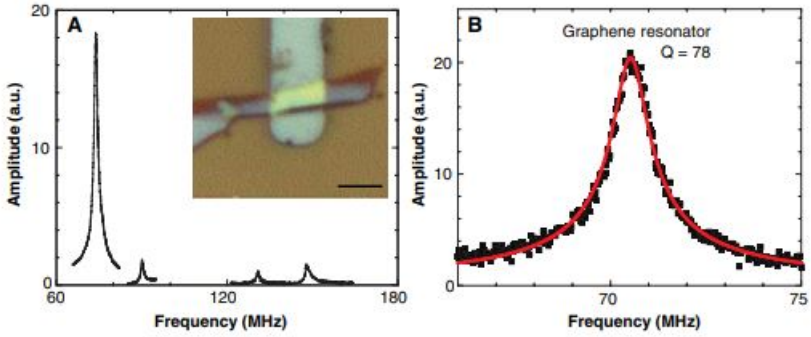

Figure 1.2: The amplitude versus frequency taken with optical drive for the fundamental mode of single-layer graphene resonator [32]

The main challenge in NEMS characterization, is to actuate and detect graphene motion. In order to perform the actuation and detection of graphene the electrical and optical method have been used [31, 33].
The basic principle of magnetic field sensors in detection of magnetic field is based on

Hall effect. According to [34], in high-density magnetic storage with nanomagnets the magnetic field sensor must be employed as close as possible to the magnetic field source. Generally the magnetic field decays exponentially as one moves away from the source.
Graphene can absorb mid-IR to ultraviolet wavelength range with almost flat absorption spectra due to its linear energy dispersion and zero bandgap. This characteristic makes graphene material suitable for optical detection applications. In [35] the graphene was utilized as infra red (IR) camera which was realized by incorporating a micro-mirror device that compressed IR imaging signal. The compressed signal was measured by the graphene detector in a series of measurements and later decompressed to reconstruct the image.
The graphene sheet is impermeable to all standard gases and can withstand pressure differences larger than 1 bar according to [36]. The impermeability of graphene makes it ideal for pressure sensor.

1.1.2 Chemical and Biological Sensors

Besides physical sensors, graphene could be utilized as a sensing element of chemical and biological sensors since the adsorbed molecules can strongly affect the physical properties including conductivity [10] and surface work function [37]. It was experimentally verified [10] that graphene could detect a single molecule from which it can be concluded that it possesses ultrahigh sensitivity.
So far a majority of developed graphene-based chemical and biological sensors are in the form of chemiresistor of chemical field-effect transistors (chem-FETs). In these type of sensors the conductivity is linearly changed with the number of absorbed analyte molecules. For specific analyte, the detection sensitivity depends on mobility of the carriers in graphene and type of substrate on which graphene is synthesized on or transferred to [38]. However, the experimental investigation [39] showed that graphene sensitivity could be tuned with back-gate utilization. Some of the applications of graphene sheet as sensing element of chemical and biological sensors are:

- gas and vapor sensors - used for detection of various analytes in gaseous and vapour phase analytes such as NO_2 [10, 39, 40, 41, 42], NH_3[10, 39, 41, 42], H_2O[10, 40], CO[10], CO_2[40], O_2[40] and C_2H_3N [43].
- pH sensors - first report [44] of successful implementation of epitaxial graphene-based pH sensor for detection in solution
- toxic heavy metal sensors - toxic heavy metals such as Cadmium (Cd), Mercury (Hg), Lead(Pb), Chromium (Cr) and Arsenic (Ar) have harmful effect on human health. Graphene [45] has been successfully implemented as sensing element for detection of mercury with detection limit of 10 ppm.

- hydrogen peroxide - molecule that is enzymatic product of many biological processes. RGO-chitosan composite film entrapped with hemoglobin molecules [46] showed better detection of hydrogen peroxide in comparison with conventional hydrogen peroxide sensors.

- glucose sensors - is important parameter in diabetics diagnosis. The detection of glucose could be realized using glucose oxidase (GO) as the mediator or recognition element. GO-RGO-chitosan modified electrode has been reported [47] successful in detection of glucose oxidase.

- nucleic acid sensor - the sensor capable of detection of nucleobases, nucleotides and DNAs. In detection of these biological compounds the RGO showed as promising candidate.The four nitrogenous bases of DNA (adenine, thymine, cytosine, and guanine) could be selectively detected with RGO due to different oxidation potentials as reported in [48].

- sensor for cancer protein marker - graphene based sensors have shown potential for detection various protein markers. One such implementation of graphene oxide (GO) is reported [49] in detection of anti-alpha-fetoprotein (AFP) that is cancer marker.

- dopamine, ascorbic acid (AA) and uric acid (UA) sensor - The absence of dopamine which is an important neurotransmitter, is indication of Parkinson's disease. Since its contraction is low (0.01-1 mM) and the possibility of error from AA and UA, present in higher concentration, can interfere with sensing of dopamine. Detection of low concentration in dopamine is an ideal task for graphene based sensors. The RGO composite electrode was able to detect dopamine [50].

- cholesterol and cellular detection - extremely important for medical purposes. The RGO-based sensor has been successfully applied for detection of cholesterol which works on amperometric property change [51].

1.1.3 Gas Sensing Using Graphene Sheet

As mentioned, there are three different types of graphene materials based on its structural properties and these are PG, GO and RGO. These graphene materials have its own distinct capabilities.

1.1.3.1 PG Gas Nanosensors

PG is a from of graphene that is pure and defect free. The chemical vapor deposition (CVD) growth methods are usually used for development of this graphene material. The first development and investigation of graphene sensors for gas sensing was reported in [52] using mechanical exfoliation. This sensor was micrometers in size and consisted of few PG layers. The sensor, placed in high vacuum environment, achieved a single NO_2 molecule detection. However in [53] the authors concluded that device fabrication procedure could cause possible contamination (chemical doping) which may lead to false results meaning high sensitivity of PG. They have also concluded that PG sensitivity is low. Using mechanical exfoliation procedure to develop few layers PG which was deposited on SiO_2/Si substrate, the authors in [54] were able to develop PG NO_2 gas nano-sensor. This nano-sensor showed high sensitivity of ~ 0.09 in response to 100 ppm NO_2 gas at room temperature. Extremely low detection limit of 158 parts-per-quadrillion (ppq) was reported in [55] for gas molecules including NO_2, NH_3, N_2O, O_2, SO_2, CO_2 and H_2O at room temperature. Low frequency noise spectrum measurement of PG was performed in [56] that was exposed to different gas vapors such as: tetrohydrofuran, methanol, acetonitrile, chloroform and air. The investigation showed that ethanol, methanol, tetrahydofuran, chloroform and acetonitrile modify the frequency spectra (unique gas signatures). In experimental investigation [57] the few-layer graphene developed using electrochemical exfoliation was exposed to CO_2 and LPG gas at room temperature. The chemiresistor exhibited detection limit of 3 ppm for CO_2 and 4 ppm for LPG. The CVD grown graphene on a smooth paper [58] showed detection limit of 300 parts per trillion (ppt) when exposed to NO_2 gas.

1.1.3.2 GO Gas Nanosensors

The chemical oxidation of graphite and reduction of resulting graphene oxide is one of the methods commonly used for graphene synthesis. The graphite oxide has similar structure of graphite with the exception of containing oxygen groups including hydroxyls, epoxies, carboxyl and lactones. The single or few layers are usually of graphite oxide are termed as GO and they are promising candidates for gas sensing. In order to optimize the sensing efficiency, the authors in [59] have developed sensing device utilizing single-layer GO flakes on standard 30 μm spaced interdigitated Pt electrodes and exposed to NO_2 gas. The results showed the sensitivity of 20 parts-per-billion (ppb). In [60] the GO nanosensor for detection of hydrogen gas was developed. The results showed good sensing response, fast response time and fast recovery time when exposed to hydrogen gas at room temperature. The successful implementation [61, 62] of the GO nanosensor with

propagated surface acoustic waves (SAW) in detection of H_2O and NO_2 in atmospheric conditions. In [63] the GO nanosensor was used in detection of tetrahydrofuran and chloroform in environment with extremely high humidity.

1.1.3.3 RGO Gas Nanosensors

The reduced graphene oxide (RGO) can be developed by removing the oxygen containing groups from GO. The quality of RGO is strongly dependent of GO reduction. When compared to PG the RGO has proved as better sensing material with properties such as conductivity, dispersibility in water and possibility of further modification. In [64] the RGO was used in detection of acetone, 2,4-dinitrotoulene (DNT), hydrogen cyanide (HCN), dymethyl methyl phosphonate (DMMP). The results showed that these chemical compounds could be detected at ppb concentrations within 10 s of exposed RGO. The RGO based nanosensor was used in [65] for detection of NH_3 and DNT. The results showed a decrease in resistance of $\sim 0.028\%$ in concentration of 52 ppb of DNT and 5 ppm NO_2 at elevated temperatures. The RGO gas nanosensor on paper substrate in [66] was used for detection of NO_2 and exhibited sensitivity to sub-ppm levels. Also the RGO was used for detection of H_2 [67, 68, 69].

1.2 Analytical Modeling of Graphene

Aside from experimental investigations which are complicated and expensive there are analytical approaches that could be used for modeling and studying graphene sheet as seen in Fig. 1.3. As seen from Fig. 1.3 there are vast number of methods which could be utilized in investigation of graphene sheets and their interaction with gas molecules. However, the most utilized methods in these investigations are Density functional theory (DFT), Molecular Dynamics (MD) Simulations and Non-local theory so the short literature overview of implementation of these methods will be given.

1.2.1 DFT Simulations of Graphene Sheet

The DFT investigations reported in [70, 71, 72, 73, 74] showed that PG, GO and RGO have potential in detecting gas molecules. One of first theoretical investigation [70] proved that total density of states of graphene is suitable for chemical sensing and explained experimentally obtained results in [10] regarding single molecule NO_2 detection with graphene. In [71] using DFT it was theoretically investigated the possibility of utilizing PG in detection of gas molecules such as H_2O, NH_3, CO, NO_2 and NO. The investigation showed that these gas molecules are physically absorbed on surface of PG. The investigation also

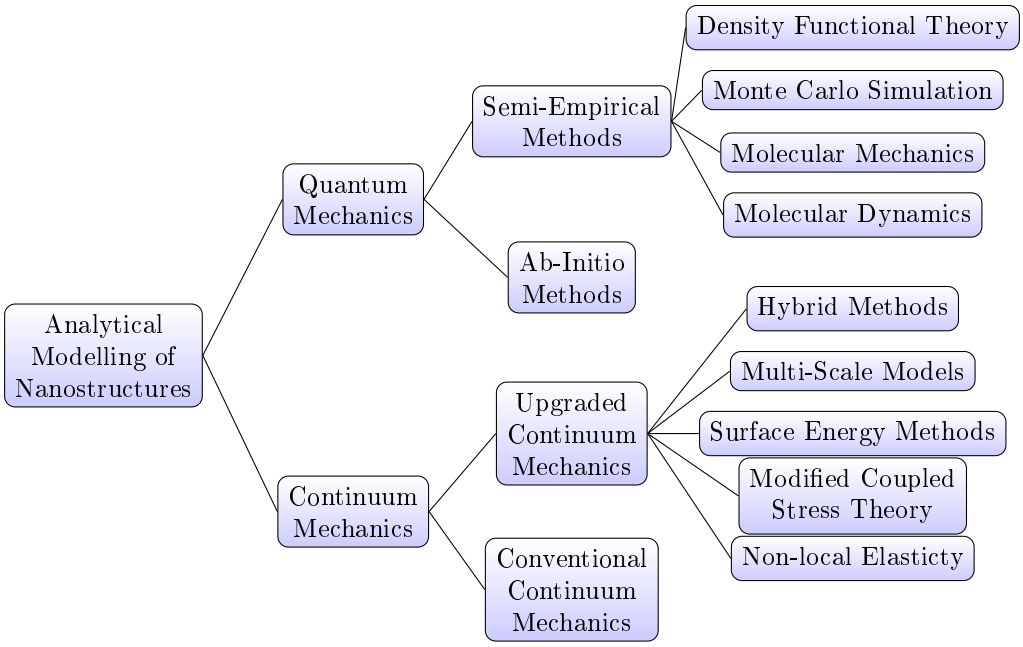

Figure 1.3: Graphical overview of analytical methods used for modeling of nanostructures.

showed that NO_2 and H_2O are electron acceptors while the CO and NH_3 are electron donors which is in agreement with the experimentally obtained results showed in [10]. In [72] absorption of hydrogen on PG flakes was analyzed using DFT. The absorption of NH_3 and other gas molecules of armchair-shaped PG was investigated in [75] using DFT, and showed that NH_3 strongly affects the electronic properties of PG. The theoretical investigation of graphene doped with B-, N- and Si-dopants in detection of H_2, H_2O, O_2, CO_2, CO, NO_2, SO_2, NH_3 and N_2 was reported in [76] and showed strong binding with aforementioned gas molecules. The Ti-doped graphene interactions with CO, NO, SO_2 and HCHO was compared with PG and nitrogen-doped graphene (NG) interaction capabilities towards the same gas molecule. This research [77] showed that Ti-doped graphene have enhanced interaction towards aforementioned gas molecules.

1.2.2 Molecular Dynamics Simulations of Graphene Sheets

The MD simulation method is less expensive than experimental investigations, and in comparison with continuum models, gives better insight into nanostructures but requires larger computational resources than continuum models. The motions of individual atoms within a system of N atoms in MD simulation could be modeled using Newtonian-based dynamics or Langevin-type stochastic dynamics if the initial positions and velocities of atoms are known. To obtain trajectories of molecules and atoms in the analyzed system

and see the evolution of the system in a specific time interval the numerical integration of Newton equations that describe the motion of each atom must be applied. The interaction between atoms in the system is defined by the interaction forces. These forces and potential energy are defined by molecular mechanics force fields. One disadvantage of the molecular simulation method, in general, is that these methods require larger computation resources because the system is described by a large number of differential equations which would be impossible to solve using consumer computational resources.
The application of single-layered graphene sheets as mass sensors in the detection of noble gases via a vibration analysis of graphenes is investigated using MD simulations [78]. The simulation results indicate the square graphene sheet with an area of 100 nm^2 achieved a mass sensor resolution of 10^{-6} fg, and that the mass sensitivity can be enhanced with a decrease in the graphene size. The potential of single-layered graphene sheets as nanosensors in the detection of noble gases through a wave propagation analysis is investigated using molecular dynamics simulations [79]. The simulation results also show that the resolution of a sensor made of the graphene sheet with a size of 3.62 nm $\times$15.03 nm can achieve an order of the impact rate of 10^{-7} fg/ps. The impact rate represents the amount of molecule mass (fg) that impacts the graphene sheet surface per ps. In [80] classical molecular dynamics simulations are performed to investigate the enhancement of the mass sensitivity and resonant frequency of graphene nanomechanical resonators that is achieved by driving them into the nonlinear oscillation regime. The mass sensitivity, as measured by the resonant frequency shift, is found to triple if the actuation energy is about 2.5 times the initial kinetic energy of the nanoresonator. Application of single-layered graphene sheets (SLGSs) as resonant sensors in the detection of ultra-fine nanoparticles (NPs) is investigated via molecular dynamics (MD), and non-local elasticity approaches. To take into consideration the effect of geometric nonlinearity, non-locality, and atomic interactions between SLGSs and NPs, a nonlinear non-local plate model carrying an attached mass-spring system is introduced and a combination of pseudo-spectral (PS) and integral quadrature (IQ) methods are proposed to numerically determine the frequency shifts caused by the attached metal NPs [81]. Despite the importance of biomolecules graphene interactions, a detailed understanding of the adsorption mechanism and features of biomolecules onto the surfaces of graphene is lacking. To address this, the authors have performed DFT and MD simulations exploring the adsorption geometries, adsorption energies, electronic band structures, adsorption isotherms, and adsorption dynamics of l-leucine (model biomolecule)/graphene composite system [82].

1.2.3 Non-local Theory Investigation of Graphene Sheets

The non-local theory of elasticity is upgraded continuum mechanics method and today is commonly used. This theory, unlike continuum mechanics theory, incorporates distant effects known as non-local effects. There are a number of papers [83, 84, 85] that theoretically analyzed graphene sheet used as a sensing element in NEMS resonators. In these papers the authors have analyzed the possibility of utilizing SLGS or DLGS as sensing elements of NEMS resonators in detection of attached molecules using absolute frequency shift method. The frequency equations for these systems are obtained using non-local plate theory. The absolute frequency shift method is based on difference in two resonant frequencies of the system where one resonant frequency is the frequency of the system without attached molecules and second one is resonant frequency of the system with attached molecules.

1.3 Challenges and Thesis Overview

Based on detailed overview of previous work in field of graphene nanosensors two hypothesis will be investigated in this thesis. First hypothesis is that the graphene sheet can be utilized as nanosensor element for detection of gas molecules based on frequency shift method using non-local plate theory and MD simulation. The second hypothesis is that the Genetic Programming algorithm can be used to obtain symbolic expressions which could calculate the non-local parameter using graphene sheet size, mechanical and thermodynamic parameters, and natural frequencies as input values. In order to investigate these two hypothesis the following challenges will be investigated and tackled in this thesis:

- Investigate the influence of graphene sheet size on its natural frequencies using MD simulations and non-local plate theory,
- Investigate the influence of pressure and temperature variation on natural frequencies of graphene sheets with and without attached mass using MD simulations and non-local plate theory,
- Investigate the influence of temperature, pressure, attached nanoparticle mass, and size of a graphene sheet on the non-local parameter,
- Tuning the non-local parameter value by equalizing natural frequencies obtained using non-local plate theory with those obtained using MD simulations, and

- Apply genetic programming algorithm in order to determine mathematical formulation using which approximate value of the non-local parameter could be determined.

In order to respond to the previously mentioned challenges, the structure of the doctoral dissertation was formed as follows:

- Chapter 2 - Properties of graphene material and gas molecules - The structural, and mechanical of graphene sheets will be described as well as physical properties of gas/vapor molecules that will be used in MD simulations and non-local plate theory,
- Chapter 3 - Simulation Methods - gives a short theoretical overview of MD simulations, and non-local plate theory that will be used in this thesis for determining mechanical and thermal properties, natural frequencies of graphene sheets.
- Chapter 4 - Artificial Intelligence (AI) Methods - short theoretical overview of genetic programming (GP) algorithm which will be used to obtain symbolic expression for the non-local parameter.
- Chapter 5 - Results of MD simulations - in this chapter the procedure and results for obtaining mechanical and thermodynamics parameters and natural frequencies of graphene sheets are described in detail,
- Chapter 6 - Results obtained using non-local plate theory - in this chapter, using non-local plate theory, the influence of temperature, pressure, graphene sheet size, type of boundary conditions, and the value of non-local parameter on natural frequencies of graphene sheet is described,
- Chapter 7 - Estimation of the Non-local Parameter of Graphene Sheet Nanosensor Using Genetic Programming Algorithm - in this chapter the dataset will be described which is obtained using MD simulation and non-local plate theory, and used in genetic programming algorithm to obtain symbolic expressions for estimation of non-local parameter,
- Chapter 8 - Conclusions and Further research - in this chapter the conclusions are given that are based on results obtained using MD simulations, non-local plate theory and AI methods, with the short glimpse on further research.

The novelty in this doctoral dissertation can be divided in three segments and these are:

- the investigation of mechanical and thermodynamic parameters at different temperatures. The temperature range was defined as the hypothetical temperature range of gas sensor,

- the investigation of graphene sheet utilization as the building block of nanosensor in detection of chemical warfare agents molecules at different temperatures,
- the procedure of dataset development with MD simulations and non-local plate theory which will be used in GP algorithm to obtain symbolic expression for estimation of non-local parameter.

2. Graphene Characteristics and Gas Molecules

The experimental and theoretical research of two-dimensional materials over the last decade has rapidly grown, graphene sheets in particular. Although graphene was experimentally obtained in 2004, the theoretical concept of this material dates back to the second half of the last century. Hans-Peter Boehm and his colleagues [86] coined the term graphene as a combination of graphite and suffix -ene. The term graphene was officially introduced in 1986 to describe a single-layer of carbon atoms. They are also responsible for developing and experimenting with graphene foils back in 1962 [87]. Over the years, different terms were used to describe graphene such as graphite layers, carbon layers, or carbon sheets. The term graphite must not be used to describe a single-layer structure because graphite implies a three-dimensional structure. In [88], isolated or free-graphene was defined as a single atomic plane of graphite, which is sufficiently isolated from its environment to be considered free-standing. In this section, the detailed overview of the mechanical properties of graphene sheets. Gas molecules that will be used in MD and non-local theory simulations are also described.

2.1 Graphene structure

In order to better understand graphene characteristics the graphene structure must be explained first. The carbon atom is a 6^{th} element in the periodic table and elementary constituent element of graphite and graphene. The carbon atom consist of 6 protons, A neutrons and 6 electrons. When number of neutrons is $A = 6$ and $A = 7$ this yields stable isotopes ^{12}C and ^{13}C, respectively and when number of neutron is $A = 8$ this yields radioactive isotopes ^{14}C. When carbon electrons are in electronic ground state the 6 electrons have the configuration $1s^2 2s^2 2p^2$. This means that 2 electrons are in the inner shell 1s, they are close to the nucleus and are not important for chemical reactions. However for chemical reactions, 4 electrons that occupy other shells 2s and 2p orbitals are important. The energy difference between 2s and 2p ($2p_x$,$2p_y$ and $2p_z$) is 4 eV. In order

to form covalent bonds with other atoms such as H, O and C the one electron from 2s orbital must be exited and jump to third 2p orbital. From energy perspective this jump of electron from 2s to third 2p orbital is around 4 eV. The electronic ground state and electronic jump state is shown in Fig. 2.1.

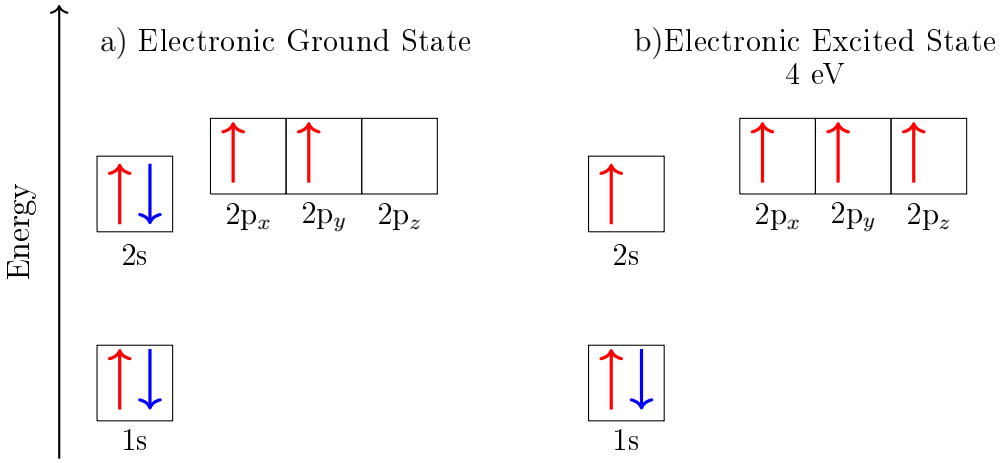

Figure 2.1: Electronic structure of carbon atom: a) Electronic Ground State and b) Electronic Excited State

Looking at the Fig. 2.1, it can be concluded, that there are 4 quantum-mechanical states and these are $|2s\rangle$, $|2p_x\rangle$, $|2p_y\rangle$ and $|2p_z\rangle$. The superposition of quantum-mechanical states $|2s\rangle$ and n $|2p_j\rangle$ states ($j = x, y, z$) is called sp^n hybridisation and this process represents essential role in covalent carbon bonds. There are three types of sp^n hybridisation and these are: sp^1, sp^2 and sp^3 hybridisation. The graphene sheet is one of graphitic allotrope in which carbon-carbon bond is formed by sp^2 hybridisation process. So in this thesis, only sp^2 hybridisation process will be explained.

2.1.1 sp^2-hybridisation

In sp^2-hybridization the superposition of 2s and two 2p orbitals ($2p_x$ and $2p_y$) occur. In this case the planar sp^2-hybridization is formed, the orbitals are oriented in xy-plane and have mutual angles of 120°. The three quantum mechanical states can be written in

mathematical form as:

$$
\begin{aligned}
|sp_1^2\rangle &= \frac{1}{\sqrt{3}}|2s\rangle - \sqrt{\frac{2}{3}}|2p_y\rangle\,, \\
|sp_2^2\rangle &= \frac{1}{\sqrt{3}}|2s\rangle + \sqrt{\frac{2}{3}}\left(\frac{\sqrt{3}}{2}|2p_x\rangle + \frac{1}{2}|2p_y\rangle\right), \\
|sp_3^2\rangle &= -\frac{1}{\sqrt{3}}|2s\rangle + \sqrt{\frac{2}{3}}\left(-\frac{\sqrt{3}}{2}|2p_x\rangle + \frac{1}{2}|2p_y\rangle\right).
\end{aligned}
\tag{2.1}
$$

The two hybridized orbitals $|2p_x\rangle$,$|2p_y\rangle$ lie in the xy-plane while the remaining unhybridized $2p_z$ orbital is perpendicular to the xy-plane as shown in Fig. 2.2.

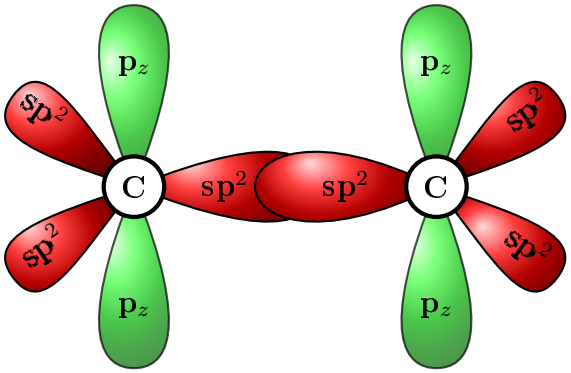

(a) Initial connection between two carbon atoms

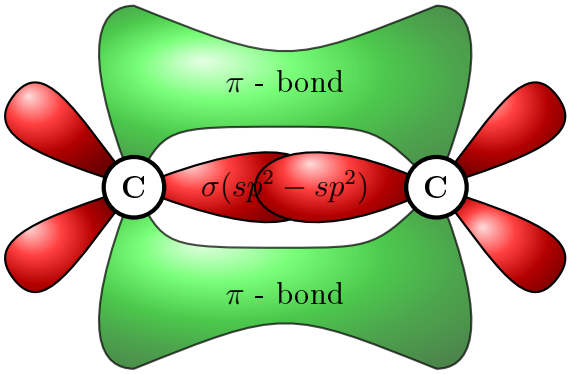

(b) Schematic view of formed σ and π bonds.

Figure 2.2: Graphical representation of sp^2 hybridization.

In graphene sheet each atom has four bonds and these bonds are: one σ bond with each of its three neighbors and one π bond that is oriented out of plane. The distance between two carbon atoms is equal to 1.42 Å[89]. The stability of graphene arises from tightly packed carbon atoms and sp^2 hybridization. A combination of s, p_x and p_y orbitals constitute σ bonds while the p_z orbital makes up the π bond. The π-bonds hybridize together in order to form π and $\pi*$ bands. These bands are main cause of extraordinary graphene

electronic properties such as half-filled band which permits free-moving electrons [89].

2.1.2 Crystal Structure of Graphene

Due to their sp^2 hybridization, the carbon atoms in graphene condense in a honeycomb lattice. This type of hybridization leads to extremely high in-plane stiffness which is one of most significant properties that graphene material possesses [9]. The honeycomb lattice is considered as a triangular Bravais lattice with a two-atom basis (A and B). In Fig. 2.3 a honeycomb lattice is shown in which the carbon atoms are marked with red and blue color where red color represents A and blue color represents B sublattice, respectively. The A sublattice has three nearest neighbors which are connected by $\boldsymbol{\delta}_1, \boldsymbol{\delta}_2$ and $\boldsymbol{\delta}_3$ vectors respectively. The A and B sublattices represent triangular Bravais lattices so honeycomb lattice can be viewed as triangular Bravais lattice with a two-atom basis. As mentioned before, the distance between carbon atoms is 0.142 nm which is the average distance of single and double carbon-carbon bond.

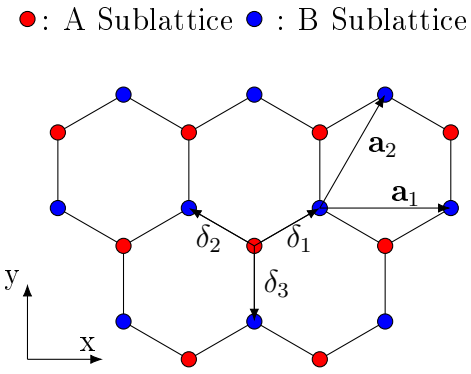

Figure 2.3: The graphical representation of honeycomb lattice. The vectors $\boldsymbol{\delta}_1$, $\boldsymbol{\delta}_2$ and $\boldsymbol{\delta}_3$ in honeycomb lattice connect carbon atoms which are separated by the distance of 0.142 nm. The $\boldsymbol{a}_1$ and $\boldsymbol{a}_2$ represent basis vectors fo triangular Bravais lattice.

The three vectors that connect A sublattice with the B sublattice can be written in following form:

$$\boldsymbol{\delta}_1 = \tfrac{a}{2}\Big(\sqrt{3}\boldsymbol{e}_x + \boldsymbol{e}_y\Big), \quad \boldsymbol{\delta}_2 = \tfrac{a}{2}\Big(-\sqrt{3}\boldsymbol{e}_x + \boldsymbol{e}_y\Big), \quad \boldsymbol{\delta}_3 = -a\boldsymbol{e}_y, \tag{2.2}$$

where $\boldsymbol{e}_x$ and $\boldsymbol{e}_y$ represents basis vectors of fixed coordinate system, shown in Fig. 2.3, and a is the distance between two carbon atoms of 0.142 nm. The triangular Bravais lattice is spanned by the basis vectors that can be written in following form:

$$\boldsymbol{a}_1 = \sqrt{3}a\boldsymbol{e}_x, \quad \boldsymbol{a}_2 = \tfrac{\sqrt{3}a}{2}\Big(\boldsymbol{e}_x + \sqrt{3}\boldsymbol{e}_y\Big). \tag{2.3}$$

Based on equations of basis vectors the lattice spacing is equal to 0.24 nm and area of unit cell to 0.051 nm^2, respectively.

2.1.3 Graphene Sheet Variants

Generally, graphene rectangular sheets can be classified based on their orientations and these are armchair and zigzag edge shapes. Since graphene sheet is two dimensional material if one edge is armchair edge the other is zigzag edge and vice versa. If one of those edges is longer than the other it can be classified as dominating edge. Based on their dominating (longer) edge shape they have different mechanical, thermodynamic and electronic properties. The bonding energies between armchair and zigzag graphene sheets differs which can represent the challenge in performing chemical modifications such as fluorographene, chlorographene and graphene oxide. In Fig. 2.4 the graphical representation of armchair and zigzag edge of graphene sheets are shown.

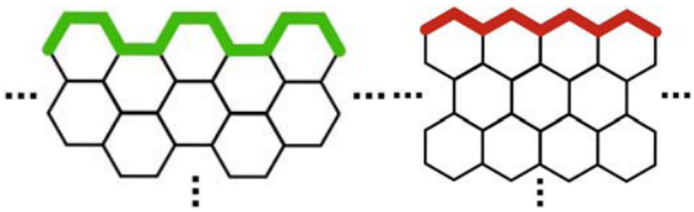

Figure 2.4: The graphical representation of armchair and zigzag edge. The armchair edge is marked in green while the zigzag edge is marked in red [90].

2.2 Mechanical Properties of Graphene

In order to obtain consistent mechanical properties, investigate various influences on mechanical properties and mathematically describe various nanomechanical behaviors such as bending, moving, rotating, vibrating and twisting the graphene mechanics must be well understood. The relationship between strain and stress is essential in graphene mechanics. According to [91] electronic and optical properties of PG are strongly influenced by strain. In this section the mechanical behavior in tension and compression, fracture, shearing, bending, friction and dynamical properties of single layer graphene sheet are described.

2.2.1 Mechanical Properties of Single Layer Graphene Sheet

Since its discovery, the single layer graphene sheet has been investigated from experimental and theoretical standpoint. The mechanical properties obtained using experimental and

theoretical investigation such as Young's modulus, 2D Young's modulus, Poisson's ratio, tensile strength and fracture toughness are given in the Tabs. 2.1, 2.2 and 2.3.

Table 2.1: The experimentally obtained mechanical parameters of single layer graphene sheet (AFM - Atomic Force Microscope).

Method	Young's Modulus [TPa]	2D Young's Modulus [N/m]	Strength [GPa]	Fracture Toughness [MPa$\sqrt{\text{m}}$]
AFM-Nano indentation [9]	1.0 ± 0.1 [9]	340[9]	130[9], $90 \sim 94$ [92]	-
In situ microscale testing [93]	-	-	-	4.0 ± 0.6 [93]

Table 2.2: The mechanical parameters of single layer graphene sheet obtained using different simulation methods (MM - Molecular Mechanics, FEM - Finite Element Method, and MMCM - Modified Molecular-Continuum Model).

Method	Young's Modulus [TPa]	2D Young's Modulus [N/m]	Poisson's Ratio	Strength [GPa]	Fracture Toughness [MPa$\sqrt{\text{m}}$]
DFT	1.029 [94] 1.05 [95]	345 [94]	0.149 [94] 0.186 [95]	A: 110, [95]	-
MD/ MM	A:1.553, Z: 1.111 (Morse), A: 0.879 Z: 1.273[96], 0.96 [97]	320 [97]	0.102∼0.175 [96], 0.28 ± 0.03 [98]	A: 107 Z: 90 [99]	3.44[93], A: 3.38, Z: 3.05, A: 2.87, Z: 3.06 [100]
FEM/ MMCM	A: $\approx$ 1.03, Z: $\approx$1.1 [101] A : 1.040, Z: 0.992 [102]	-	A: $\approx$0.08, Z: 0.06 [101], A: 1.285, Z:1.441 [102]	98 [92]	Mode I A: 3.13, Z: 1.99, Mode II A: 2.70, Z: 3.73 [103]
A - Armchair SLGS, Z - Zigzag SLGS					

Table 2.3: The experimental and simulation results of mechanical parameters obtained with shear test for single layer graphene sheet (DPO - double paddle oscillator, DFT - Density Functional Theory, MD - Molecular Dynamics, and MM - Molecular Mechanics).

Method	Shear Modulus [TPa]	Shear Strength [GPa]	Bending Rigidity (Normal Bending Stiffness) [eV]	Gaussian Bending Stiffness [eV]
Experimental				
Silicon DPO	280 [104]	-	-	-
Simulation				
DFT	-	-	1.44 [105]	1.52[105]
MD/MM	A: 36 $\sim$ 96, Z: 59 $\sim$ 138 [106], 353 (MORSE), 277 (AMBER)[96], A: 340 $\sim$ 370, Z: 430 $\sim$ 470 (AIREBO)[107]	$\approx$ 60 [107]	0.819 $\sim$ 2.385 [108]	-
A - Armchair SLGS, Z - Zigzag SLGS				

2.2.1.1 Tension and Compression

The stiffness of single layer graphene sheet against the tensile stress is characterized with Young's modulus and the ratio of tensile stress to tensile strain under small strains. In [109] researchers found that Young's modulus and tensile strain could rise dramatically as a result of rippling suppression. The interesting phenomena of graphene which is stretched in one in-plane direction and the tensile strain exceeds about 6 % is that the graphene expands its size in direction vertical to the tensile direction and its called Negative Poisson's Ratio (NPR). In [110] the authors have defined two major deformation modes and these are PW-I and PW-II in order to explain the underlying mechanism behind the mechanical properties of SLGS. The PW-I mode is a mode in which angles change while bond lengths remain constant, and PW-II mode is a mode in which bond lengths change while bond angles remain constant during simulation. The PW-I deformation mode yields a positive Poisson's ratio, while the PW-II mode yields a NPR. The graphical representation of PW-I and PW-II mode is shown in Fig. 2.5.

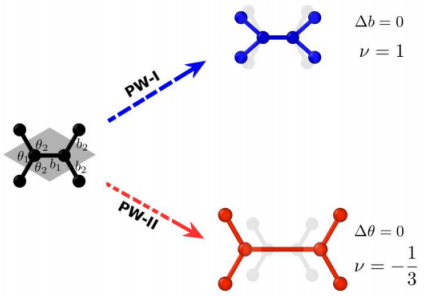

Figure 2.5: Two typical ideal deformation pathways during the tensile deformation of graphene. The left atom cluster is stretched along the horizontal x-direction. The parallelogram gray area indicates the unit cell. PW-I: carbon-carbon bond lengths remain constant ($\Delta b = 0$), while angles are altered to accommodate the external strain, which results in a Poisson's ratio of $\nu = 1$. PW-II: angles are unchanged and bond lengths are elongated to accommodate the external tension, resulting in a NPR of $\nu = -1/3$. The lighter shades show the undeformed structure [110].

In [111] authors have found that NPR occurs only for armchair SLGS under uniaxial tension and that NPR vanishes at temperatures above 2400 K. According to [9], graphene material is the strongest material ever tested. In this paper the authors were measuring the elastic properties and intrinsic breaking strength of graphene sheet using nanoindentation by a atomic force microscope as shown in Fig. 2.6. The results showed graphene intrinsic tensile strength of 130 GPa and Young's modulus of 1 TPa.

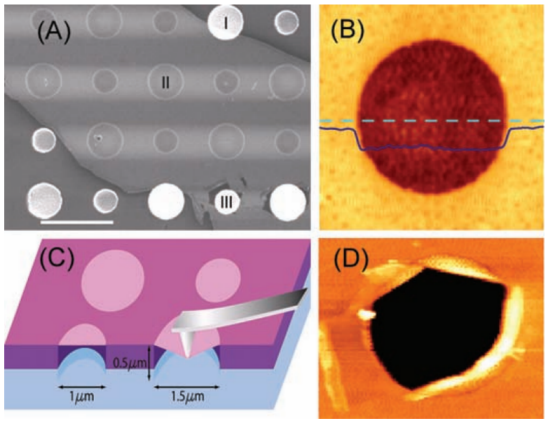

Figure 2.6: Images of suspended graphene sheet [9]: (A) Scanning electron micro-graph of a large graphene flake spanning an array of circular holes 1.5 µm in diameter and 1 µm deep. Area I shows a hole partially covered by graphene, area II is fully covered, and area III is fractured from indentation, (B) Non-contact mode AFM image of one membrane, 1.5µm in diameter. The solid blue line is a height profile along the dashed line. The step height at the edge of the membrane is about 2.5 nm. (C) Schematic of nanoindentation on suspended graphene membrane. (D) AFM image of a fractured membrane.

In [112] authors have performed experimental investigation of graphene in order to obtain

axial stress-strain curve using Raman spectroscopy and transforming this data into true axial stress-strain curves with estimated stress-strain sensitivity of the 2D peak in the spectroscopy. When SLGS is subjected to compressive axial in-plane load and when this load reaches certain limit the buckling will occur, as a sudden sideways deflection of the SLGS central part. The results of tension and compression experiments reported in [113] revealed buckling characteristics of SLGS.

The buckling of SLGS was also theoretically investigated. In [114] using high-order shear deformation theory the equations of motion of non-local theory were derived in order to investigate the buckling of SLGS. The influence of non-local effect on buckling of biaxially compressed graphene was investigated in [115] and showed that influence of non-local effect on biaxially compressed is smaller than on uniaxially compressed graphene. In [116] the authors have investigated, the influence of the vacancy location and the density of vacancies on the the bending behavior of the single layer graphene sheets. This investigation is based on the structural mechanic approach with covalent bonds modeled as beam finite elements. The results showed that the defect in the center of the nanosheet has the highest influence on the bending behavior. The continuum-based approach was used in [117] in order to investigate the influence of the boundary conditions, applied loads and skew angles on buckling of skew shaped graphene. The results showed that influence of the aspect ratio on buckling loads is significant for small skew angles of graphene sheet than other skew angles. The investigation also showed graphene sheet exhibits maximal buckling loads when subjected to pure shear loads. Besides the compression of SLGS by in-plane loads the compression by out-of-plane loads was also investigated usually with AFM nanoindentation. In [118] the authors were triggering the out-of-plane displacements of single carbon atom of a graphene sheet using AFM in order to establish the relationship between the elasticity and out-of-plane displacements. The results of conducted investigation showed that intrinsic modulus increased dramatically when the distance is over 0.35 nm and as the out-of-plane displacement of the single atom becomes larger the out-of-plane elastic stiffness at the carbon atom site also becomes larger. The schematic illustration is shown in Fig. 2.7.

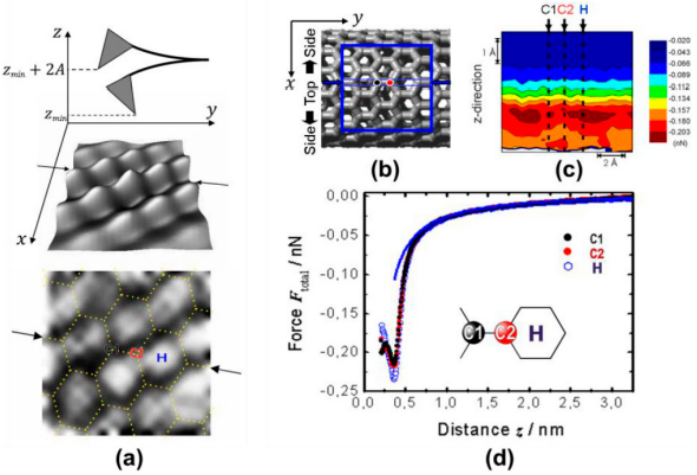

Figure 2.7: (a) Schematic illustration of a 3DFFS measurement (b) Schematic illustration of a 3DFFS measurement (c) 2D force field map (d) Interatomic force vs. vertical distance z [118].

2.2.1.2 Fracture

A fracture can be defined as separation of material into two or more pieces under the action of stress. The fracture toughness of the material represents the ability to resist the fracture. In [93] the authors have proved that graphene exhibits brittle fracture which is in accordance with classical Griffith theory of brittle fracture. They have also experimentally determined the value of fracture toughness which is equal to 4.0 ± 0.6 MPa$\sqrt{\text{m}}$ of graphene obtained using chemical vapor deposition (CVD) method. In [119] the fracture mechanics of graphene was studied using molecular dynamics. The results showed that initial crack length can determine crack's path and the edge structure and the value of obtained fracture toughness is equal to 11.24 Jm^{-2}. With combination of MD simulations and fracture mechanics in [120] authors have showed that the fracture forces from the spherical indenter cannot be directly mapped onto the uniaxial strength but cylindrical indenters could.

2.2.1.3 Shearing

In Fig. 2.8 the schematic procedure of investigating shear phenomenon on armchair and zigzag graphene is shown.

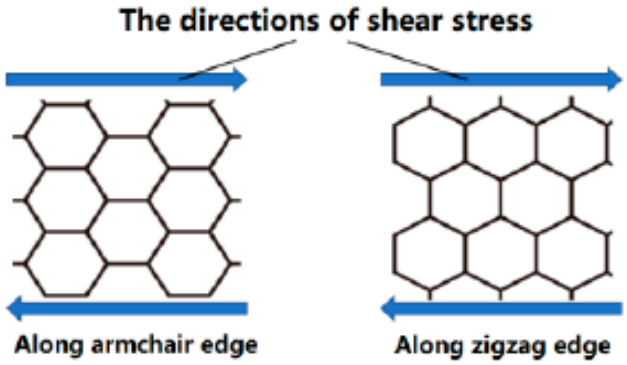

Figure 2.8: The schematic view of shear stress loading along armchair and zigzag edge [91].

As seen from Fig. 2.8 in armchair and zigzag graphene sheet one boundary is fixed while constant forces are applied on each atom of the opposite boundary. The applied forces are parallel to the edges of graphene sheet. Shear modulus of graphene sheet has been obtained using experimental and theoretical methods. In [102] the shear modulus of graphene sheet was obtained using molecular mechanics method. For armchair graphene the shear modulus is 0.228 TPa and for zigzag graphene 0.213 TPa. The Monte Carlo simulations was applied in [121] to obtain temperature dependent shear modulus and the highest value was obtained at 700 K and is equal to 0.483 TPa. Using MD simulation method the authors in [122] obtained shear modulus value 0.358 TPa at 0 K with AMBER force field. The MD simulation with AIREBO force field was used in [107] to obtain shear modulus of armchair and zigzag graphene sheet. For armchair graphene the shear modulus is in range from 0.34 to 0.37 TPa while for zigzag graphene sheet from 0.43 to 0.47 TPa. The temperature in these simulations was varied in range from 0 to 2000 K and the results showed that shear moduli rises as the temperature rises until it reaches the 800 K. After 800 K as the temperature rises the value of shear modulus decreases. As the temperature increases the shear strength also decreases from 60 to 30 GPa.

2.2.1.4 Bending

Bending [123] can be defined as the behavior of a slender structural element subjected to an external load that is applied perpendicular to a longitudinal axis of the element. The bending of graphene under a loaded force is influencing electrical, thermal and magnetic properties of material. The bending of graphene generally is not studied well when compared number of research investigating this phenomena to the papers regarding tensile strength. In [105] the authors have determined bending rigidity and Gaussian bending stiffness which are equal to 1.44 and -1.52 eV respectively.

2.2.1.5 Friction

In [124] the authors have investigated the friction behavior of graphene flake sliding on a supported graphene substrate. The results showed that friction increases exponentially with decreasing stiffness and that stiffness dependent friction has close relationship with stiffness-dependent deformation. Besides experimental investigation the MD simulation was applied in order to investigate fundamental atomic scale mechanisms of graphene friction [125]. The investigation showed that grain boundary region has greater contribution to the friction than bulk grain regions.

2.2.1.6 Dynamic Properties

Besides the investigation of mechanical properties of SLGS from theoretical and experimental standpoint over the years the dynamical properties of this material were also investigated. The investigation of dynamical properties of SLGS include investigation of natural frequencies, mode shapes, linear and non-linear vibrations and power spectral density properties. In Tab. 2.4 a list of research papers is given in which the SLGS dynamic properties were investigated. From investigations presented in the Tab. 2.4 it can be concluded that the natural frequencies and mode shapes are affected by size of SLGS, and by various boundary conditions. The natural vibrations are decreasing with bigger-size of SLGS. In [129, 130] it has been reported that natural frequencies are higher in case of armchair graphene sheet than in the zigzag. The natural vibrations of SLGS using continuum mechanics [129] disagree with those obtained via molecular mechanics and molecular dynamics, which may indicate the limitation of continuum theory in simulation properties.

2.2.2 Influence of Temperature on Mechanical Properties of SLGS

There are a number of research papers which investigated the influence of temperature on mechanical properties of SLGS. In [138] it was found that fracture stress and strain linearly change with temperature. As temperature increase the graphene turns to be weaker and as a consequence Young's modulus decreases. In research [139] the results confirmed that temperature has negative effect on Young's modulus. As the temperature increases the Young's modulus monotonically drops down.

2.3 Gas Molecules

The analyte molecules (gas/vapor molecules) that were used to investigate the possibility of utilizing the graphene sheet as a sensing element of NEMS nanosensor using MD sim-

Table 2.4: List of different investigations of SLGS dynamic properties

References	Methods	Subjects Investigated
[126, 127]	Molecular structural mechanics	Natural frequencies and mode shapes
[128]	A hybrid atomistic-structural element	Linear and nonlinear vibrations
[129]	Molecular mechanics and equivalent continuum structure	Natural frequencies of axial and bending modes of SLGS with different chiralities, aspect ratios
[130]	A non-local model based on differential quadrature method and molecular dynamics simulation	Natural frequencies
[131]	An equivalent atomistic-continuum finite element model	Natural frequencies and acoustic wave propagation characteristics of graphene nanoribons.
[132]	A membrane model	Nonlinear vibrations
[133]	Molecular mechanics	Transverse vibrations
[134]	Modifed coupled stress theory	The size effect on vibrations of SLGS on an elastic matrix
[135]	A finite element method based on molecular mechanics	2D and 3D modal and transient analyses
[136]	Molecular mechanics	Natural frequencies and the buckling modes
[137]	A finite element method based on molecular mechanics	Natural frequencies and mode shapes for cantilever and bridged SLGS

ulations and non-local plate theory are the molecules of chemical warfare agents (CWA). The CWAs according to [140] are categorized based on physiological effects caused on the human body as blister agents, nerve agents, choking agents, asphyxiants, and behavioral altering agents. However, only three CWA molecules will be used and these are Hydrogen Cyanide (asphyxiant), Soman (GD) (nerve agent), and 3 - quinuclidinyl benzilate (BZ) (behavioral agent). These molecules were chosen based on their mass from the lowest (hydrogen cyanide) to the highest (3-quinuclidinyl benzilate). All these chemical compounds are in liquid form. However, each of these molecules at certain temperatures and pressures evaporates (vapor pressure). According to [140], the vapor pressure for hydrogen cyanide is 100 kPa at 298.15 K, for soman is 53 Pa at 298.15 K and for 3 - quinuclidinyl benzilate is 3.17×10^{-8} Pa at 298.15 K, respectively. The idea is to investigate the possibility of detecting the aforementioned chemical compounds with the graphene sheet using MD simulations and non-local theory. Due to the complexity of the molecules in terms of size, the number of atoms and lack of interatomic potential required for the approximate definition of interaction between gas/vapor molecules and graphene sheet in MD simulations these molecules will be approximated with the carbon atom attached to the graphene sheet surface with modified mass. In each MD simulation with graphene sheet and gas/vapor molecule, the mass of the attached carbon atom to the graphene sheet surface is equal to the mass of the specific gas/vapor molecule. Since in MD simulations the *metal* unit style was utilized due to the requirement of REBO interatomic potential used in this thesis, the mass of each molecule modeled as attached carbon atom of modified mass must be defined in g/mol. In the non-local theory for the calculation of frequency shift caused by these molecules, their mass of the CWA molecule in yg will be used in the calculation. In Tab. 2.5 the mass values of CWA molecules that will be used in MD simulation and non-local theory is given.

Table 2.5: Mass and weight properties of gas/vapor molecules [140]

Chemical Compound Name	Chemical formula	Mass [Da = g/mol]	Mass of one molecule [yg]
Soman (GD)	$C_7H_{16}FO_2P$	182.17	302.51
Hydrogen Cyanide	HCN	27.03	44.89
3 - quinuclidinyl benzilate (BZ)	$C_{21}H_{23}NO_3$	337.42	560.31

3. Simulation Methods

In this chapter the detailed overview of methods utilized in this thesis will be given in order they were used. First the overview of Molecular Dynamic Simulation method will be given which was used in order to determine mechanical parameters, natural frequencies of graphene sheet and absolute/relative frequency shift caused by gas/vapor molecules attached at the center of graphene. Finally, the non-local theory will be described as an alternative method for obtaining the natural frequencies of graphene sheets. The frequency result obtained using MD simulation and non-local theory will be compared in order to obtain the correct value of the non-local parameter.

3.1 Molecular Dynamics

The MD simulation is a method for studying physical movements of atoms and molecules. In the MD simulation atoms and molecules interact for the fixed period of time which gives insight into dynamical evolution of the system. From physical point of view in MD simulation, motion of all atomic nuclei in the system is treated as classical, Newtonian particles:

$$\boldsymbol{f}^{\alpha} = m^{\alpha}\ddot{\boldsymbol{r}}^{\alpha}, \quad \alpha = 1, 2, ..., N, \tag{3.1}$$

where N represents number of atoms in the system, m^{α} is the mass of the atom α, $\ddot{\boldsymbol{r}}^{\alpha}$ is the position and $\boldsymbol{f}^{\alpha}$ is time-dependent force acting on particle α due to external effects and presence of its neighbors. The two dots over position variable represent time differentiation of this variable so in Eq.(3.1) the $\ddot{\boldsymbol{r}}^{\alpha}$ represents acceleration of atom α. The $\boldsymbol{f}^{\alpha}$ is function of the positions of all atoms in the system but in some cases may depend on particle velocities. The forces acting on atoms in the system are given by:

$$\boldsymbol{f}^{\alpha} = -\frac{\partial U_{total}}{\partial \boldsymbol{r}^{\alpha}}, \tag{3.2}$$

where U_{total} represents the total potential energy of the system. The total potential energy of the system is the sum of internal part U_i and external part U_e. The internal potential energy comes from atom interactions in the system and external part comes

from external fields and constraints. The temperature of the system is obtained from time averaged vibrational part of system kinetic energy and is expressed in the following form:

$$T = \frac{2}{3Nk_B}\overline{T_v} = \frac{2}{3Nk_B}\overline{\sum_{\alpha=1}^{N}\frac{1}{2}m^{\alpha}||\mathbf{v}_{rel}^{\alpha}||^2}, \tag{3.3}$$

where $\bar{T}_v$ is the averaged vibrational kinetic energy of the system, N is the number of atoms in the system, k_B the Boltzmann constant which is equal to 1.3807×10^{-23}J/K, $\mathbf{v}_{rel}^{\alpha}$ represents velocity of atom α relative to the center of mass velocity, and m^{α} the mass of atom α.

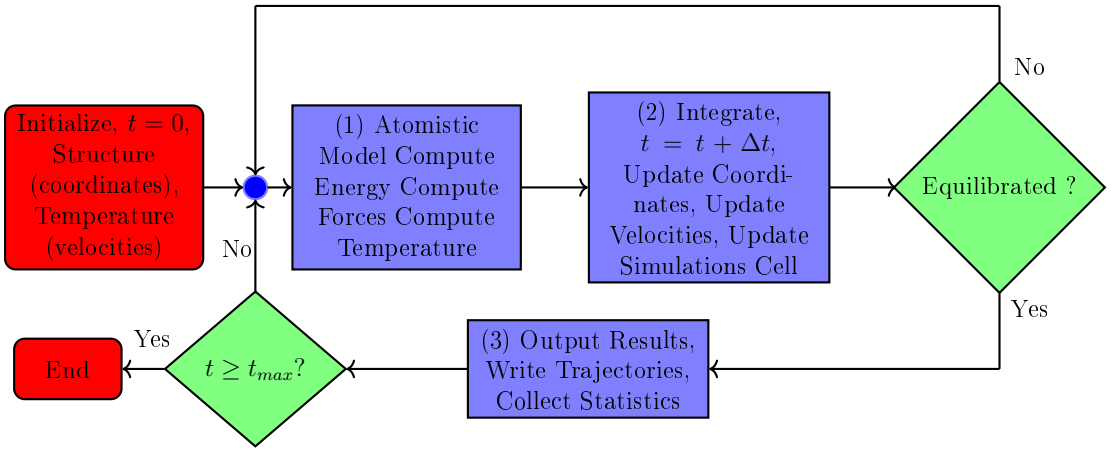

Figure 3.1: Flowchart of MD Simulation process

The steps of MD simulations are:

- Initialization step involves definition of the initial structure, boundary conditions and the particle velocities.
- The equilibration loop - before performing the MD simulation the system must be relaxed at certain temperature and pressure.
- The main integration loop - after the system is equilibrated the evolution of the MD system is investigated usually for thousands or millions of timesteps.

3.1.1 Interatomic Potentials

The interatomic potentials in molecular dynamics are used for calculation for the potential energy of the system which consists of atoms and these atoms have their positions in space [141, 142, 143].

3.1.1.1 Functional Form

Mathematically, the functional form of interatomic potential can be written as series expansion of functional terms that can depend on the position of one, two, three or more atomes at a time. The total potential of the system in a general form can be written as:

$$U_{total} = \sum_{i}^{N} U_1(\vec{r}_i) + \sum_{i,j}^{N} U_2(\vec{r}_i, \vec{r}_j) + \sum_{i,j,k}^{N} U_3(\vec{r}_i, \vec{r}_j, \vec{r}_k) + ..., \tag{3.4}$$

where U_1, U_2 and U_3 represent one-body term, two-body term and three body term, respectively. N represents the number of atoms in the system while the $\vec{r}_i$ represents the position of atom. The one-body term is useful only if the atoms in the system are placed in external field such as electrical field. If there is not any external field that affect the system, the total potential depends only on the relative position. In other words the functional form can be reformulated as a function of interatomic distances $\vec{r}_{ij} = |r_i - r_j|$ and angles between the bonds θ_{ijk}. The total potential of the system without the presence of the external forces can be written in the following form:

$$U_{total} = \sum_{i,j}^{N} U_2(r_{ij}) + \sum_{i,j,k}^{N} U_3(r_{ij}, r_{ik}, \theta_{ijk}) + ..., \tag{3.5}$$

The term with the order higher than 2 can be classified as many-body potential and in some interatomic potentials these many body interactions are integrated as pair potentials. The key component in the interatomic potential is the cutoff distance r_{cut}. This parameter defines the effective range of the interatomic potential. If the distance between two atoms is larger than the cutoff distance the potential is zero.

3.1.1.2 Force Calculation

In order to obtain forces that are acting between atoms in each iteration of MD simulation the differentiation of the total system energy with respect to the atom positions must be performed. For example, in order to get the force that is acting on atom α the three-dimensional derivative (gradient) of total system potential with respect to atom position must be determined. The force equation can be written in the following form:

$$f^{\alpha} = -\nabla U_{total}, \tag{3.6}$$

As mentioned earlier there are the two body and many body potentials. In case of two body potential the Eq. (3.6) is easy to calculate, however in case of many body potentials the differentiation in Eq. (3.6) becomes far more complex.

3.1.2 Classification of Interatomic Potentials

The problem in simulating the atomic system generally is the selection of appropriate interatomic potential. Unfortunately, the true interatomic interactions are quantum mechanical in the nature and it is impossible to cast the interactions of all electrons and nuclei described by Schrödinger/Dirac equations into an analytical functional form. So, all analytical interatomic potentials are approximations. As stated before there are two groups of potentials and these are:

- pair potentials - for inert gases, van der Waals interactions in organic materials (hard-spheres, Lennard-Jones and Morse potential), and
- many body potentials:
  - Potentials for metallic systems - embedded atom method, effective medium theory, glue model, corrected effective medium potential and
  - potentials for covalently bounded systems (bond order potentials) - Stillinger - Weber, Tersoff, REBO and AIREBO.

3.1.2.1 Lennard-Jones Potential

The LJ potential is a mathematical model that approximates interactions between neutral atoms or molecules. This potential is used to model the Van der Walls interaction which can be described as the combination of attractive and repulsive forces between two atoms that are not bonded. The potential energy varies with the separation distance between two atoms. As seen from Fig. 3.2 when separation distance between two atoms is large the energy is almost zero. As the distance between two atoms reduces further the energy decreases, passing through a minimum and as the distance reduces further the energy increasingly grow. The 12-6 LJ potential can be written in the following form

$$U_{LJ} = 4\varepsilon\left[\left(\frac{\sigma}{r}\right)^{12} - \left(\frac{\sigma}{r}\right)^{6}\right], \tag{3.7}$$

where ε, σ and r represent the depth of the potential well, distance at which potential is zero and distance between particles, respectively. In Fig. 3.2 the 12-6 LJ interaction potential is shown for two non-bonded carbon atoms. The parameters for 12-6 LJ interaction is taken from [144].

3.1.2.2 Bond-Order Potentials

These types of potentials are class of empirical (analytical) interatomic potentials that are used in MD and molecular statics simulations. When compared to molecular mechanics

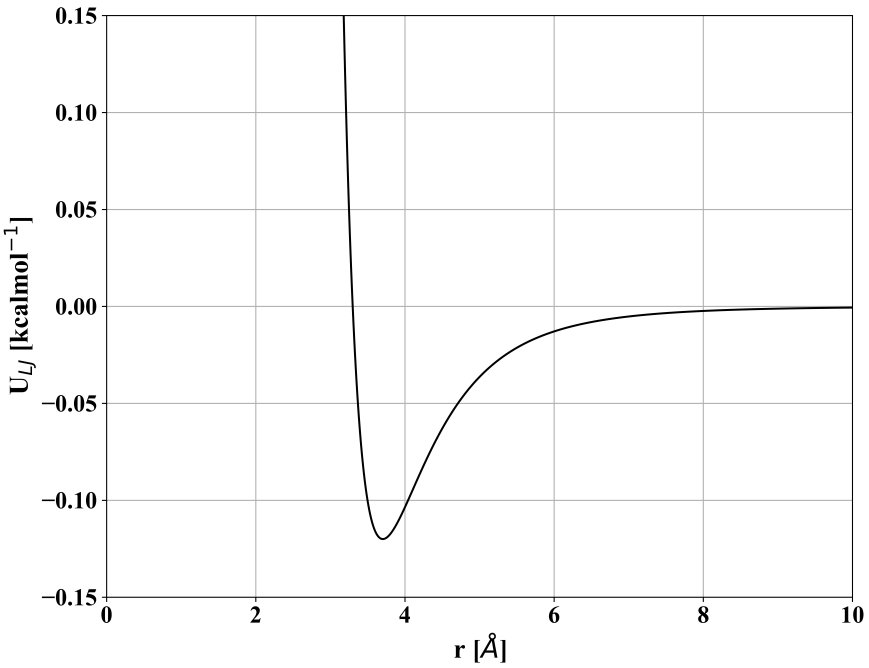

Figure 3.2: Example of 12-6 Lennard Jones potential for two carbon atoms

force fields, these potentials have advantage since it is possible with them to describe several different bonding states of an atom with the same parameters. The practical advantage using these potentials is the ability to approximate chemical reactions. These potentials are based on Linus Pauling bond order concept [145, 146] which can be written in the following form

$$U_{ij}(r_{ij}) = U_{rep}(r_{ij}) + b_{ijk}U_{att}(r_ij), \tag{3.8}$$

where U_{rep} and U_{att} represent the repulsive and attractive part of the potential while the b_{ijk} represents bond order, respectively. The Eq.(3.8) shows that the potential consists of a simple pair potential which depends on the distance between two atoms r_{ij} while the strength is modified with the environment of the atom i by the bond order b_{ijk}. As stated in [145], the variable b_{ijk} is a function which depends inversely on the number of bonds to the atom i, and the bond angles between sets of three atoms ijk. Optionally the b_{ijk} could depend on the relative bond lengths r_{ij}, and r_{ik}, respectively. Regarding the bond order there are two limiting cases, and these are:

- the case of diatomic molecule (one atomic molecule) - the value of $b_{ijk} = 1$ and this case corresponds to the strongest and shortest possible bond, and
- the increasingly many number of bonds with some interaction range - the $b_{ijk} \to 0$, and the potential becomes repulsive.

3.1.2.3 REBO Potential

The original TERSOFF potential was designed for structures made from Si and C atoms, and was capable of describing single, double, and triple bond configurations. However, the TERSOFF potential was not able to describe radicals and conjugate versus non-conjugate atom configurations. The TERSOFF interatomic potential could not distinguish the different kinds of bonds that can form between carbon and hydrogen in hydrocarbon systems. This disadvantages of TERSOFF potential was motivation for developing the reactive empirical bond-order (REBO) potential, as reported in [147, 148]. The REBO potential is essentially a function which is used for calculating the potential energy of covalent bonds and interatomic force. The binding energy for the hydrocarbon potential can be written in the following form

$$E_{REBO} = \sum_{i} \sum_{j \neq i} \Big[U_R(r_{ij}) - b_{ij} U_A(r_{ij}) \Big], \tag{3.9}$$

where the repulsive and attractive function can be determined from following expressions

$$\begin{aligned} U_R(r_{ij}) &= f_{ij}(r_{ij}) \frac{D_{ij}^e}{S_{ij}-1} e^{-\sqrt{2/S_{ij}}\beta_{ij}(r-R_{ij}^e)}, \\ U_A(r_{ij}) &= f_{ij}(r_{ij}) \frac{D_{ij}^e S_{ij}}{S_{ij}-1} e^{-\sqrt{2/S_{ij}}\beta_{ij}(r-R_{ij}^e)}, \end{aligned} \tag{3.10}$$

where S_{ij} and β_{ij} are empirical parameters, R_{ij}^e is the equilibrium distance, and D_{ij}^e is the depth of the potential well. The function $f_{ij}(r)$ is responsible for restricting the pair potential to the nearest neighbors and can be written in the following form

$$f_C(r_{ij}) = \begin{cases} 1, & r < R - D \\ \frac{1}{2} - \frac{1}{2}\sin\left(\frac{\pi}{2}\frac{r-R}{D}\right). & r - D < r < R + D \\ 0, & r > R + D \end{cases}. \tag{3.11}$$

The parameters R and D in smooth function cutoff given in Eq.(3.11) are not systematically optimized but are chosen to include first-neighbor shell for several high-symmetry bulk structure of silicon, graphite, diamond, simple cubic and face centered cubic (FCC) structures. When r is in range $R - D < r < R + D$ the value of f_C function decreases from 1 to 0.

The empirical bond-order function b_{ij} is represented by the average of terms associated with each atom in a bond and can be written in the following form

$$b_{ij} = \frac{(B_{ij} + B_{ji})}{2} + F_{ij}(N_i^t, N_j^t, N_{ij}^{conj}), \tag{3.12}$$

where N_i^t is the total number of carbon or nitrogen atom neighbors of atom i, N_{ij}^{conj} represents the number of bonds between atoms i and j that are part of conjugated system. The function B_{ij} can be written in the following form

$$B_{ij} = \left\{ 1 + \sum_{k \neq i,j} G_i(\theta_{ijk}) f_{ik}(r_{ik}) e^{\alpha_{ijk}[(r_{ij} - R_{ij}^e) - (r_{ik} - R_{ik}^e)]} + H_{ij}(N_i^H, N_i^C) \right\}^{-\delta_i}. \tag{3.13}$$

In Eq.(3.13) the N_i^C and N_i^H represents the number of carbon and hydrogen atoms in the system respectively. The parameter $G(\theta_{ijk})$ represents the function of the angle between bonds of atoms $i-j$ and $i-k$. The functions $f_{ij}(r_{ij})$ are introduced to define the bonding connectivity in the system and to make the potential function continuous. These functions are utilized to define the values for N_i^H, N_i^C, N_i^t, and N_{ij}^{conj}. The values for N_i^H, N_i^C can be written in the following form

$$\begin{aligned} N_i^H &= \sum_{j(=\text{Hydrogen})} f_{ij}(r_{ij}), \\ N_i^C &= \sum_{j(=\text{Carbon})} f_{ij}(r_{ij}). \end{aligned} \tag{3.14}$$

The value of N_i^t can be calculated from

$$N_i^t = N_i^H + N_i^C. \tag{3.15}$$

The values of the N_i^t for neighbors of two carbon atoms involved in a bond can be used to determine if the bond is part of conjugated system. If there are any neighbors of carbon atoms that have a coordination less than 4, the bond is defined as being part of conjugated system. The value of N_{ij}^{conj} between two carbon atoms i and j can be determined from

$$N_{ij}^{conj} = 1 + \sum_{\text{carbons} k(\neq i,j)} f_{ik}(r_{ik}) F(x_{ik}) + \sum_{\text{carbons} l(\neq i,j)} f_{jl}(r_{jl} F(x_{jl})). \tag{3.16}$$

In Eq.(3.16) the function $F(x_{ik})$ is a piecewise function which can be written in the following form

$$F(x_{ik}) = \begin{cases} 1, & x_{ik} \leq 2 \\ \frac{1+\cos(\pi(x_{ik}-2))}{2}, & 2 < x_{ik} < 3 \\ 0, & x_{ik} \geq 3 \end{cases}. \tag{3.17}$$

where

$$x_{ik} = N_k^{tot} - f_{ik}(r_{ik}). \tag{3.18}$$

The function $F(x_{ik})$ given in Eq.(3.17) yields continuous value of N^{conj} as bonds break and form and as second-neighbor coordinations change. If the value of N^{conj} is equal to 1, a bond between atoms is not a part of conjugated system and the function gives appropriate values. If the value of $N^{conj} \geq 2$ the bond between atoms is part of conjugated system and parameters fit to conjugated bonds are used.
As stated earlier, the second-generation REBO potential energy function for solid carbon and hydrocarbon molecules is used in this thesis and incorporated in LAMMPS program package. As reported in [149] the difference between second-generation and the original REBO is that the second-generation allows the breaking and forming of covalent bonds with associated changes in atomic hybridization within a classical potential. By doing so the second-generation REBO potential is a powerful tool for modeling complex chemistry in large many-atoms systems. These improved version of second-generation REBO potential was achieved with improved analytic functions and the extended database relative to the original version.
The original REBO potential had following disadvantages, and these are:

- angular terms in the first generation of REBO had a minimum angle θ of 90° and two maxima at 0° and 180°,
- bond order should decrease monotonically with decreasing bond angle θ_{kij},
- the parameter b_{ij} is proportional to $\frac{1}{\sqrt{G(\theta_{kij})}}$ so if $G(\theta_{kij})$ should decrease when the value of θ_{kij} increases,
- the lack of double bond or conjugate bond rotation barrier in order to prevent unrealistic rotations from occurring.

So, in order to improve the first generation of REBO potential, the modification was made on angular term and the torsional term was introduced. The bond order in second generation of REBO potential can be written in the following form

$$b_{ij} = \frac{(B_{ij} + B_{ji})}{2} + \Pi_{ij}^{RC} + B_{ij}^{DH}, \tag{3.19}$$

where Π_{ij}^{RC} is the same function $F_{ij}(N_i^t, N_j^t, N_{ij}^{conj})$ as in the first generation of REBO potential, while the b_{ij}^{DH} the double bond and conjugate bond torsion term. The B_{ij} can be written in the following form

$$B_{ij} = \left(1 + \sum_{k(\neq i,j} f_{ik}(r_{ik}) G(\cos\theta_{kij}) e^{\alpha_{kij}((r_{ij} - R_{ij}^{eq}) - (r_{ik} - R_{ik}^{eq}))} + P_{ij}(N_i^C, N_i^H)\right)^{-\frac{1}{2}}. \tag{3.20}$$

The modification of angular term was made by introduction of new function, implementation of new fit method, and flexibility in various bond angles during the chemical reaction. For θ_{kij} in range from 109.47° up to 180° the function $G(\cos\theta_{kij})$ can be written in the following form

$$G(\cos\theta_{kij}) = a_0 + a_1\cos\theta_{kij} + a_2\cos^2\theta_{kij} + ... + a_6\cos^6\theta_{kij}. \tag{3.21}$$

As seen for Eq.(3.21) the $G(\cos\theta_{kij})$ is the sixth order polynomial spline. When θ_{kij} is in range from 0 up to 109.47° the $G(\cos\theta_{kij})$ can be written in the following form

$$g(\cos\theta_{kij}) = G(\cos\theta_{kij}) + Q(N_i^t)\Big(\gamma(\cos\theta_{kij}) - G(\cos\theta_{kij})\Big), \tag{3.22}$$

where

$$Q(N_i^t) = \begin{cases} 1, & N_i^t < 3.2 \\ \frac{1+\cos\left(\frac{\pi}{3.7-3.2}(N_i^t-3.2)\right)}{2}, & 3.2 < N_i^t < 3.7 \\ 0, & N_i^t > 3.7 \geq 3 \end{cases}. \tag{3.23}$$

Introduction of torsional term to the interatomic potential provided the rotation barrier for double bond and conjugate bond. When the torsion angle is zero the value of parameter B_{ij}^{DH} is zero, and when the value of torsion angle is 90° the value of $B_{ij}^{DH} = T_{ij}$. The B_{ij}^{DH} can be written in the following form

$$B_{ij}^{DH} = T_{ij}(N_i^t, N_j^t, N_{ij}^{conj})\left(\sum_{k(\neq i,j)}\sum_{l(\neq i,j)}\Big(1-\cos^2\Theta_{ijkl}\Big)f_{ik}(r_{ik})f_{jl}(r_{jl})\right), \tag{3.24}$$

where $T_{ij}(N_i^t, N_j^t, N_{ij}^{conj})$ is a tri-cubic spline function. The cosine function for angle Θ_{ijkl} can be written in the following form

$$\cos\Theta_{ijkl} = (\overrightarrow{r_{ji}} \times \overrightarrow{r_{ik}}) \cdot (\overrightarrow{r_{ij}} \times \overrightarrow{r_{jl}}). \tag{3.25}$$

3.1.3 Boundary Conditions

The MD system may be simulated in a number of ways. The N particles may be isolated, i.e. surrounded by vacuum, but in most cases the goal is to investigate the bulk properties of liquid or solid system so some other boundary conditions (BC) must be imposed. In order to perform MD simulation of any system containing N particles the simulation box in which these N particles are located must be defined. Depending on the nature of problem simulated using MD the following BC could be applied in each direction x, y and z: periodic, non-periodic and fixed (rigid), non-periodic and shrink-wrapped, non-

periodic and shrink-wrapped with a minimum value. The difference between periodic and non-periodic BC lies in the fact that in the molecular system with a non-periodic BC the particles do not interact across the boundary and do not move from one side of the box to the other. For example, imposing non-periodic fixed walls on molecular system the surface effect would overshadow the bulk physics. The surface effects would appear since on the domain walls there is large number of atoms ($N^{-1/3}$). The properties of previously mentioned BC imposed on the walls of the simulation box, are:

- the periodic style - the particles interact across the boundary, and can exit one end of the simulation box and re-enter on the opposite end of the box. This style of boundaries can change in size due to the constant pressure BC or box deformations. However, in order to perform the simulation with the constant pressure the periodic style must be applied to both faces of the dimension.
- the non-periodic and fixed style - the faces of the box are fixed. In this case if the atom moves outside the face it will be deleted in the next step of MD simulation and the re-neighboring will occur.
- the non-periodic and shrink-wrapped style - the position of the face is set so as to encompass the atoms in that dimension, no matter how far they move.
- the non-periodic and shrink-wrapped with minimum-value style - type of BC in which shrink-wrapping occurs, but is bounded by the value specified in the data or restart file or set by the configuration of simulation box.

3.1.4 The microcanonical ensembles

The evolution of the MD simulation may be used in order to determine macroscopic thermodynamic properties of the system. However, the MD system must obey the ergodic hypothesis meaning that the time averages of an ergodic system correspond to microcanonical ensemble averages. There are three most commonly used ensembles and these are:

- the NVE ensemble - the system consists of constant number of atoms (N) which occupies constant volume (V) and energy (E) of the system which is also constant. This system can be described as adiabatic system in which trajectory of particle can be described as transformation of potential to kinetic energy while total energy of the system is conserved.
- the NVT ensemble is slightly more realistic simulation when compared to NVE ensemble. The system consists of constant number of atoms (N) which occupies

constant volume (V) at approximately constant temperature (T). In order to control temperature in MD simulation the thermostat methods must be applied. Today two most commonly used thermostat methods are: Langevin (stochastic) thermostat and Nose-Hoover (NH) thermostat.

- the NPT ensemble - also known as isothermal–isobaric ensemble. The system consist of constant number of atoms (N) at approximately constant pressure (P) and temperature (T).Controlling the pressure P during the simulations is called barostating. In MD simulation typically the target temperature and/or pressure are specified in the script by user, and the role of the thermostat or barostat is to equilibrate the MD system and reach the desired temperature and pressure. The barostating methods are: Nose-Hoover and Berendsen.

3.2 Non-local Plate Theory

The basic principle of classical continuum mechanics is that it eliminates the influence of strain field of distant point on the reference point. The non-local theory of elasticity incorporates these distant effects which are known as non-local effects or size-effects. Let's say that in the elastic continuum there is reference point named $\boldsymbol{x}$. In classical continuum mechanics the stress field at a reference point $\boldsymbol{x}$ depends only on strain at that point while in the non-local theory of elasticity the stress field at a reference point $\boldsymbol{x}$ depends on strain at that point and the strain at every point $\boldsymbol{x'}$ in the domain [150]. According to [151] the previous statement is in accordance with the atomic theory of lattice dynamics and experimental observation on phonon dispersion. It can be concluded that the classical elasticity theory could be obtained from non-local theory of elasticity if the effects of strain at all other points are neglected. In the non-local elasticity, the most general form of the constitutive relation involves integral over the entire domain. This integral consists of a non-local kernel function $\alpha(|\boldsymbol{x}-\boldsymbol{x'}|,\xi)$ that describes the relative influences of strains at various locations on the stress at reference point. The constitutive equations of homogeneous, isotropic and non-local elastic solid free of external forces can be written in the following form:

$$\begin{aligned}
&\sigma_{kl,k}+\rho(f_l-\ddot{u}_l)=0,\\
&\sigma_{kl}(\boldsymbol{x})=\int_{\boldsymbol{\Omega}}\alpha(|\boldsymbol{x}-\boldsymbol{x'}|,\xi)\sigma^c_{kl}(\boldsymbol{x'})d\Omega(\boldsymbol{x'}),\\
&\sigma^c_{kl}(\boldsymbol{x'})=\lambda\varepsilon_{rr}(\boldsymbol{x'})\delta_{kl}+2\mu\varepsilon_{kl}(\boldsymbol{x'}),\\
&\varepsilon_{kl}(\boldsymbol{x'})=\Big(\frac{\partial u_k(\boldsymbol{x'})}{\partial x'_l}+\frac{\partial u_l(\boldsymbol{x'})}{\partial x'_k}\Big),
\end{aligned} \tag{3.26}$$

where:

- $\sigma_{kl}, \sigma_{kl}^{c}$ - non-local and classical stress,
- $\alpha(|\boldsymbol{x}-\boldsymbol{x'}|,\xi)$ - influencing kernel function or non-local modulus,
- ε_{kl} - classical strain
- u_l, u_k - displacement vectors at a reference point $\boldsymbol{x'}$,
- λ, μ - Lame's first and second parameters,
- ρ, f_l - mass and body force density.

The unit of measure of kernel function is $(length)^{-3}$ and so it depends on characteristic length ratio a/l where a and l represents internal (lattice parameter, grain size, granular distance etc.) and external (wavelength, crack length, size, dimensions of shape etc.) characteristic length, respectively. The non-local modulus could be written in the following form:

$$\alpha = \alpha(|\boldsymbol{x}-\boldsymbol{x'}|,\xi), \xi = \frac{e_0 a}{l}. \tag{3.27}$$

In Eq.(3.27) e_0 represents a constant appropriate to the material and must be determined for each material independently. Eq.$(3.26)_1$ which represents governing equation of non-local elasticity is an integro-partial differential equation. This type of equation is generally difficult to solve so it must be simplified to the differential form by introducing certain assumptions. The non-local modulus $\alpha(|\boldsymbol{x}-\boldsymbol{x'}|,\xi)$ is a Green function of linear differential operator and is written in following form:

$$L_0\alpha(|\boldsymbol{x}-\boldsymbol{x'}|,\xi) = \delta(|\boldsymbol{x}-\boldsymbol{x'}|), \tag{3.28}$$

where L_0 and δ represents linear differential operator and Dirac delta function respectively. With application of L_0 to Eq.$(3.26)_1$ we obtain:

$$L_0\sigma_{ij} = \sigma_{ij}^{c}. \tag{3.29}$$

It is worth mentioning that linear differential operator L_0 has different forms for different expressions of non-local modulus. In case of the non-local modulus represented with Eq.(3.28) in combination with Eq.(3.29) yields:

$$L_0 = 1 - l^2\xi^2\nabla^2, \tag{3.30}$$

where ∇^2 represents Laplacian operator. Using the Eq.(3.29) and Eq.(3.30) the non-local constitutive relations Eq.$(3.26)_1$ can be written in the following form:

$$(1 - \xi^2 l^2 \nabla^2)\sigma_{kl}(\boldsymbol{x}) = \sigma^2_{kl}(\boldsymbol{x}) = C_{klmn}\varepsilon_{mn}(\boldsymbol{x}), \tag{3.31}$$

where C_{klmn} is the elastic modulus tensor and ε_{mn} is the strain tensor. Generally used kernel function according to [150] can be written in the following form:

$$\alpha(|\boldsymbol{x} - \boldsymbol{x'}|, \xi) = \frac{1}{2\pi\xi^2 l^2} K_0\Big(\frac{\sqrt{|\boldsymbol{x} - \boldsymbol{x'}|}}{\xi l}\Big), \tag{3.32}$$

where K_0 is a modified Bessel function of the second kind. A role of the kernel function is to incorporate these non-local effects at reference point $\boldsymbol{x}$ which are produced by local strain at the source $\boldsymbol{x'}$ into the constitutive relations. In the kernel function the term $|\boldsymbol{x'} - \boldsymbol{x}|$ represents Euclidean distance. For a case where $\boldsymbol{x} = \boldsymbol{x'}$ the kernel function reaches maximum.

3.2.1 Non-local parameter

The non-local parameter $e_0 a$ is parameter which consist of material parameter e_0 and characteristic length a. As originally introduced in [151], the material parameter e_0 is a constant which is estimated such that the relations of the non-local elasticity model could approximate atomic dispersion curves of plane waves with those of atomic lattice dynamics. The value of e_0 can be found by developing two models of nanostructure using non-local theory and MD. By comparing results MD simulation to non-local theory the precise value of e_0 is determined. As reported in [150], different non-local parameters that are commonly used are $e_0 a$ and $e_0 a/l$. Some usual values of parameters e_0, $e_0 a$ and $e_0 a/l$ for graphene sheet are shown in Tab. 3.1.

Table 3.1: Values of parameters e_0, e_0a and e_0a/l used for graphene sheet in various research papers

Parameters	Magnitudes
e_0	0.39 [151] 0.288 [152] 0-19 [153, 154]
e_0a	0.7 nm [155] 0-2 nm [156, 157, 84] 0-2 nm [153, 154, 158] $<$ 2.1 nm [152] 0-45 nm [159]
e_0a/l	0-0.8 [160]

3.3 Mechanical Vibrations of Graphene Sheets

According to [161] vibrations can be classified by:

- the number of degrees of freedom (DOF) that is necessary for modeling the system,
- type of forcing exerted on the system, and
- assumptions used in the modeling.

Classification of vibration system in terms of DOF required for modeling the system are: discrete systems (systems that have finite degrees of freedom), single degree of freedom (SDOF) systems (systems with one degree of freedom), multiple degree of freedom (MDOF) systems (systems with two or more degrees of freedom) and continuous number of freedom systems (systems having infinite degrees of freedom systems). Since beams and plates have infinite number of degrees of freedom they are classified as continuous systems. Regarding the type of forcing exerted on the SLGS system in this thesis the following type of vibrations will be investigated from non-local plate theory standpoint and these are:

- free vibrations - vibrations that are initiated by the internal energy present in the system and no other source is present. In this case the transverse load function is equal to zero.
- forced vibrations - vibrations that are caused by an external forces or motion. There are total of three forced vibration cases considered and these are:

– the system with atmospheric pressure exerted on the system,

– the system with attached gas/vapor molecules and the atmospheric pressure acting on the system.

It should be noted that in this thesis, only the linear free and forced vibrations of graphene sheet are investigated.

3.3.1 Single Layer Graphene Sheet

The dynamic behavior of single layer graphene sheet (SLGS) with the attached gas molecules at arbitrary positions is considered using non-local elasticity theory in combination with theory of thin plates. In this investigation only completely clamped boundary condition (CCCC) is considered. Schematic illustration of SLGS with one nanoparticle attached at random position is shown in Fig. 3.3.

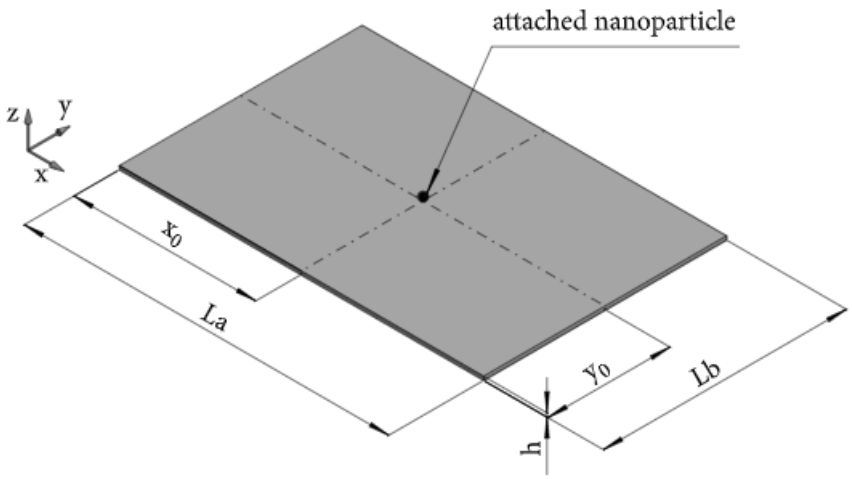

Figure 3.3: Schematic illustration of SLGS with one nanoparticle attached at random position [158].

As shown in Fig. 3.3 the coordinate system is positioned at lower left corner of SLGS with x and y axis are oriented along the L_a and L_b lengths, respectively while z axis is taken along the height of SLGS.

3.3.1.1 Derivation of Governing Equation

The stress-strain relation for orthotropic material in two dimensional form can be written as:

$$(1-(e_0a)^2\nabla^2)\begin{Bmatrix}\sigma_{xx}\\ \sigma_{yy}\\ \sigma_{xy}\end{Bmatrix}=\begin{bmatrix}\frac{E_{xx}}{1-\nu_{xy}\nu_{yx}} & \frac{\nu_{xy}E_{yy}}{1-\nu_{xy}\nu_{yx}} & 0\\ \frac{\nu_{yx}E_{xx}}{1-\nu_{xy}\nu_{yx}} & \frac{E_{yy}}{1-\nu_{xy}\nu_{yx}} & 0\\ 0 & 0 & G_{xy}\end{bmatrix}\times\begin{Bmatrix}\varepsilon_{xx}-\alpha_x\Delta T\\ \varepsilon_{yy}-\alpha_y\Delta T\\ 2\varepsilon_{xy}\end{Bmatrix}, \tag{3.33}$$

where E_{xx} and E_{yy} are the elastic moduli in x and y direction, respectively, while G_{xy} is shear modulus. The ν_{xy} and ν_{yx} are Poisson's ratios and α_x, α_y are thermal expansion coefficients in x and y directions, respectively. The differential equation of motion [157] for SLGS can be written as:

$$\begin{aligned}&D_{11}\frac{\partial^4 w}{\partial x^4}+2(D_{12}+2D_{66})\frac{\partial^4 w}{\partial x^2\partial y^2}+D_{22}\frac{\partial^4 w}{\partial y^4}\\ &-q(x,y,t)+\rho h\frac{\partial^2 w}{\partial t^2}-N_{xx}^T\frac{\partial^2 w}{\partial x^2}-N_{yy}^T\frac{\partial^2 w}{\partial y^2}+\\ &(e_0a)^2\frac{\partial^2}{\partial x^2}\Big[q(x,y,t)-\rho h\frac{\partial^2 w}{\partial t^2}+N_{xx}^T\frac{\partial^2 w}{\partial x^2}+N_{yy}^T\frac{\partial^2 w}{\partial y^2}\Big]+\\ &(e_0a)^2\frac{\partial^2}{\partial y^2}\Big[q(x,y,t)-\rho h\frac{\partial^2 w}{\partial t^2}+N_{xx}^T\frac{\partial^2 w}{\partial x^2}+N_{yy}^T\frac{\partial^2 w}{\partial y^2}\Big]=0,\end{aligned} \tag{3.34}$$

where w represents displacement in z direction, t is time, ρ is mass density, and N_{xx}^T and N_{yy}^T are thermal resultant forces. The D_{11}, D_{12}, D_{22} and D_{66} represent bending rigidity coefficients which can be written in the following form

$$\begin{aligned}D_{11}&=\frac{E_{xx}h^3}{12(1-\nu_{xy}\nu_{yx})}, D_{12}=\frac{\nu_{xy}E_{yy}h^3}{12(1-\nu_{xy}\nu_{yx})},\\ D_{22}&=\frac{E_{yy}h^3}{12(1-\nu_{xy}\nu_{yx})}, D_{66}=\frac{G_{xy}h^3}{12}.\end{aligned} \tag{3.35}$$

In previous equations the variable $q(x,y,t)$ represents transverse force per unit area. Here three different types of transverse vibrations of the SLGS are considered and these are:

- transverse vibrations of SLGS in presence of atmospheric pressure,
- transverse vibrations of SLGS with attached gas/vapor molecule without atmospheric pressure, and
- transverse vibrations of SLGS with attached gas/vapor molecule with atmospheric pressure.

These three cases can be written in the following form:

$$\begin{aligned} q(x,y,t) &= -\Big(P_{atm}A\Big)\frac{\partial^2 w}{\partial t^2}, \\ q(x,y,t) &= -\Big(\sum_{j=1}^{N_1} m_j\delta(x-x_j,y-y_j)\Big)\frac{\partial^2 w}{\partial t^2}, \\ q(x,y,t) &= -\Big(P_{atm}A+\sum_{j=1}^{N_1} m_j\delta(x-x_j,y-y_j)\Big)\frac{\partial^2 w}{\partial t^2}, \end{aligned} \tag{3.36}$$

where m_j represents mass of attached gas/vapor molecule, P_{atm} atmospheric pressure, A SLGS area on which atmospheric pressure acts and $\delta(x-x_j,y-y_j)$ is a two dimensional Dirac delta function. The properties of this function can be written in the following form:

$$\begin{aligned} &\delta(x-x_j,y-y_j)=0,(x,y)\neq(x_j,y_j), \\ &\int_{-\infty}^{\infty}\int_{-\infty}^{\infty}\delta(x-x_j,y-y_j)=1. \end{aligned} \tag{3.37}$$

The N_{xx}^T and N_{yy}^T represents thermal resultant force due to temperature difference ΔT and can be written in following form:

$$\begin{aligned} N_{xx}^T &= -\frac{E_{xx}(\alpha_x+\nu_{xy}\alpha_y)}{1-\nu_{xy}\nu_{yx}}h\Delta T, \\ N_{yy}^T &= -\frac{E_{yy}(\alpha_y+\nu_{xy}\alpha_x)}{1-\nu_{xy}\nu_{yx}}h\Delta T, \end{aligned} \tag{3.38}$$

where h represents the thickness of graphene sheet. Eq.(3.34) can be converted to eigenvalue problem by substituting the following equation:

$$w(x,y,t)=W(x,y)e^{i\omega t}, \tag{3.39}$$

where ω represents the angular frequency and $i=\sqrt{-1}$ represents imaginary unit number, and $W(x,y)$ represents the shape function of deflection. Substituting previous equation

into Eq.(3.34) the following equation is obtained:

$$\begin{aligned}
&D_{11}\frac{\partial^4 W}{\partial x^4} + 2(D_{12}+2D_{66})\frac{\partial^4 W}{\partial x^2 \partial y^2} + D_{22}\frac{\partial^4 W}{\partial y^4} \\
&- q(x,y)\omega^2 W - \omega^2 \rho h W - N_{xx}^T \frac{\partial^2 W}{\partial x^2} - N_{yy}^T \frac{\partial^2 W}{\partial y^2} + \\
&(e_0 a)^2 \frac{\partial^2}{\partial x^2}\left[\omega^2 q(x,y)W + \omega^2 \rho h W + N_{xx}^T \frac{\partial^2 W}{\partial x^2} + N_{yy}^T \frac{\partial^2 W}{\partial y^2}\right] + \\
&(e_0 a)^2 \frac{\partial^2}{\partial y^2}\left[\omega^2 q(x,y)W + \omega^2 \rho h W + N_{xx}^T \frac{\partial^2 W}{\partial x^2} + N_{yy}^T \frac{\partial^2 W}{\partial y^2}\right] = 0.
\end{aligned} \tag{3.40}$$

3.3.1.2 Natural Vibrations of SLGS

In order to investigate free vibrations of SLGS mass nanosensor Galerkin method is utilized to solve Eq.(3.40). Only one boundary condition is considered and this is completely clamped boundary condition (CCCC). The solution function for CCCC boundary condition is given in Tab. 3.2.

Table 3.2: Mathematical formulations for CCCC boundary condition

Mode Shape Function	Mathematical Form of Boundary Conditions
$W(x,y) = A_{mn}\left(\cos\left(\frac{2m\pi x}{L_a}\right)-1\right)\left(\cos\left(\frac{2n\pi y}{L_b}\right)-1\right)$	$w(0,y,t) = w(L_a,y,t) = 0$ $w(x,0,t) = w(x,L_b,t) = 0$ $\frac{\partial w(0,y,t)}{\partial x} = \frac{\partial w(L_a,y,t)}{\partial x} = 0$ $\frac{\partial w(x,0,t)}{\partial y} = \frac{\partial w(x,L_b,t)}{\partial y} = 0$

3.3.1.3 Free Vibration SLGS System

Here the frequency equation are derived for the free SLGS system with CCCC boundary condition. To obtain this frequency equation the mode shape functions from Tab. 3.2 are utilized. Consider SLGS with CCCC boundary condition without any transverse load acting on it. This means that the transverse load function $q(x,y)$ is zero. In order to obtain the frequency equation of SLGS with CCCC boundary condition the mode shape function given in Tab. 3.2 must be substituted in the Eq.(3.40). After substitution the equation is multiplied with $\left(\cos\left(\frac{2m\pi x}{L_a}\right)-1\right)\left(\cos\left(\frac{2n\pi y}{L_b}\right)-1\right)$ and integrated over whole region ($x \in [0, L_a], y \in [0, L_b]$). After further manipulation the frequency equation is

obtained which can be written in following form:

$$\omega_{mn}^2 = \frac{D_{11}\frac{3m^4\pi^4}{L_a^4} + 2(D_{12}+2D_{66})\frac{m^2n^2\pi^4}{L_a^2L_b^2} + D_{22}\frac{3n^4\pi^4}{L_b^4}}{\frac{3h\rho}{4}\left(\frac{3}{4}+(e_0a)^2\pi^2\left(\frac{m^2}{L_a^2}+\frac{n^2}{L_b^2}\right)\right)} + \frac{N_{xx}^T\left(\frac{m^2\pi^2}{L_a^2}\left(\frac{3}{4}+(e_0a)^2\pi^2\left(\frac{3m^2}{L_a^2}+\frac{n^2}{L_b^2}\right)\right)\right)}{\frac{3h\rho}{4}\left(\frac{3}{4}+(e_0a)^2\pi^2\left(\frac{m^2}{L_a^2}+\frac{n^2}{L_b^2}\right)\right)} + \frac{N_{yy}^T\left(\frac{n^2\pi^2}{L_b^2}\left(\frac{3}{4}+(e_0a)^2\pi^2\left(\frac{m^2}{L_a^2}+\frac{3n^2}{L_b^2}\right)\right)\right)}{\frac{3h\rho}{4}\left(\frac{3}{4}+(e_0a)^2\pi^2\left(\frac{m^2}{L_a^2}+\frac{n^2}{L_b^2}\right)\right)}. \tag{3.41}$$

3.3.1.4 Vibrations of SLGS with CCCC boundary condition

As mentioned earlier if vibrations of the system are caused by external forces or motion, vibrations of the system are classified as forced vibration. So in this case the transverse load $q(x,y,t)$ is acting on SLGS plate. It should be noted if the external excitation is causing the system to oscillate at the frequency which is close to a natural frequency of the system this frequency is called resonant frequency. The analytical solution of governing equation Eq.(3.40) in case where only attached molecules are considered for SLGS with CCCC boundary condition can be found by substitution of mode shape function from Tab. 3.2 for CCCC case into the Eq.(3.40) and $q(x,y)$ from Eq.$(3.36)_3$, respectively. Multiplying the equation with $\left(\cos\left(\frac{2m\pi x}{L_a}\right)-1\right)\left(\cos\left(\frac{2n\pi y}{L_b}\right)-1\right)$ and integrating the equation over the whole region with respect to x,y in range $x\in[0,L_a], y\in[0,L_b]$ the frequency equation for forced vibration is obtained and can be written in the following form

$$\omega_{mn}^2 = \frac{D_{11}\frac{4m^4\pi^4}{L_a^4} + 2(D_{12}+2D_{66})\frac{4m^2n^2\pi^4}{3L_a^2L_b^2} + D_{22}\frac{4n^4\pi^4}{L_b^4}}{X_{CCCCPATM}} + \frac{\frac{4N_{xx}^T(e_0a)^2\pi^4}{L_a^2}\left(\frac{m^2}{L_a^2}+\frac{n^2}{3L_b^2}\right)}{X_{CCCCPATM}} + \frac{N_{yy}^T\left(\left(\frac{m^2}{L_a^2}+\frac{n^2}{L_b^2}\right)\left(\pi^2+\frac{4n^2(e_0a)^2\pi^4}{L_b^2}\right)\right)}{X_{CCCCPATM}}, \tag{3.42}$$

where coefficient $X_{CCCCPATM}$ can be written as

$$X_{CCCCPATMM} = \frac{3PA}{4}\left(\frac{3}{4} + (e_0 a)^2\pi^2\left(\frac{m^2}{L_a^2} + \frac{n^2}{L_b^2}\right)\right) + \frac{3h\rho}{4}\left(\frac{3}{4} + (e_0 a)^2\pi^2\left(\frac{m^2}{L_a^2} + \frac{n^2}{L_b^2}\right)\right) + \frac{1}{4}\sum_{j=1}^{N_1}\frac{m_j}{L_a L_b} - \frac{1}{2}\sum_{j=1}^{N_1}\frac{m_j}{L_a L_b}\cos\left(\frac{2mx_j}{L_a}\right) - \frac{1}{2}\sum_{j=1}^{N_1}\cos\left(\frac{2n\pi y_j}{L_b}\right) \left(\frac{1}{4} + (e_0 a)^2\pi^2\left(\frac{m^2}{L_a^2} - \frac{n^2}{L_b^2}\right)\right)\sum_{j=1}^{N_1}\frac{m_j}{L_a L_b}\cos^2\left(\frac{m\pi x_j}{L_a}\right)\cos^2\left(\frac{n\pi y_j}{L_b}\right) \tag{3.43}$$

As seen from Eq.(3.43) the coefficient contains the pressure exerted on the SLGS system with attached mass. In case where only the influence of pressure exerted on the SLGS system the mass in the Eq.(3.43) is equal to zero and in the case were mass is attached on the surface of SLGS without atmospheric pressure in the Eq.(3.43) the pressure is equal to zero.

4. Artificial Intelligence Algorithm

In this chapter Artificial Intelligence (AI) algorithm used in this thesis will be described in detail. The AI algorithm that is utilized is Genetic Programming (GP) algorithm for generating symbolic expressions between input and desired output parameters. In this particular instance, GP will be used to obtain symbolic expression for determining non-local parameter of analyzed system. In order to obtain this mathematical equation the dataset will be required and the dataset will be provided from MD simulations and non-local theory.

4.1 Genetic Programming Algorithm

GP, which is a type of evolutionary computation (EC), is a technique that automatically solves a problem without human interference. In general GP can be categorized as a systematic and domain-independent method which utilize computational resources in order to solve problems automatically starting from a high-level statement of what needs to be done. In GP the population of computer programs are evolved from generation to generation and a goal is to obtain computer program which most accurately describes the analyzed physical problem. A simple flow chart of genetic algorithm is shown in Fig. 4.1.

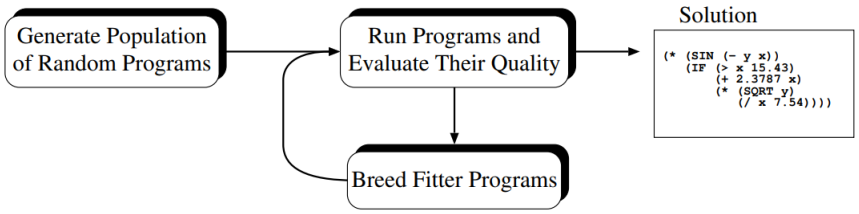

Figure 4.1: Flow chart of genetic programming algorithm [162].

4.1.1 The basics of GP Algorithm

In order to explain the inner workings of GP algorithm the basic tools and terminology used in GP programming must be described in detail.

4.1.2 Representation

In GP, programs are represented as syntax trees. For example, in Fig. 4.2 the tree representation of the program $(X_1 - 1) - ((X_1 - X_0).(X_0 + X_1))$ is shown.

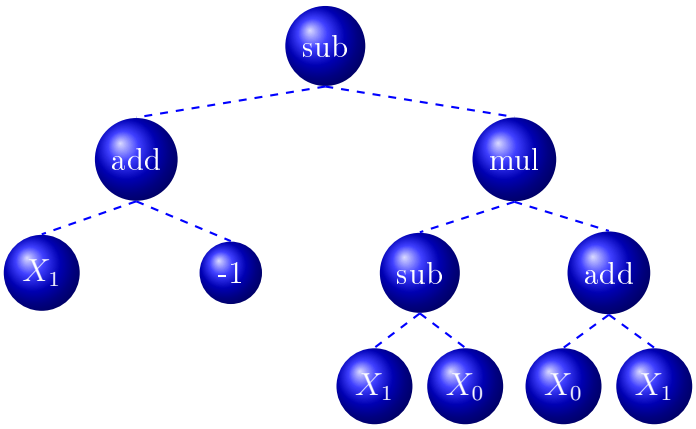

Figure 4.2: GP program tree representation of $(X_1 - 1) - ((X_1 - X_0) \cdot (X_0 + X_1))$

As seen from Fig. 4.2 the variables and constants represent leaves of the tree while the arithmetic operations are internal tree nodes. The tree representation shown in 4.2 consists of set of trees which are grouped together under one "root" node that acts as a glue. Generally GP algorithm randomly generates the program using tree gene sets. The variables (X_0, X_1) and constants (-1) in the program are stored in terminals gene set. The arithmetic operations in the program $(+, -, *)$ are stored in functions gene set. The functions and terminals together form the primitive set of GP.

4.1.2.1 Terminal Set

The terminal set consist of:

- the program external input variables i.e. $X_0, X_1, X_2, ..., X_n, y$,
- functions with no arguments - these functions do not require any input variable and each time they return different value. In Python programming language there is the random() function for example, and
- constants - randomly generated number in the tree creation process or created by mutation.

The list of examples of terminal set used in GP is shown in Tab. 4.1.

Table 4.1: Examples of GP Terminal Set

Terminal Set	
Kind of Primitive	Example
Variables	$X_0, ..., X_n, y$
Constant values	1, 1.5 , 2
zero arity functions	random (rand)

4.1.2.2 Function Set

A function set generally depends on the nature of the problem that is being solved using GP. If it is a simple numeric problem then the function set should consist of simple arithmetic functions such as addition, subtraction, multiplication and division. However, if a nature of the problem is more complicated then the function set should consists of more advanced functions. In general, before implementing GP algorithm the complexity of the problem must be determined. The list of functions, that are commonly used in GP function sets is given in Tab. 4.2.

Table 4.2: Examples of GP Function Set

Function Set		
Kind of Primitive	Example	Arity[1]
Arithmetic	addition (+)	2
	subtraction (-)	2
	multiplication (*)	2
	division (/)	2
Mathematical	Square root (sqrt)	1
	Logarithm (log)	1
	Absolute value (abs)	1
	Negative (neg)	1
	Inverse (inv)	1
	Maximum (max)	2
	Minimum (min)	2
	Sine (sin)	1
	Cosine (cos)	1
	Tangent (tan)	1
Boolean	and	2
	or	2
	not	1

The arity in Tab. 4.2 represent the arity of a function or operation that is the number of arguments or operands the function or operation accepts [163].

4.1.3 Initializing the Population

In genetic algorithms there are two types of population initialization and these are: random and heuristic initialization. The random initialization is the method in which the initial population is filled with randomly chosen members. The method is frequently used and population diversity is higher when compared to other methods. The heuristic initialization is method in which initial population is filled by applying some heuristic method. The disadvantage of using this method is lower population diversity. In GP the individuals of initial population are usually randomly generated. Today, there are a number of different approaches for generating random initial population but three methods that are most commonly used are: full, grow and ramped half-and-half method. The full and grow methods are the most basic methods used while ramped half-and-half is today most commonly used method. This method is the combination of the full and grow method.

4.1.3.1 The Full and Grow Method

The full and grow methods are the first and basic methods used for construction of initial population in GP. The individuals in the initial population are generated considering the limitation of user specified maximum tree depth. The depth of tree node is defined as the number of the edges that need to be traversed in order to reach the node starting from root node. The root node is assumed to be at depth 0. So the depth of the tree is the depth of its deepest leaf. The full method is named because this method generates full trees meaning all leaves are at the same depth. The nodes are randomly selected from the function set until the maximum tree depth is reached. After the function set reached the maximum tree depth only terminals could be chosen. In Fig. 4.3 the construction of population member is shown using the full method with tree depth of 2.

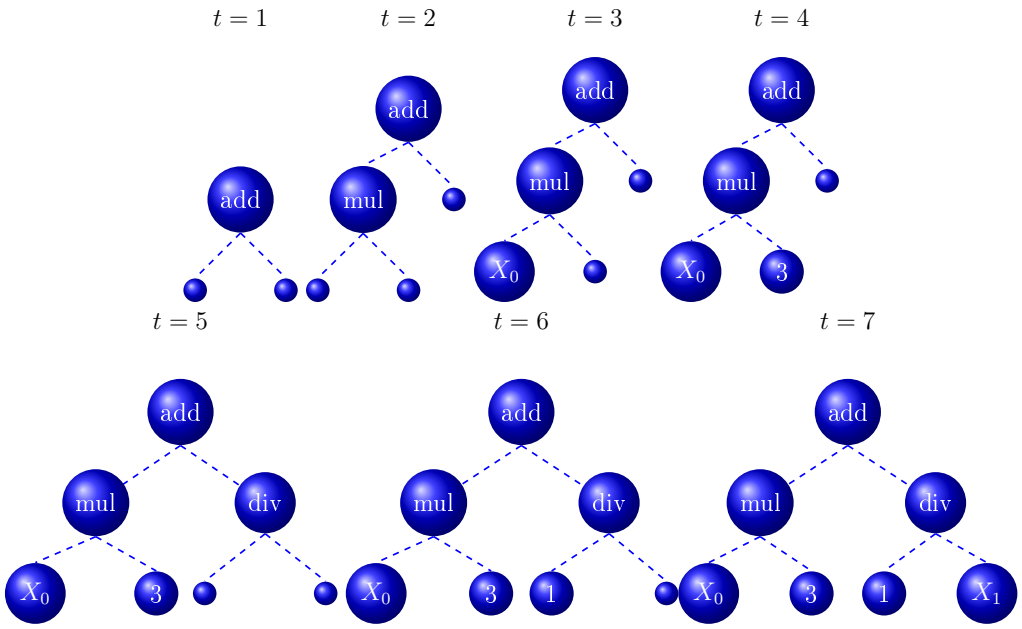

Figure 4.3: Creation of a six node tree using full method

In Fig. 4.3 the variable t represent steps in population member initialization. As seen from Fig. 4.3 the full method reaches the maximum depth with randomly selecting the functions. After the maximum depth is reached the members from terminal set are chosen as leaves. Otherwise the tree would be too deep. Using full method the generated trees will have leaves at the same depth. However, it is not guaranteed that these trees will have the same number of nodes or the same shape. Here a key factor is function arity. If the arity of all functions used is the same then all the trees in initial population will have the same shape. Even if mixed-arity primitive sets are used, the range of program sizes and shapes produced using full method may be limited.

The grow method is slightly better than the full method in terms of creating trees with more varied sizes and shapes. In grow method the nodes are selected from the whole primitive set meaning functions and terminals until the depth limit is reached. When the depth is reached the elements from terminal sets are chosen. In Fig. 4.4 the construction process of tree using grow method is shown with the tree depth of 2. The variable t represents the steps in population member initialization.

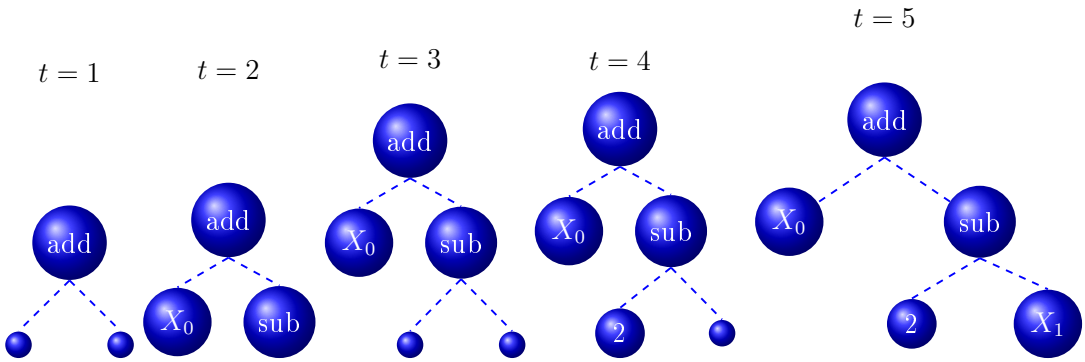

Figure 4.4: Creation of five node tree using grow method.

4.1.3.2 Ramped half-and-half method

The main disadvantage of the full and grow method is the very wide range of sizes and shapes of tree structures they produce. The ramped half-and-half method [164] is combination of full and grow method. The idea of this method is to ensure that the initial population consists of trees having a variety of sizes and shapes. A half of initial population is constructed using full and the other half is constructed using grow method.

4.1.4 Fitness Function

So far the methods for creating initial population have been explained. The next step is to describe the method of evaluating population members. In any evolutionary algorithm (EA) this is a crucial step because the fitness function gives measure of quality to each population member. In other words, the fitness function gives information of how good each population member is a solution of the specific problem. There is no specific method for determining the quality of each population member and it depends on problem. For example, the fitness measure can be the amount of error between calculated output and desired output, the time needed for a system to reach the desired state, the population member accuracy in pattern recognition or object classification, the output that population member produces and user specified design criteria. The fitness function in GP is more complex from other EA fitness functions. Since in GP the population members are tree structures these members must be interpreted correctly, before evaluation. This means that node execution must be performed in specific order which guarantees that nodes are not executed before the value of their arguments is known. There are two methods for population members tree evaluation based on starting point and these are from root node and from leaves. These two methods are equivalent and must traverse the tree recursively. In Fig. 4.5 the example of syntax tree is shown for equation $3 \cdot X_0 + \frac{4}{X_1}$ where $X_0 = -1$ and $X_1 = 2$.

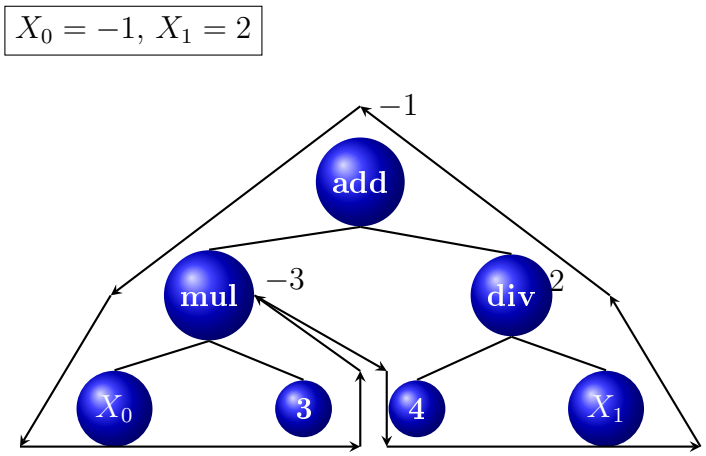

Figure 4.5: Interpretation of a syntax tree

4.1.5 Selection

In the GP as in other EA, genetic operations are applied on individuals that are selected based on their fitness value. Generally, the individuals with better fitness value will have more children than those with inferior fitness value. Commonly used methods for selecting population members are:

- fitness proportionate selection - in this selection method any individual can become a parent with probability which is proportional to its fitness value. Fitter individuals have higher chance of mating and propagating their features to the next generation. There are two types of fitness proportionate selection and these are Roulette Wheel Selection and Stochastic Universal Sampling,

- rank selection - this selection method is used when population members have very close fitness values which generally leads to individuals having an almost equal chance of selection when utilizing fitness proportionate selection. The concept of fitness value is removed in this method and then every population member receives fitness from this ranking. Now selection of parents depends on the rank of each population member not the fitness value,

- tournament selection - generally this selection method is used when dealing with huge number of population members. In this method two of population members are randomly selected from the population and compared to each other. Based on comparison the best of them is chosen to be the parent, and

- random selection - the parents are randomly selected from existing population.

In GP the tournament selection is commonly used. As mentioned earlier, in this method, two or more individuals from population are selected and compared. Those with better fitness value will be selected as parents of next generation.

4.1.6 Crossover and Mutation

In GA there are two main genetic operators that are responsible for creating diversity in population and these are crossover and mutation. Crossover (recombination) is genetic operator which is used to combine genetic material from two parents in order to generate new offspring. The mutation is genetic operator which is used to randomly modify population member. Both of these genetic operators are used to maintain genetic diversity in GA. In GP both of these operators are used in order to generate computer programs for next generation and they will be described in detail.

4.1.6.1 Crossover

The crossover is variational operator in EA that requires two or more parents and genetic material from two or more parents is used to create offspring. Although the principle of crossover is the same in GP the implementation of this operator is slightly different from other EA. The most common type of Crossover used in GP is Subtree Crossover. The tournament for this variational operations must be ran twice in order to find parents. First the algorithm randomly selects the subtree on both parents. Then the subtree is copied form second parent and replaces existing subtree on first parent. The process of subtree crossover is shown in Fig. 4.6.

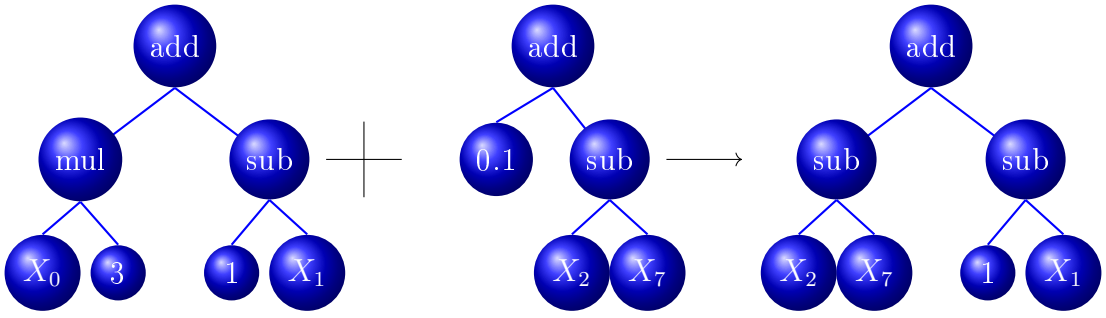

Figure 4.6: Subtree crossover example

4.1.6.2 Mutation

According to [165] there are three types of mutation and these are Subtree Mutation, Hoist Mutation and Point Mutation. The Subtree Mutation compared to other types of mutation is most agressive mutation operation because more genetic material is replaced

by naive random components. This mutation method could improve diversity by reintroduction of extinct mathematical functions. In Fig. 4.7 the example of subtree mutation process is shown.

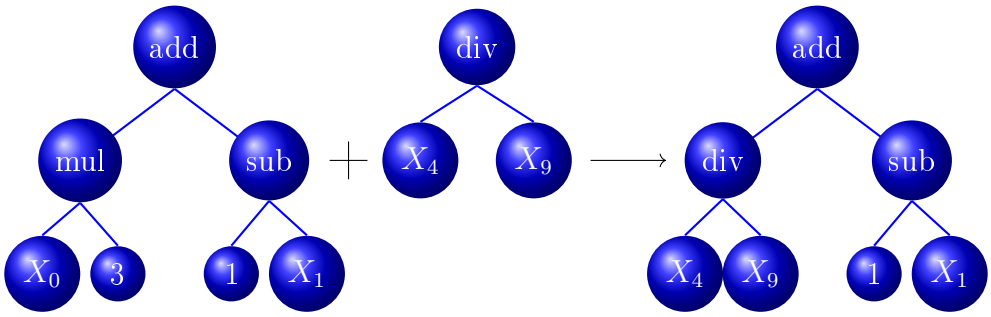

Figure 4.7: Subtree mutation example

The general purpose of hoist mutation is to eliminate some genetic material from tournament winners. In this mutation method the random subtree is selected from tournament winner. Then random subtree of that subtree is than selected and hoisted in the original subrees location in order to form an offspring in the next generation. The process of hoist mutation is shown in Fig. 4.8.

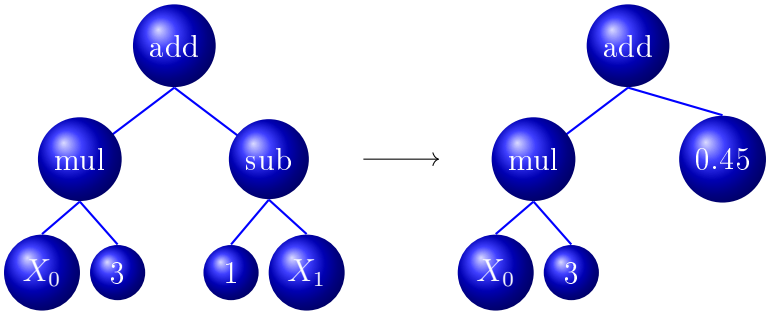

Figure 4.8: Hoist mutation example.

The most common type of mutation is point mutation method. As in the case of subtree mutation, the method can introduce extinct functions and operators in order to improve population diversity. In this method random nodes are selected for replacement on the tournament winner. Selected terminals are replaced by other terminals and functions by other functions. The procedure of point mutation is shown in Fig. 4.9.

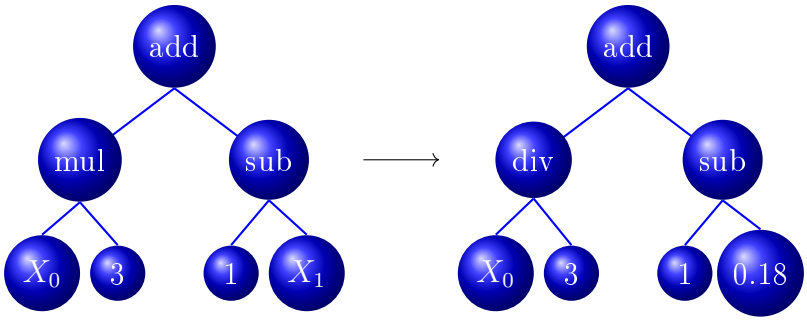

Figure 4.9: Point mutation example

4.1.7 Termination Criteria

Termination criteria is one of the most important parts of any EA. If not specified, the algorithm could run indefinitely. Generally in EA the termination criteria tells the algorithm when to stop the execution. According to [166] there are number of termination criteria and these are:

- Maximal Time Budget - this criteria is based on time budget consumed which can be defined as an absolute time or the CPU-time. When EA runs the predetermined execution time it returns the final solution,
- Maximal Number of Generations - as the name states the EA runs for predetermined number of generations or iterations and then returns final solution,
- Maximal Number of Fitness Function Evaluation - when EA reaches predefined number of fitness function evaluations it stops the execution.,
- Hitting a Bound - this criteria is fulfilled when EA fitness function reaches predefined value.
- K-iterations - this criteria is fulfilled if there is no improvement in solution after K-iterations.

In GP the maximum number of generations and hitting a bound are used together as termination criteria. Since complexity of the problem could not be estimated at first there is usually best to perform couple of test in order to better specify these two parameters.

5. MD Simulations

In this chapter, the procedure and results obtained using MD simulations will be described in detail. First, the mechanical properties of the SLGS structure using MD will be determined, such as the elastic and shear modulus and Poisson's ratio by performing a uniaxial test and shear test, respectively. Coefficients of thermal expansion in x and y-direction will be determined after the models are equilibrated at a specific temperature and pressure. The reason for performing these analyses lies in the fact that SLGS structure is considered, as a sensing element of nanosensor, for the detection of gas/vapor molecules. Usually, commercially available sensors have a strictly specified temperature and pressure range in which they could be utilized. So for each temperature and pressure, the mechanical and thermodynamic properties of this material must be determined. Secondly, the natural frequencies of the SLGS structure will be determined using MD simulation in combination with the FFT algorithm. The main result of MD simulations is the amplitude versus time of the central atom in the SLGS structure. To transform the amplitude versus time signal into amplitude versus frequency signal and to determine the natural frequency of vibrating structure the FFT will be utilized. The natural frequencies will be excited using the velocity excitation method. Finally, investigation of the absolute and relative frequency shift caused by attached gas/vapor molecules on the SLGS surface will be described.

5.1 LAMMPS Simulation

The MD simulations were performed using Large scale Atomic/Molecular Massively Parallel Simulator (LAMMPS) [167]. To run the LAMMPS MD simulation first the input script must be created. In most cases, the LAMMPS input script can be divided into four parts, and these parts are:

- Initialization,
- Atom definition,
- Settings, and

Table 5.1: The list of metal physical quantities and their measuring unit

Physical variable	Measurement unit
mass	g/mol
distance	Å
time	ps
energy	eV
velocity	Å/ps
force	eV / Å
torque	eV
temperature	K
pressure	bar
dynamic viscosity	Poise
charge	multiple of electron
dipole	charge * Å
electric field	V/ Å
density	$\frac{g}{cm^i}$ where $i = 1, 2, 3$

- Parameters for simulation run.

5.1.1 Initialization

In the first part of the LAMMPS input script, the parameters such as units, dimensions, simulation box boundaries, and atom style must be defined. The LAMMPS offers a variety of unit systems used in MD simulations, and these are *lj*, *real*, *metal*, *si*, *cgs*, *electron*, *micro*, and *nano*. All the analyses in this thesis will be conducted with metal units style, and units for each physical quantity for that style, are listed in Tab. 5.1. The REBO interatomic potential that was used in these investigations is created in metal units so if the other unit style was utilized then interatomic potential must be recalculated. Each units style has its own default value of timestep size and its skin distance. For metal units default values of the timestep size and skin distance are 0.001 ps and 2.0 Å, respectively. The next step is to define dimensions of the MD simulation system using dimension command. This command defines the dimensionality of the system and default LAMMPS input script if no dimension command is specified runs 3D simulations. In order to run a 2D simulation the dimension command must be used before specifying the simulation box using the *create_box* or *read_data* commands. In this thesis all analyses were conducted using a 3D simulation box. Boundary command defines boundaries for the global

simulation box in each dimension. With the atom style command, the style of atoms which will be used in simulation and what attributes are associated with the atoms are defined. This command must be defined before setting up the simulation box. Once a style is assigned, it cannot be changed later in the input script. For example, if atomic atom style is defined in the input script the bond and angular terms cannot be used or later added to the model. The choice of atom style defines what quantities can be stored by each atom, what quantities are exchanged by processors in the multiprocessing simulation, and what quantities are stored in the geometry data file. All the analyses were conducted with atom style atomic.

5.1.2 Atom Definition

The LAMMPS simulation package offers three ways in defining the atoms of the MD system and these are:

1. read them from the external document which contains molecular topology information using *read_ data* command. The molecular toplogy is usually built in other program packages such as: Visual Molecular Dynamcs (VMD) [168], Avogadro [169] etc.,

2. read them from the restart file which contains molecular topology information using *read_ restart* command and

3. creating atoms on a lattice using following commands: *lattice*, *region*, *create_ box* and *create_ atoms*. After building initial set of atoms these atoms can be duplicated using replicate command.

In this thesis, for initial equilibration of SLGS structures, the molecular topology is created using the VMD software package. After equilibration simulation, the restart file is created, which is then used in a simulation of uniaxial, shear tests, and vibration simulation.

5.1.3 Settings

After the initialization step and atom definition of the model in LAMMPS input script are defined, the next and most important step is to define the settings of simulation. So in this section, the variety of settings could be defined, such as force field coefficients, simulation parameters, and output options. The force field coefficients that could be defined depending on the atom style in initialization step defined are: *pair_ coeff*, *bond_ coeff*, *angle_ coeff*, *dihedral_ coeff*, *improper_ coeff* etc.. Various boundary conditions, ensembles, time integration and diagnostic options are defined using fix commands which will be

explained in further analyses in detail. Various computations are specified for execution during MD simulation using *compute*, *compute_ modify* and *variable* command. Using *thermo*, *dump* and *restart* commands will result with various type of output information. With *thermo* command, the simulation values such as step, temperature, energy are displayed in terminal or command prompt during MD simulation. The data command is used to save data of MD simulation in the new document.

5.1.4 Parameters for Simulation Run

After the definition of initialization, atom definition, and settings of MD simulation the final step is to define parameters for the simulation run. In order to successfully execute the simulation, if all previous parts are correctly defined, is to define the number of iteration steps. The number of iteration steps of MD simulation is defined with the *run* command followed by the integer value representing the total number of iteration steps. In this thesis, the equilibration simulation of SLGS structure at a specific temperature and pressure are performed for 1000000 iteration steps. As mentioned earlier the timestep used for metal units is 0.001 ps. So, the equilibration simulation is conducted for 1000 ps. The mechanical tests such as uniaxial test in x and y-direction and shear test are performed for 300000 iteration steps or 300 ps. The vibration analysis after equilibration consists of two simulations and these are vibration excitation and free vibration. The vibration excitation using the velocity excitation method is performed for 200000 iteration steps (200 ps) while the free vibration is performed for 1000000 iteration steps (1000 ps).

5.2 Generating Graphene Sheet Models

One of the key components in MD is the geometric model of nanostructure that will be used. All models that are used in these investigations were generated using VMD Carbon / Boron Nitride Nanostructure Builder Plugin, which is included in VMD software. Besides the graphene sheets, this plugin allows the construction of carbon and boron nitride nanostructures. Based on user input, this plugin computes the carbon atom positions with the option to generate topology information suitable for classical force field MD simulations, and these topologies, are stored in a file of suitable format. In Chapter 2, it was mentioned there are two variants of graphene sheet depending on the edge type, and these are armchair and zigzag. The SLGSA model has the armchair edge in one direction and zigzag edge in another direction, while the SLGSB model has the zigzag edge in one direction, and armchair edge in another direction. In this thesis for determination of mechanical properties different models were generated, and these were named SLGSA and SLGSB model with dimensions 10×5 nm, Fig. 5.1.

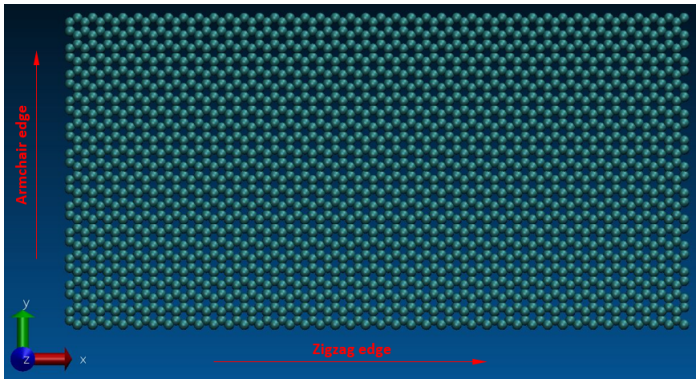

(a) SLGSA model

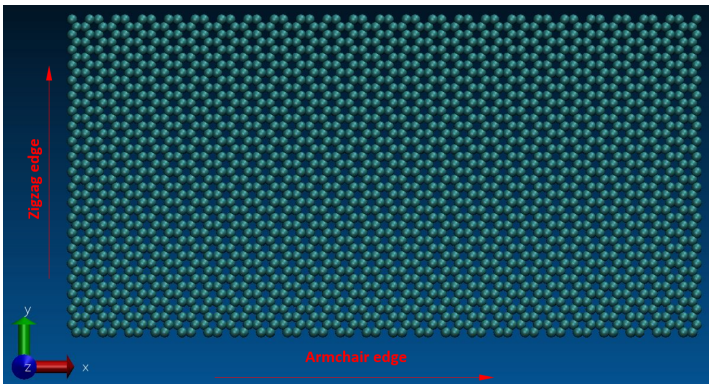

(b) SLGSB model

Figure 5.1: The SLGSA and SLGSB model generated in VMD with dimensions 10×5 nm

As seen in Fig. 5.1, the SLGSA model has a zigzag edge in x-direction and armchair edge in y-direction. The SLGSB model has the armchair edge in x-direction, and zigzag edge in y-direction. Initial investigation of natural frequencies showed that the SLGSA and SLGSB model with dimensions of 10×5 nm is too small for this kind of investigation since the value of natural frequency is wildly fluctuating (almost 100 GHz) so it can not be used for detection of gas/vapor molecules. Additional SLGSA and SLGSB models were created for natural frequency investigation in terms of size and these are 20×10, 30×15, and 40×20 nm so the total of 6 models were created.

5.3 Determination of Mechanical Properties of Graphene Sheet using MD

In this section, the mechanical properties of SLGSA and SLGSB model, are obtained utilizing MD, and these are: Young's modulus along x and y-direction, shear modulus G_{xy}, Poisson's ratio ν_{xy} and coefficients of thermal expansion α_x and α_y. Since the nanosensor

for the detection of gas/vapor molecules will be used at different atmospheric conditions, the mechanical and thermodynamic properties must also be obtained at specific temperatures and pressures. The considered temperature range in these analyses is from 233.15 up to 313.15 K with temperature step of 10 K. The step of 10 K between each temperature was defined since in MD simulation during equilibration and later in mechanical simulations the temperature tends to fluctuate significantly so if the deference between temperature is smaller it would generate almost equal results in terms of mechanical and thermodynamic parameter values. The initial approach was to investigate the influence of pressure on mechanical properties of SLGSA and SLGSB. However, the initial investigation showed that pressure fluctuations are two large so the investigation of mechanical parameters with different pressures will be omitted from these analyses. The investigation of mechanical parameters as well as vibration analysis were conducted using REBO interatomic potential.

Before investigating mechanical and thermodynamic properties of the SLGSA and SLGSB model the system must be equilibrated at given temperatures and pressure. All structures were equilibrated in a time period of 1000 ps using NPT ensemble with Nose-Hoover barostat. The time step was set to 0.001 ps (1 fs), and equilibration simulation was carried out for 1000000 iterations. The goal was to investigate mechanical properties at temperatures ranging from 233.15 to 313.15 K. This is a hypothetical working temperature range of the SLGS nanosensor, so a total of 9 different temperatures were considered for these simulations (equilibrations). The temperature during equilibration using the NPT ensemble was set to a specific temperature and adjusted every 100 iterations or 0.1 ps, as recommended in LAMMPS [170]. For analyses without atmospheric pressure exerted on the system the boundaries in x, y, and z direction were set to periodic, and the pressure was set to 0 bar. The adjustment of pressure in x and y-direction was set to 0.5 ps while in z direction was set to 1000 ps. Usually, the pressure is adjusted according to LAMMPS manual [170] every 1000 ps. However, in the case of pressure in x and y-direction such fast adjustment of pressure is required so that the simulation walls coincide with structure boundaries. The idea for performing such adjustment is to simulate an infinite graphene sheet since the boundaries in x and y-directions are periodic. In Tab. 5.2, the list of SLGSA and SLGSB models equilibration and mechanical test simulations using different interatomic potentials at different temperatures and pressures is presented.

Table 5.2: The list of SLGSA and SLGSB equilibrations and mechanical simulations using REBO interatomic potential at different temperatures and 0 [bar] pressure.

Material Type	Temperature range [K]	Type of mechanical test	
SLGSA	233.15, 243.15, 253.15, 263.15, 273.15, 283.15, 293.15, 303.15, 313.15	Uniaxial test in x and y direction	Shear test
SLGSB			

As seen from Tab. 5.2, the total number of equilibration simulations performed is 18 for SLGSA and SLGSB models with REBO potential for temperatures in a range from 233.15 up to 313.15 K and at pressure of 0 bar. In Fig. 5.2, the temperature fluctuations from equilibration simulation of the SLGSA model with REBO potential at 303.15 K and 0 bar.

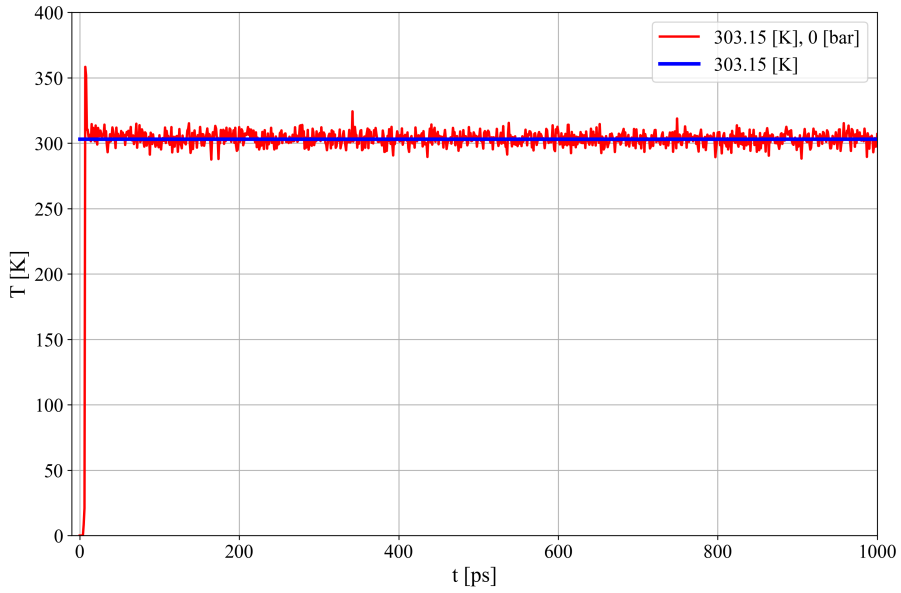

Figure 5.2: Example of temperature oscillations during the equilibration simulation of the SLGSA model at temperature 303.15 K and pressure of 0 bar

As seen in Fig. 5.2 after an initial sudden temperature jump from 0 to 360 K the temper-

ature falls down to 300 K and for the rest of equilibration simulation is oscillating around that value. After the equilibration of the structure, the uniaxial test in x, y-direction, and shear test were performed in order to obtain stress and strain values which will be used to determine E_{xx}, E_{yy} and G_{xy} values. In a uniaxial test in x and y-direction and shear test, in order to obtain stress values first the computation of stress per atom must be performed using *compute stress/atom* command in each iteration. This computation generates per-atom stress tensor for each atom which is symmetric with 6 components stored as 6 element vector with components stored in the following order: xx, yy, zz, xy, xz, and yz. The output value of this computation in the case of metal units are in bar $\cdot$ Å^3 units. In order to transform the value of stress per atom from vector to a scalar value the *reduce sum* command must be applied. This computation reduces one or more vector inputs into equivalent scalar values. The output value of this computation is in the same units as the quantities that are being reduced are in. Now that the stress/atom is a scalar value the stress/atom must be divided with the core volume. The core volume for of SLGSA and SLGSB model is calculated with an expression that is written in the following form:

$$V_C = \frac{V \cdot h}{L_z}, \tag{5.1}$$

where V represents the entire volume of the simulation box, h the thickness of the SLGSA or SLGSB model and the L_z the height of the simulation box. To obtain stress in x and y-direction in GPa units the following expression is used:

$$\sigma_i = \frac{C_{pi} \cdot 0.001}{V_C}, \qquad i = xx, yy, xy \tag{5.2}$$

where C_{pi} represents the reduced sum of the component stress tensor in a specific direction and 0.001 coefficient is used to convert pressure from bar units into GPa units.
One of the key components in the uniaxial and shear test is the *fix deform* command. This command changes the volume or shape of the simulation box during the MD simulation run. In a uniaxial test, the simulation box in which the SLGSA or SLGSB model is located is orthogonal, meaning that this box has 3 adjustable parameters (displacements in x, y, and z direction). In investigations of mechanical parameters of SLGSA and SLGSB only, x and y parameters where used. For the shear test of SLGSA and SLGSB model after equilibration, the simulation box was changed from orthogonal to triclinic (non-orthogonal) using *change_ box all triclinic* command. This type of simulation box have 6 adjustable parameters (x,y,z,xy,xz,yz). In the shear test of the SLGSA and SLGSB model, the xy component was utilized. Any of these adjustable parameters or all of them can be adjusted independently and simultaneously using this command.
In order to perform uniaxial and shear tests of SLGSA and SLGSB model using *fix deform*

command the *erate* parameter must be defined. This parameter changes the dimensions of the simulation box at a constant engineering strain rate. The units of the engineering strain rate are in 1/time, so in metal units, this parameter is equal to 1/ps. In a uniaxial test, the tensile strain is unitless and is defined, as the $\Delta L/L_0$, where L_0 is the original box length in x or y-direction and the ΔL is the change relative to the original simulation box length. The time dependency of box length L can be written, as:

$$L(t) = L_0 \cdot (1 + erate \cdot dt), \tag{5.3}$$

where dt represents elapsed time (ps).
In the shear test, the *erate* parameter changes the tilt factor at the constant engineering shear strain rate. The units are the same as in the uniaxial test-with metal units 1/ps. Shear strain is also unitless and is defined as the $\Delta S/L$, where length is the box length which is perpendicular to the shear direction, and the ΔS represents the displacement in the shear direction. In xy deformation of the simulation box the L parameter would be L_y or length in y-direction and ΔS would be changed in ΔL_x value. The tilt factor T as a function of time can be written as:

$$T(t) = T_0 + L_0 \cdot erate \cdot dt, \tag{5.4}$$

where T_0 represents initial tilt factor, L_0 is the original box length perpendicular to the shear direction (L_y) and dt is the elapsed time (ps), respectively. The strain value in uniaxial and shear test is calculated in each timestep with the expression that can be written in the following form:

$$\varepsilon_i = \varepsilon_t \cdot N_i, \qquad i = xx, yy, xy, \tag{5.5}$$

where ε_t is the strain rate per time step and N_i is iteration step. The strain rate per time step is calculated as:

$$\varepsilon_t = S_t \cdot t_s, \tag{5.6}$$

where S_t is the engineering strain rate, and t_s is the timestep. In all investigation of mechanical parameters the engineering strain rate is equal to 0.001 ps^{-1}.
The procedure for determining the mechanical parameters E_{xx}, E_{yy} and G_{xy} is based on linear regression analysis with R^2 metric. The elasticity and shear modulus can be defined as the relationship between stress and strain (shear stress and strain) of material in the linear elasticity regime. Due to some fluctuations in stress-strain relation, it is difficult to define the linear part (modulus of elasticity or shear modulus) based only on the calculated ratio between stress and strain. The R^2 compares two sets of solutions

which are the real data y and the data obtained by the model Y, in terms of variance. The real (MD) data represents the calculated ratio between stress and strain, while data Y is generated by the model. This metric gives the information about the amount of variance contained inside of data y, which was explained in the set Y. The value of R^2 can change between 0.0 and 1.0, where R^2 of 1.0 means that the variance between two sets does not exist, i.e. a perfect fit, while the value of 0.0 shows that there is not any relation contained in real data y that explains the model data. Generally, the R^2 is can be calculated using the following equation:

$$R^2 = 1 - \frac{S_{RESIDUAL}}{S_{TOTAL}} = 1 - \frac{\sum_{i=0}^{m}(y_i - Y_i)^2}{\sum_{i=0}^{m}\left(y_i - \frac{1}{m}\sum_{i=0}^{m} y_i\right)^2} \tag{5.7}$$

For linear regression analysis range from 2 in the first iteration up to maximum of 500 stress-strain points were used. In each iteration, the amount of stress-strain points was increased by one to train linear regression model, and the linear regression model was fitted with strain and stress data values in order to calculate R^2 metric value. Simultaneously, the model coefficient which is in these case modulus of elasticity or shear modulus value was also calculated. The higher values of R^2 metric indicated better approximation of stress-strain points with the line i.e. the linear elasticity regime. For each stress-strain curve, based on the obtained R^2 metric and model coefficient values (E_{xx}, E_{yy}, and G_{xy}) obtained from linear regression analysis the highest model coefficient was selected with the corresponding R^2 metric value. The average temperatures in all 10 simulations of uniaxial test in x-direction are ranging from 232.635 to 233.445 K. However, in each simulation the average E_{xx} value is 1022.0876 GPa with corresponding R^2 metric of 0.99414 is obtained. For all of the obtained E_{xx}, E_{yy} and G_{xy} values the R^2 metric value was always greater than 0.98.

To calculate the Poisson's ratio the required data are the initial lengths of SLGSA and SLGSB models in x and y-direction as well as at 20000, 40000 and 60000 iteration of uniaxial test simulation. The Poisson's ratio was calculated using the equation:

$$\nu_{xy} = -\frac{\frac{\Delta L_b}{L_b}}{\frac{\Delta L_a}{L_a}} \tag{5.8}$$

where ΔL_b is the difference in length between length in y-direction at 20000, 40000, and 60000 iteration and initial length in y-direction which is the length of SLGS model after equilibration simulation. The L_b is the initial length in y-direction after equilibration. The ΔL_a is the difference between the length in x-direction recorded at 20000, 40000 and 60000 iteration and initial length L_a as well as at coefficients of thermal expansion α_x and

α_y are obtained after the equilibration of SLGS structure using the formula:

$$\alpha_i = \frac{1}{L_i}\left(\frac{\Delta L_i}{\Delta T}\right) \qquad i = xx, yy, \tag{5.9}$$

where $\Delta L_i = L_{1i} - L_{0i}$ is the difference between the equilibration length in x or y-direction and the initial length, $\Delta T = T_1 - T_0$ is the temperature difference between equilibrated temperature and initial temperature. The L_i is the initial length of SLGS in x or y-direction. From Tab. 5.2, it can be calculated that the total number of different simulations is 54. For each equilibrated structure at a specific temperature and pressure, three different simulations of mechanical tests were conducted (uniaxial tests in x and y-direction and shear test). Since the difference in specified temperatures is very small (only 10 K) during the equilibration of structures and simulation of mechanical tests the temperature fluctuates around the specified value the simulation must be repeated multiple times in order to obtain consistent results by averaging. In these investigation, each simulation of mechanical tests is repeated 10 times so the total number of these simulations is 540. In further subsection the procedure for obtaining mechanical parameters and results will be presented.

5.3.1 Mechanical Parameters of SLGS at Different Temperatures Using REBO Potential

The SLGSA and SLGSB models were generated using the VMD software package [168]. The size of both SLGS structures is 10×5 nm and thickness of 0.34 nm. For these analyses, in order to obtain the mechanical parameters, the REBO potential was adjusted in terms of cutoff distance. In order to speed up MD computations, the interactions between two atoms which are separated by a distance greater than a predefined cutoff distance are ignored. The cutoff distance according to recommendation in [171] was changed from 1.7 Å to 2.0 Å. This modification also leads toward stress-strain relation which qualitatively agrees with the behavior observed in experimental [172] and ab-initio [95] investigations. The boundaries in x and y-direction are set to periodic, the pressure of 0 bar is applied to these boundaries and adjusted every 0.5 ps so that SLGS boundaries are at the edges of the simulation box. With the aforementioned adjustment of boundaries, the simulation of an infinite graphene sheet is performed. The boundary in z direction is fixed and set to 17 and -17 Å in order to simulate only one layer of graphene sheet.

5.3.1.1 Uniaxial test in x-direction

After the SLGS structure was relaxed/equilibrated at a specific temperature and pressure the following operations were carried out:

- the new dimensions in x, y, and z direction are saved under L_x, L_y, and L_z variable names, while the volume of the equilibrated structure was saved under the variable name Vol,
- the command *compute stress/atom* was used in order to compute per-atom stress tensor for each atom in the simulation box, and the reduced sum was computed using *compute reduced sum* in x and y-direction respectively in order to obtain scalar values of atom stress in pressure times volume units. These values were later transformed into stress in GPa units by dividing them with the core volume using Eq.(5.1) and Eq.(5.2), respectively,
- the uniaxial test of SLGSA and SLGSB model in x-direction was performed by applying the strain rate to the sample along x-direction at the rate of 0.001/ps. The simulation of the uniaxial test was carried out for 300 ps or 300000 iterations. Although the structure is equilibrated for a long time period (1000 ps) each uniaxial and shear test is carried out 10 times since the fluctuations around specific temperatures are small but noticeable. In other words, for each SLGS model, a total of 90 uniaxial test simulation in x-direction were carried out, 10 simulations for each temperature.
- For each stress-strain curve, the modulus of elasticity was determined using linear regression analysis, while Poisson's ratio was calculated using Eq.(5.8).

In Figs. 5.3 and 5.4 the stress-strain curves with maximum value of fracture stress at each temperature for SLGSA and SLGSB model are shown.

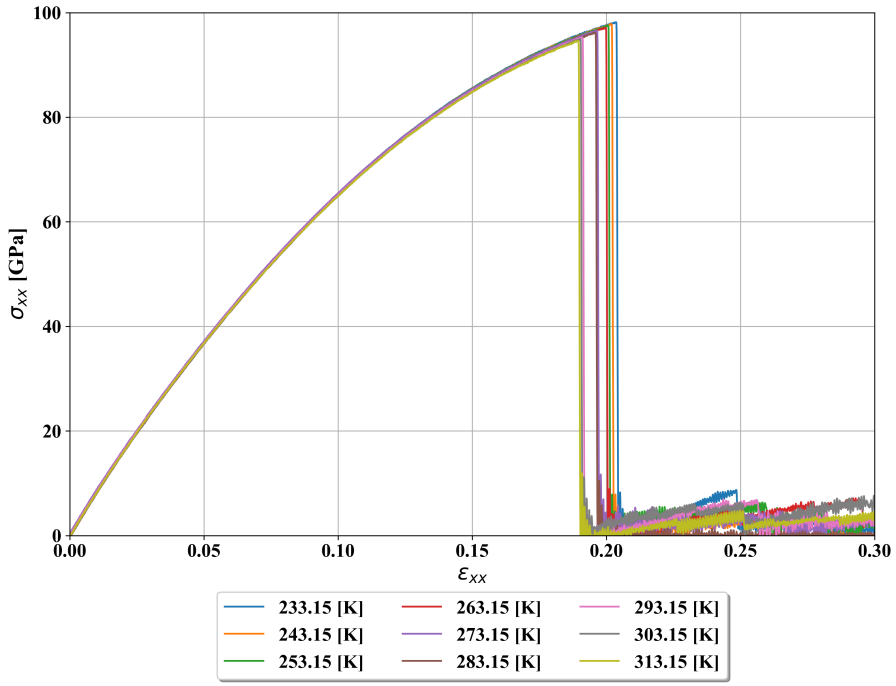

Figure 5.3: The stress-strain curves of SLGSA model subjected to uniaxial test in x-direction at different temperatures.

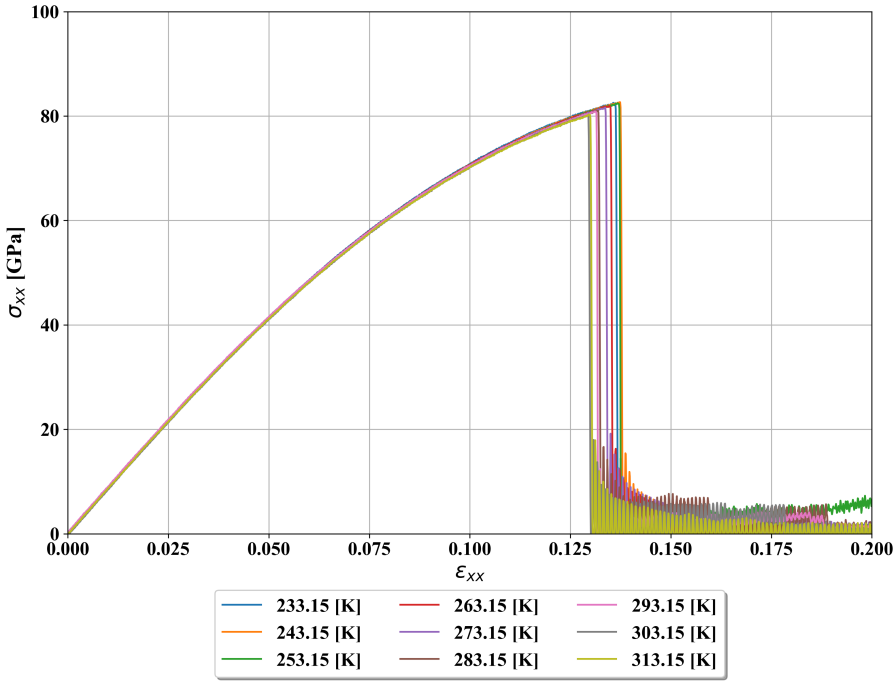

Figure 5.4: The stress-strain curves of SLGSB model subjected to uniaxial test in x-direction at different temperatures.

As seen in Figs. 5.3 and 5.4 the stress in x-direction is temperature depended. As the temperature increases, the maximum stress at which the SLGS fracture occurs becomes

lower. This phenomenon also occurs in the case of uniaxial test in y direction and shear test, respectively. It can be seen that the SLGSA model breaks when the strain reaches 0.2 while the fracture of the SLGSB model occurs around 0.125. The maximum stress of the SLGSA model at which fracture occurs is 98.15 GPa while in case of SLGSB model is 82.52 GPa. As mentioned in the introduction of this chapter, the SLGSA model has the zigzag edge in x-direction, and armchair edge in y-direction while the SLGSB model has the armchair edge in x-direction, and zigzag edge in y-direction. The values of fracture stress indicate that when the load is aligned with the zigzag edge structure can withstand much higher loads before the fracture occurs. After the fracture of SLGSA and SLGSB models occurs, there are some residual stresses which can be noticed in Figs. 5.3 and 5.4 as the strain increases. This can be attributed to the remaining connection between two separate pieces of SLGSA and SLGSB model. In Figs. 5.5 and 5.6 the minimum, average and maximum values of fracture stress for SLGSA and SLGSB model are shown.

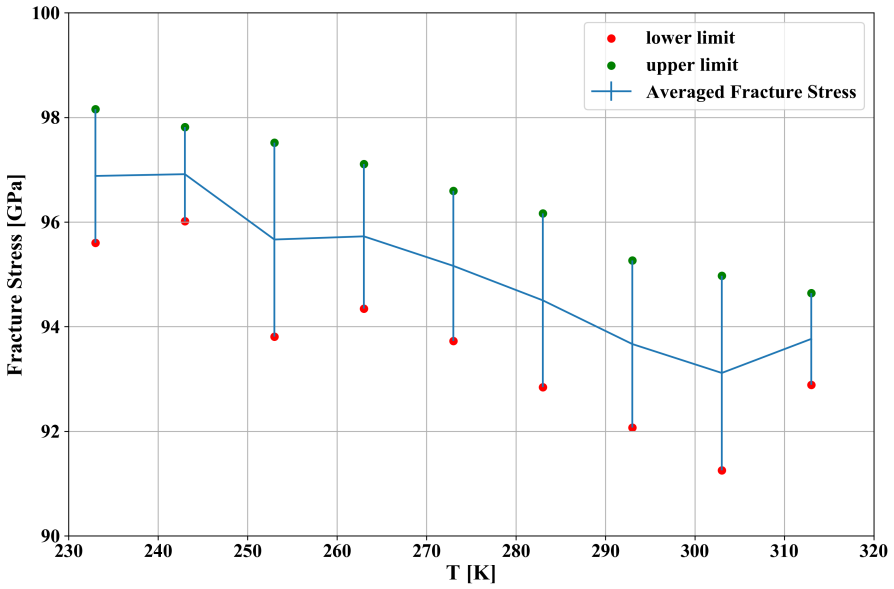

Figure 5.5: The average value of fracture stress with minimum and maximum values obtained at each temperature for SLGSA model.

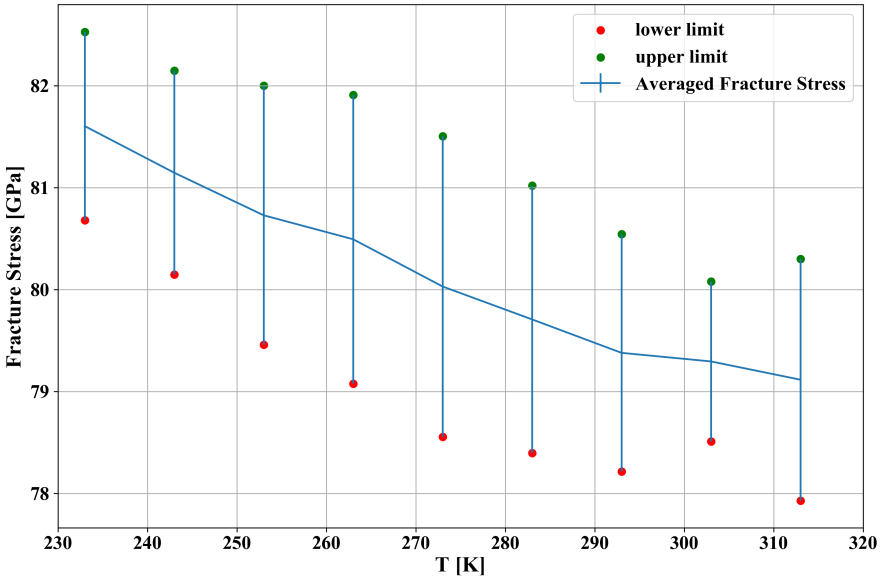

Figure 5.6: The average value of fracture stress with minimum and maximum values obtained at each temperature for SLGSB model.

As seen in Figs. 5.5 and 5.6, the variation of average fracture stress obtained using the uniaxial test in x-direction for SLGSA and SLGSB model is temperature-dependent. As the temperature increases, the values of average stress, as well as minimum and maximum values of fracture stress, decrease. This phenomenon also occurs in case of average fracture stress for uniaxial test in y direction as well as shear test. From figures it can be noticed that approximately linear trend of fracture stress versus temperature is obtained. In the case of the SLGSA model, the values of fracture stress, the difference between the minimum and maximum values are in the range of 1 GPa. However, in the case of the SLGSB model, this difference is higher and in the range of 1.5 GPa. When those two figures, are compared it can be seen that the SLGSA model in uniaxial test in x-direction can sustain much higher stress before fracture. The higher fracture stress values in the SLGSA model can be attributed to the fact that the uniaxial test in x-direction, is performed in the same direction as the zigzag edge. This edge can sustain higher loads and has higher stiffness than the armchair edge. The graphical representation of SLGSA and SLGSB models subjected to a uniaxial test in x-direction with a temperature of 233.15 K and without atmospheric pressure at 0, 100, 150, and 200 ps, are shown in Figs. 5.7 and 5.8.

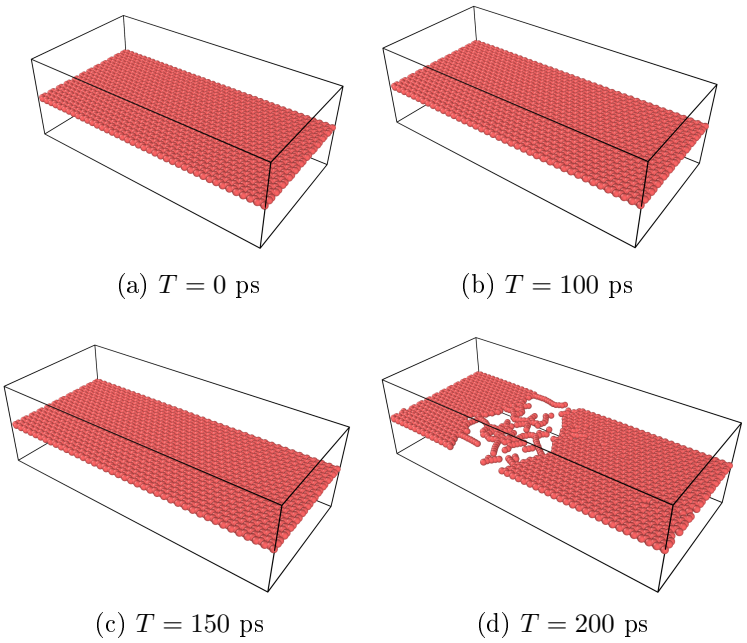

(a) $T = 0$ ps (b) $T = 100$ ps

(c) $T = 150$ ps (d) $T = 200$ ps

Figure 5.7: The graphical representation of the SLGSA model subjected to the uniaxial test in x-direction at different time steps at a temperature of 233.15 K.

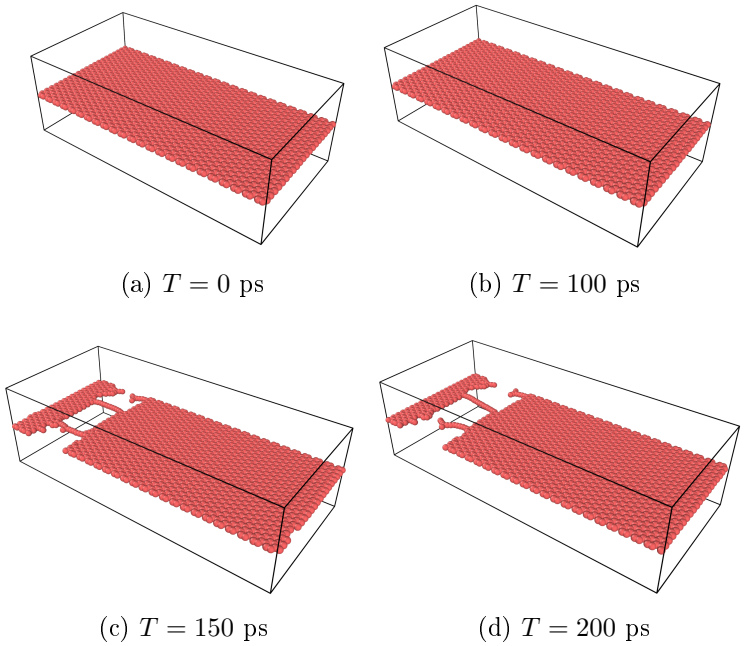

(a) $T = 0$ ps (b) $T = 100$ ps

(c) $T = 150$ ps (d) $T = 200$ ps

Figure 5.8: The graphical representation of the SLGSB model subjected to the uniaxial test in x-direction at different time steps at a temperature of 233.15 K

From Figs. 5.7 and 5.8 it can be noticed that SLGSB model fractures much earlier in simulation than SLGSA model. This is another indicator that gives additional information

that the SLGSA model (zigzag edge) can sustain much higher load in uniaxial test in x-direction i.e. in the zigzag edge. From Figs. 5.7 and 5.8 it can also be seen that after the SLGS structure is fractured there is still some connection between two pieces of SLGS structure and this is the reason why there are some stresses noticeable in Figs. 5.3 and 5.4 after the fracture occurred.

5.3.1.2 Uniaxial test in y-direction

The procedure for performing the uniaxial test of SLGS models in y-direction is the same as in the previous case with the exception of strain rate applied in y-direction. The total of 180 stress-strain curves (90 per each SLGS structure) was obtained for SLGSA and SLGSB model at a specific temperature range without atmospheric pressure using REBO potential. In Figs. 5.9 and 5.10, the stress-strain curves of SLGSA and SLGSB model at each temperature are shown, based on maximum values of fracture stress.

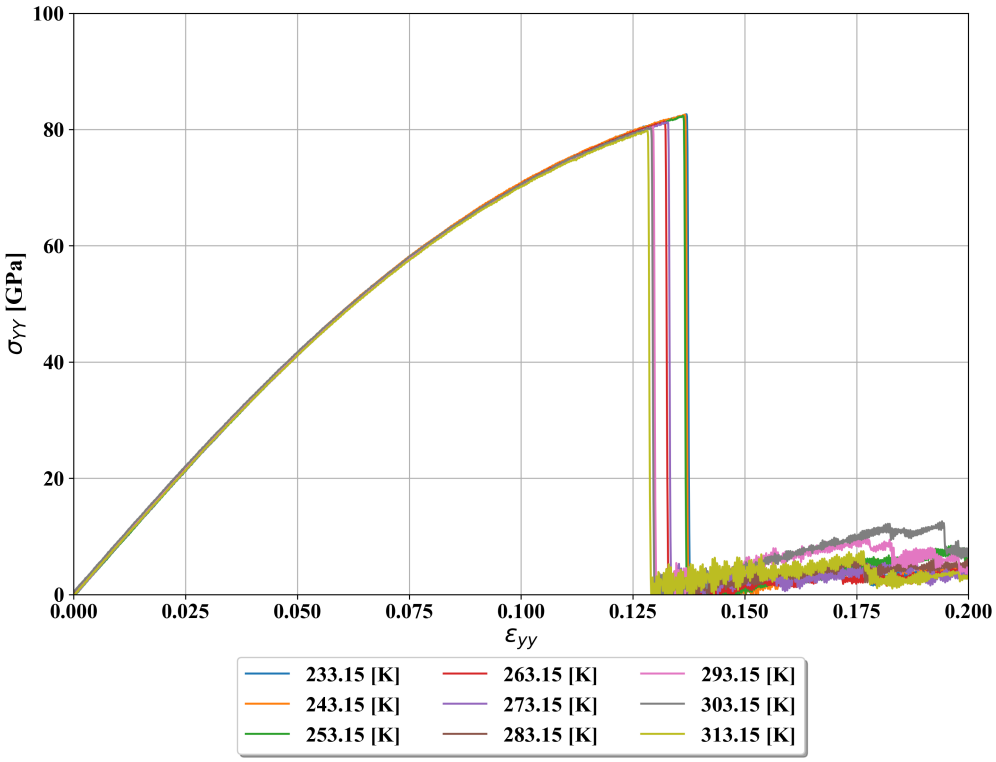

Figure 5.9: The stress-strain curves of SLGSA model subjected to uniaxial test in y-direction at different temperatures.

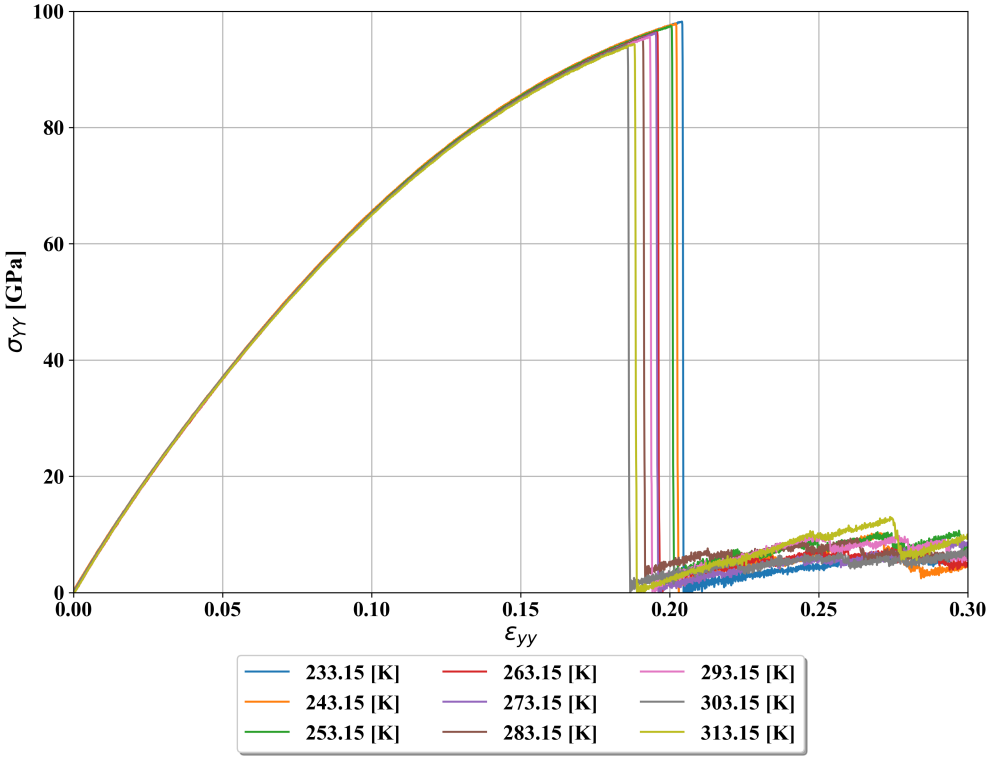

Figure 5.10: The stress-strain curves of SLGSB model subjected to uniaxial test in y-direction at different temperatures.

As seen from Figs. 5.9, and 5.10, the maximum stress value for the SLGSA model is 82.62 GPa, and for SLGSB model is 98.21 GPa. When two stress-strain diagrams, are compared it can also be noticed that the SLGSA model can sustain slightly less stress than the SLGSB model. In the case of the SLGSA model subjected to a uniaxial test in y-direction the armchair edge is in y-direction while in the case of the SLGSB model subjected to the uniaxial test in y-direction the zigzag edge is in y-direction. The fracture of the SLGSA model occurs when strain is in a range from 0.125 up to 0.14 while fracture in the case of the SLGSB model occurs when strain is in a range from 0.19 up to 0.21. These values indicate that SLGSB model can sustain higher loads in y-direction than SLGSA model. The average values of fracture stress with minimum and maximum values obtained in the uniaxial test in y-direction for different temperatures of SLGSA and SLGSB model are shown in Figs. 5.11 and 5.12.

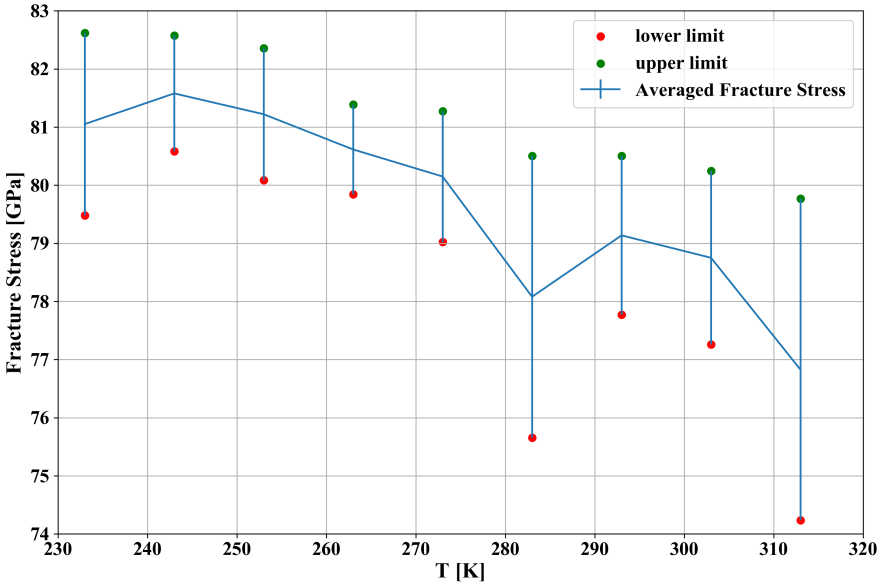

Figure 5.11: The variation of average fracture stress with minimum and maximum values versus temperature obtained with uniaxial test in y-direction for SLGSA model.

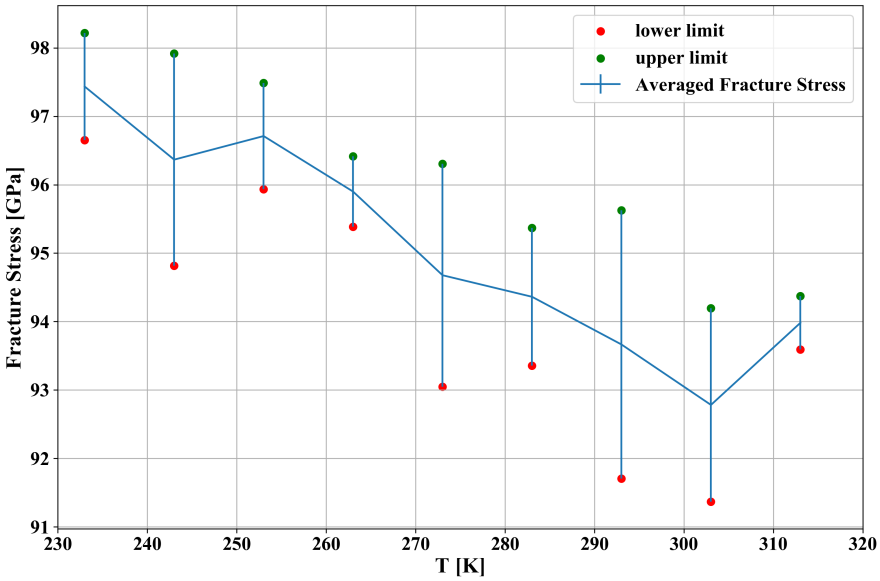

Figure 5.12: The variation of average fracture stress with minimum and maximum values versus temperature obtained with uniaxial test in y-direction for SLGSB model.

The difference of minimum and maximum values in SLGSA case shown in Fig. 5.11 at most temperature is 1.5 GPa with exceptions for temperatures of 283.15 and 313.13 K, where the difference between these two values is in range of 4.5 GPa. The difference between the minimum and maximum values in the SLGSB model shown in Fig. 5.12, at specific temperatures is in range from 1 to 3 GPa. However, at a temperature of 293.15 K, the difference between the minimum and maximum values of fracture stress is almost

4 GPa. When compared the values of fracture stress in the SLGSB model are higher than in the case of the SLGSA model. The reason for higher values in the SLGSB model can be attributed to the fact that the uniaxial test in y-direction is in direction of zigzag edge, and as mentioned earlier, this edge can withstand higher loads before breaking occurs. The graphical representation of SLGSA and SLGSB models subjected to uniaxial test in y-direction with temperature of 233.15 K and 0 bar at 0, 100, 150 and 200 ps are shown in Figs. 5.13 and 5.14.

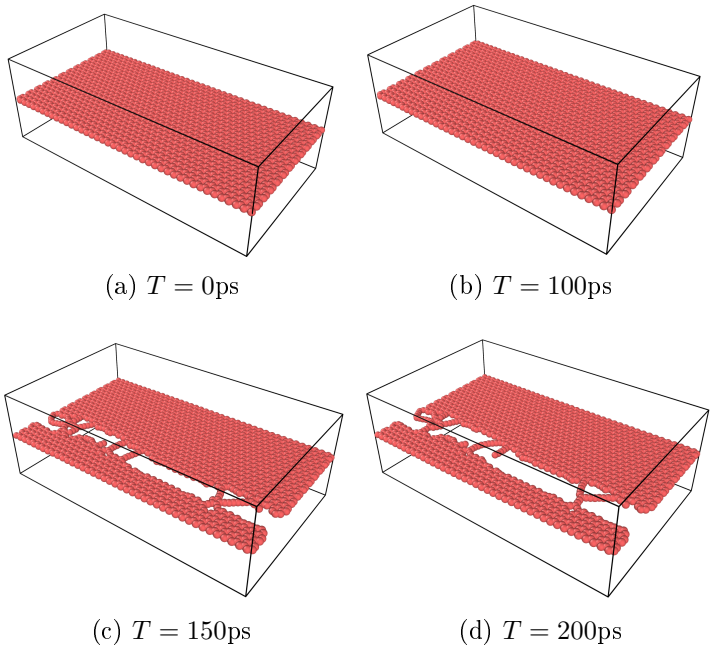

(a) $T = 0$ps (b) $T = 100$ps

(c) $T = 150$ps (d) $T = 200$ps

Figure 5.13: The graphical representation of the SLGSA model subjected to the uniaxial test in y-direction at different time steps for the temperature of 233.15 K and pressure of 0 bar.

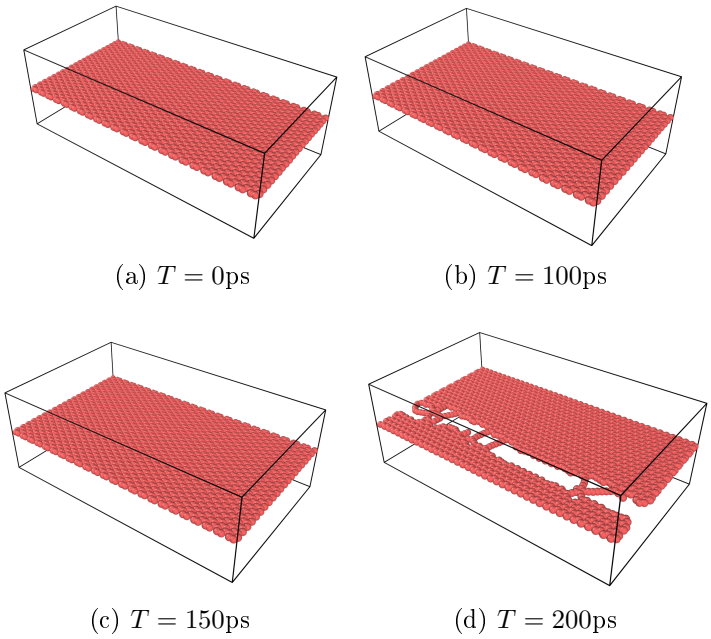

(a) $T = 0$ps (b) $T = 100$ps

(c) $T = 150$ps (d) $T = 200$ps

Figure 5.14: The graphical representation of the SLGSB model subjected to the uniaxial test in y-direction at different time steps for the temperature of 233.15 K and pressure of 0 bar

As seen from Figs. 5.13 and 5.14 the SLGSA model breaks much faster than SLGSB model. The fracture in the SLGSA model occurs before 150 ps after simulation started, while fracture in the SLGSB model occurs when simulation reaches 200 ps. It can be concluded that the SLGSB model subjected to a uniaxial test in y-direction can sustain a much higher load than the SLGSA model.

5.3.1.3 Shear test

For a shear test, after the equilibration of SLGSA and SLGSB models were done at a specific temperature and pressure, the simulation box is changed from orthogonal to the triclinic box using *change_box* command. The strain rate is applied xy plane, and the simulation was carried out for a maximum of 300 ps or 300000 iterations using *fix deform* command. Since there are 9 different temperatures in a range from 233.15 up to 313.15 K and due to temperature fluctuation the shear test at each temperature was repeated 10 times. In Figs. 5.15 and 5.16 the 9 stress-strain curves are shown for each model based on maximum value of fracture stress, are shown.

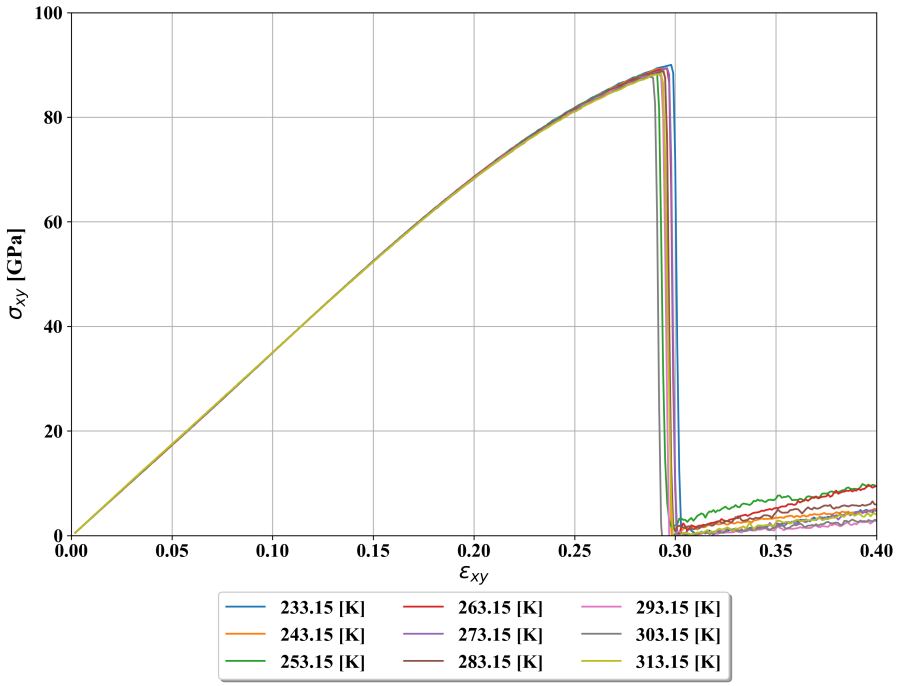

Figure 5.15: The stress-strain curve of SLGSA model subjected to the shear test at different temperatures.

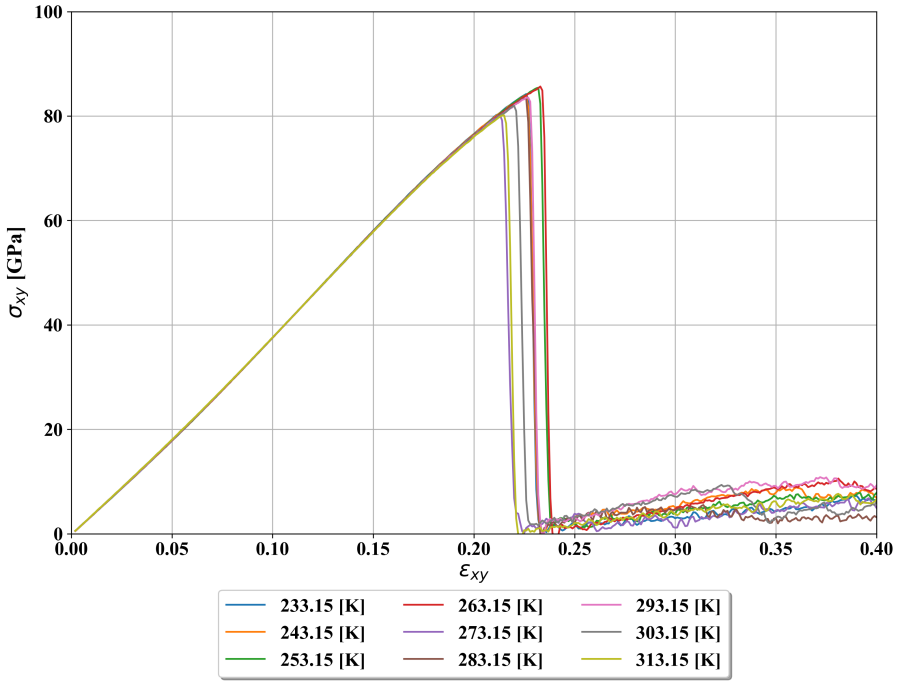

Figure 5.16: The stress-strain curve of SLGSB model subjected to shear test at different temperatures.

When stress-strain curves of SLGSA and SLGSB models shown in Figs. 5.15, and 5.16, are compared it can be seen that the SLGSA model can withstand a much higher load than

the SLGSB model. This is because the zigzag edge in the SLGSA model is longer than the armchair edge, and as seen from the previous investigation all analyses in zigzag edge direction generated higher stress values. The maximum shear stress that the SLGSA model can withstand is 90.02 GPa, while the maximum shear stress that the SLGSB model can withstand is 85.65 GPa. The variation average fracture stress with minimum and maximum values versus temperature obtained in shear test simulations for SLGSA and SLGSB model are shown in Figs. 5.17 and 5.18.

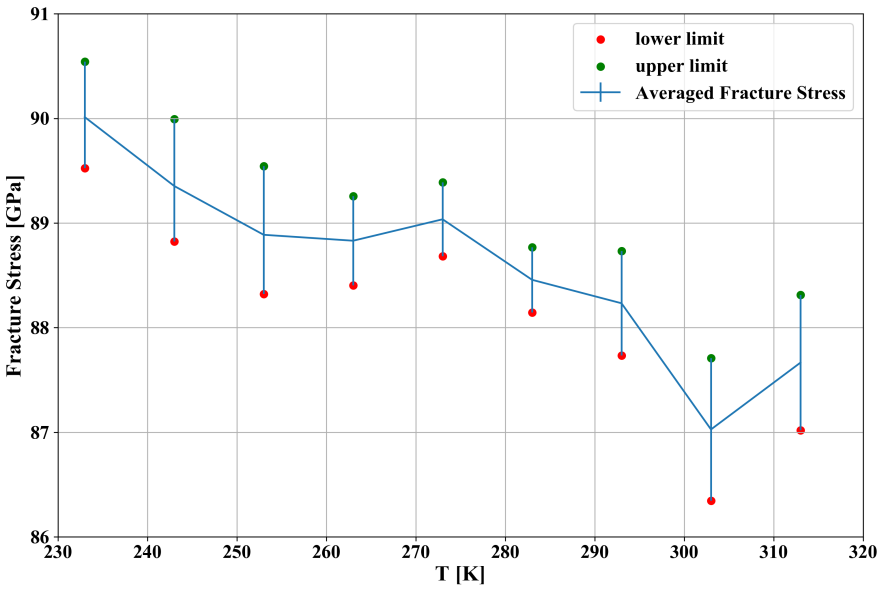

Figure 5.17: The variation of fracture stress with minimum and maximum values at different temperatures obtained with shear test simulations for SLGSA model.

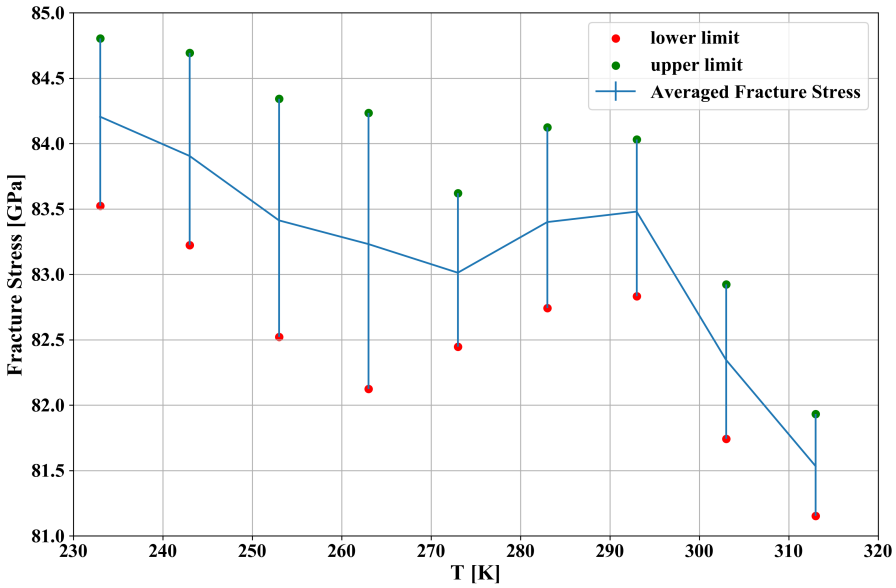

Figure 5.18: The variation of fracture stress with minimum and maximum values at different temperatures obtained with shear test simulations of SLGSB model.

In the case of the SLGSA model shown in Fig. 5.17, the difference in minimum and maximum values of fracture stress is in a range from 1 to 2 GPa while in the case of SLGSB model the difference is higher and in a range from 1.5 up to 2.5 GPa. Higher values of fracture stress, are achieved in the case of the SLGSA model due to the longer zigzag edge which can withstand higher stress values before a fracture occurs. In Figs. 5.19 and 5.20 the SLGSA and SLGSB models are shown subjected to shear test with temperature of 233.15 K and pressure of 0 bar at simulation time 0, 10, 20 and 30 ps.

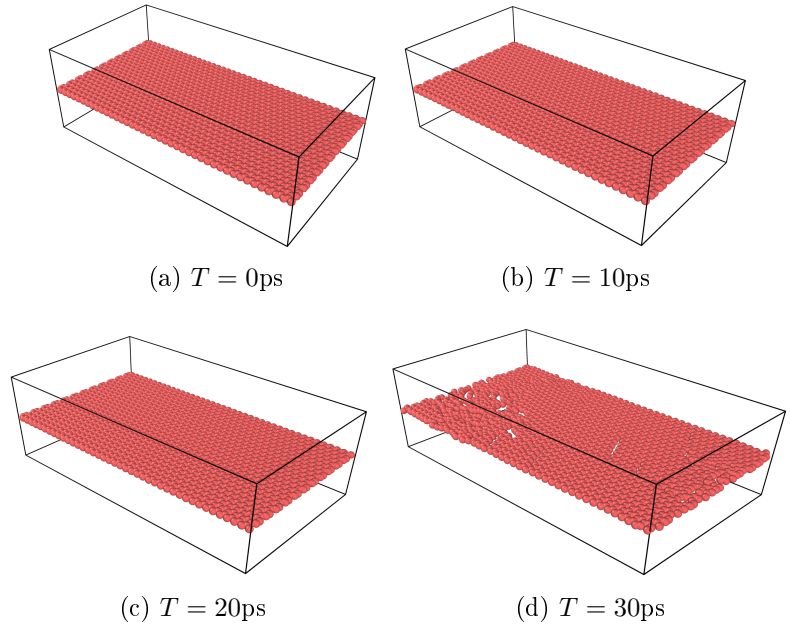

(a) $T = 0$ps (b) $T = 10$ps

(c) $T = 20$ps (d) $T = 30$ps

Figure 5.19: The graphical representation of SLGSA model subjected to shear test at different time steps at temperature of 233.15 K.

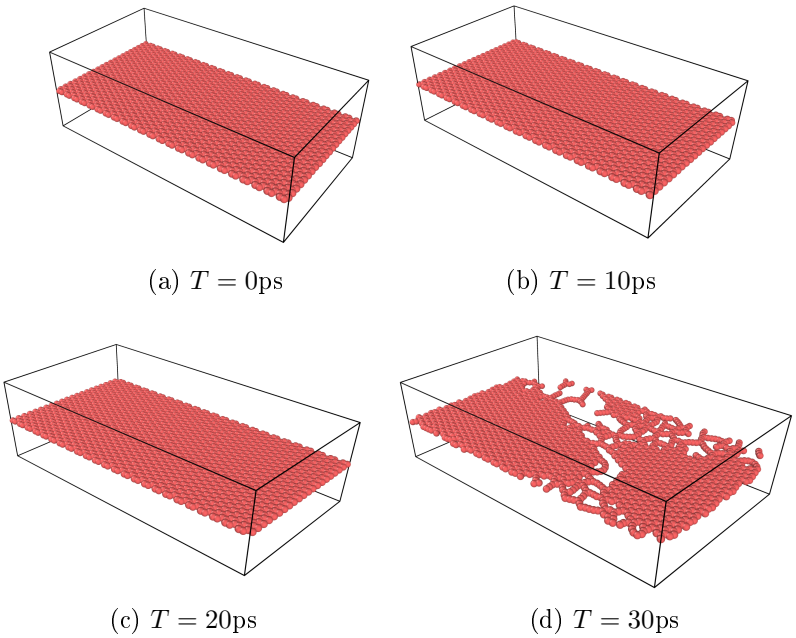

(a) $T = 0$ps (b) $T = 10$ps

(c) $T = 20$ps (d) $T = 30$ps

Figure 5.20: The graphical representation of SLGSB model subjected to shear test at different time steps at temperature of 233.15 K.

As seen from Figs. 5.19 and 5.20 that in SLGSB model fracture occurs much earlier than SLGSA model. This means that the SLGSB model can withstand less load than the SLGSA model. In Figs. 5.15 and 5.16, it can be seen that after the fracture of both models

occurs there are some stresses that occur with further application of shear strain which can be attributed to not fully fractured structures. The mechanical and thermodynamic properties obtained during the equilibration and later uniaxial tests in x and y-direction and shear test for both models are shown in Tabs. 5.3 and 5.4.

Table 5.3: SLGSA mechanical and thermodynamic parameters obtained using REBO potential without external pressure exerted on the system

Temperature [K]	E_{xx} [TPa]	E_{yy} [TPa]	G_{xy} [TPa]	ν_{xy}	α_x [K$^-$1]	α_y [K$^-$1]
233.15	1.0609	0.9230	0.3611	0.2541	-2.70085E-07	-2.07823E-05
243.15	1.0036	0.9065	0.3524	0.2322	-1.48749E-06	-2.32565E-05
253.15	1.0399	0.8721	0.3890	0.2622	-4.28776E-06	-1.94226E-05
263.15	0.9470	1.0359	0.3705	0.2649	-7.02156E-06	-1.89359E-05
273.15	0.9616	0.8855	0.3562	0.2715	-1.80875E-06	-1.62672E-05
283.15	0.8514	0.8967	0.3551	0.2605	-2.31484E-07	-1.4612E-05
293.15	1.0201	0.9640	0.3554	0.2664	-4.98748E-06	-1.48856E-05
303.15	0.9209	0.9724	0.3987	0.2695	-4.83014E-06	-1.57822E-05
313.15	0.9093	0.8978	0.3783	0.2522	-5.35251E-06	-1.39984E-05

Table 5.4: SLGSB mechanical and thermodynamic parameters obtained using REBO potential without external pressure exerted on the system

Temperature [K]	E_{xx} [TPa]	E_{yy} [TPa]	G_{xy} [TPa]	ν_{xy}	α_x [K$^-$1]	α_y [K$^-$1]
233.15	1.0609	0.9552	0.3947	0.1470	-1.5566E-07	-3.6629E-05
243.15	1.0288	0.9965	0.3941	0.1415	-4.7105E-07	-3.6565E-05
253.15	0.9914	0.8727	0.3939	0.1862	-2.8711E-07	-2.9439E-05
263.15	0.9541	0.8559	0.3933	0.1638	-1.2831E-06	-2.7850E-05
273.15	0.9884	0.8906	0.3933	0.1447	-2.3770E-06	-3.2624E-05
283.15	0.9240	1.0329	0.3925	0.1485	-1.2900E-06	-2.8285E-05
293.15	0.9494	0.9445	0.3922	0.1291	-1.3399E-06	-2.8461E-05
303.15	0.8966	1.0607	0.3917	0.1643	-3.4789E-07	-2.3913E-05
313.15	0.9043	0.8953	0.3917	0.1770	-1.3468E-06	-2.1472E-05

The E_{xx} and E_{yy} values shown in Tabs. 5.3 and 5.4 for SLGSA and SLGSB model are around 1.0 TPa which is consistent with the values obtained in experimental [9] and theoretical [94, 95] investigations. It can also be noticed that as the temperature rises, the E_{xx} and E_{yy} values drop down to 0.9 TPa. The shear modulus in both cases

is near 0.4 TPa, which is consistent with values reported in [96, 102, 104, 106, 107]. The Poisson's ratio values are little bit higher in SLGSA model than in SLGSB model, however the values are consistent with values obtained in [95, 94, 96, 101, 121, 98]. The α_{xx} and α_{yy} shown in Tabs. 5.3 and 5.4 are calculated using Eq.(5.9) and the values are negative which is consistent with values reported [173]. In this paper, the authors have utilized AIREBO and TERSOFF potential in the investigation of the thermal expansion coefficient. The result of their investigation showed that for temperatures below 600 K, the values of thermal expansion coefficient are negative when AIREBO potential is utilized. The AIREBO potential is an upgrade of REBO potential, so the obtained values of the thermal expansion coefficient are also negative.

5.4 Vibrations of SLGS

In this section, the investigation of natural frequencies of SLGSA and SLGSB models with different boundary conditions and three different temperatures is described. The influence of the pressure is omitted from these analyses due to very high-pressure fluctuations during the equilibration and vibration simulations which are in the range from -2 up to 2 bar. So instead of the NPT ensemble, the NVT ensemble was utilized. The natural frequencies of SLGSA and SLGSB models will be excited using the velocity excitation method. The REBO interatomic potential was used in these analyses as in the case of mechanical and thermodynamic properties investigation. However, the natural frequencies of these models will be investigated only at 233.15, 273.15, and 313.15 K due to high-temperature fluctuations during the vibration simulations which are in the range $\pm$10 K around previously mentioned temperatures. The procedure of performing influence of various system parameters on natural vibrations of SLGSA and SLGSB models consists of:

- influence of SLGSA and SLGSB structure size on natural vibrations at a constant temperature,
- influence of temperature variation on natural vibrations of SLGSA and SLGSB models,
- influence of attached gas/vapor molecules on natural frequencies of SLGSA and SLGSB models at different temperatures and pressures.

All these analyses will be conducted considering only clamped boundary conditions (CCCC) which means that all sides are completely clamped. To simulate this boundary condition, groups of atoms near the edges of the graphene sheet are defined. Boundary conditions

are assigned to these groups after system minimization is completed. In particular, the sum of forces acting on each atom in the group is set to zero, thus fixing its position. The procedure for defining the boundary conditions is adapted from literature [130]. The graphical representation of CCCC boundary conditions is shown in Fig. 5.21.

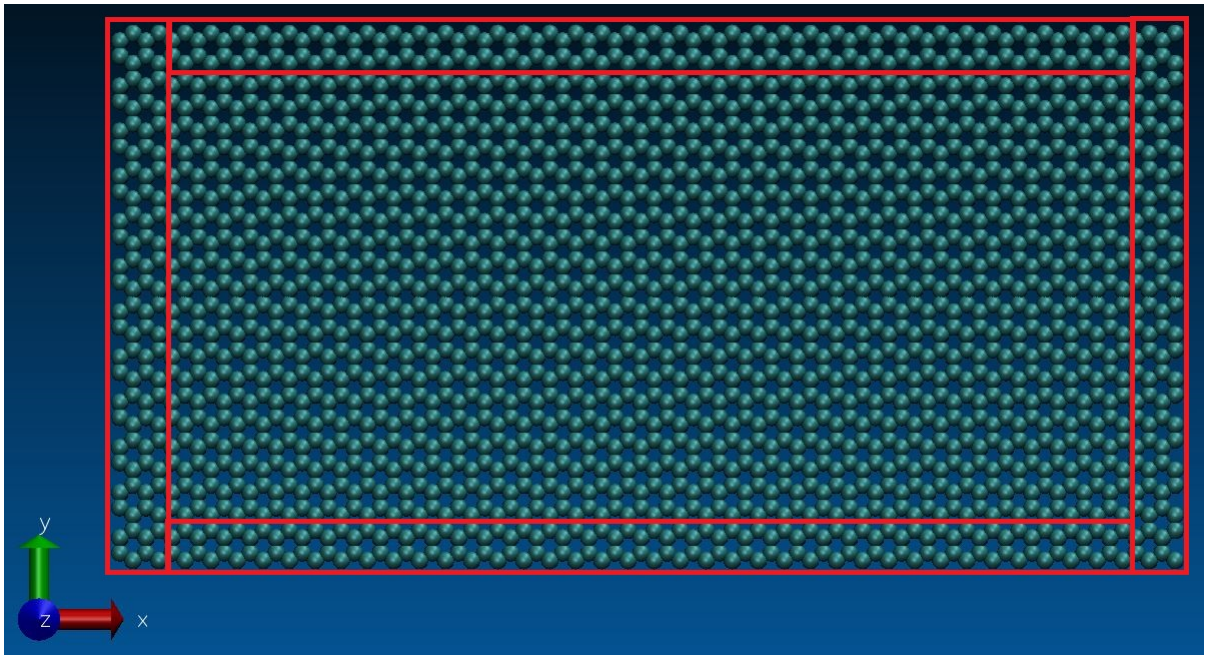

Figure 5.21: The graphical representation of SLGS CCCC boundary conditions

To simulate the clamped boundary condition the four rows of atoms are selected and force exerted on these atom group are set to zero. The group of atoms that are fixed during vibration simulations with clamped boundary condition (CCCC) are indicated with red rectangles in Fig. 5.21. All the regions that must be defined in LAMMPS input script after structure minimization but before equilibration simulation is performed, are shown in Fig. 5.22.

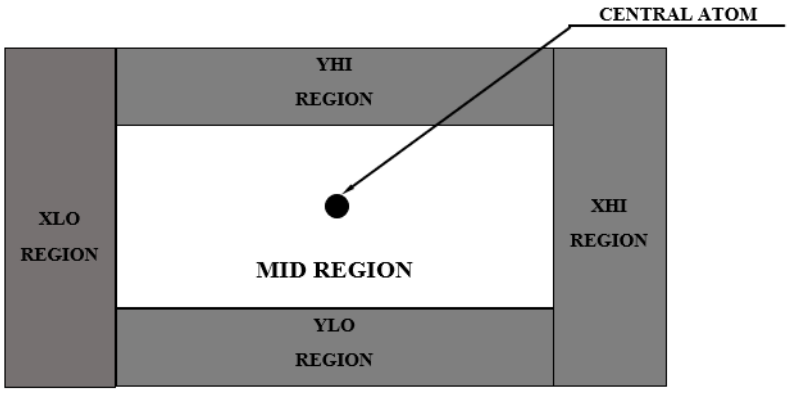

Figure 5.22: Schematic view of structure regions

As seen from Fig. 5.22 six regions must be defined to perform the equilibration and vibration simulations using velocity excitation method. These regions are named XLO, XHI, YLO, YHI, MID and $CENTRAL$ atom region. The XLO, XHI, YLO and YHI atom regions are regions of atoms where force on these atoms are set to zero in every direction. This means that atoms in these regions will be fixed during equilibration and vibration simulations. The MID and $CENTRAL$ atom regions will freely vibrate during the equilibration, and vibration simulations. Initial investigation of natural vibrations for SLGSA and SLGSB model with size of 10×5 nm showed that the natural frequency highly fluctuates so these models were not used in further MD simulations. Instead, the SLGSA and SLGSB model with sizes 20×10, 30×15 and 40×20 nm are considered but before performing equilibration and vibration simulation the number of atoms per region must be defined. In Tab. 5.5 the number of atoms for each region are shown.

Table 5.5: The number of atoms in different regions of SLGSA and SLGSB with CCCC boundary condition

Region name	SLGSA			SLGSB		
	20×10	30×15	40×20	20×10	30×15	40×20
XLO	192	288	384	164	248	328
XHI	192	288	384	164	248	328
YLO	312	476	636	368	552	744
YHI	312	476	636	368	552	744
MID	6864	16184	29256	6808	16008	29016
Total number of atoms	7872	17712	31296	7872	17608	31160

5.4.1 Velocity Excitation

To determine the natural frequency of the system the MID region must be excited. This region that is subjected to the free vibration which is shown in Fig. 5.22 will be excited using velocity excitation method. In this method the velocity distribution function is used to excite the MID region for 200 ps using NVE ensemble. The velocity distribution function for CCCC boundary condition can be written in the following form

$$v_{CCCC}(x,y) = v_0\Big(1-\cos\Big(\frac{2m\pi x}{L_a}\Big)\Big)\Big(1-\cos\Big(\frac{2n\pi y}{L_b}\Big)\Big), \tag{5.10}$$

where v_0, m, n, L_a, L_b represents the initial velocity, mode shape numbers, length of nanostructure in x and y-direction, respectively. As reported in [174] the initial velocity v_0 was

set to 1 Å/ps in all vibration simulations for SLGSA and SLGSB model. By setting the initial velocity to aforementioned value the corresponding amplitude was less than 1.5 Å which is too small to generate violent nonlinear vibrations. Before measuring the free vibrations of atoms the middle region of SLGS structure is excited using velocity distribution function in z direction. The implementation of velocity distribution function on SLGSA model with CCCC boundary conditions is shown in Fig. 5.23.

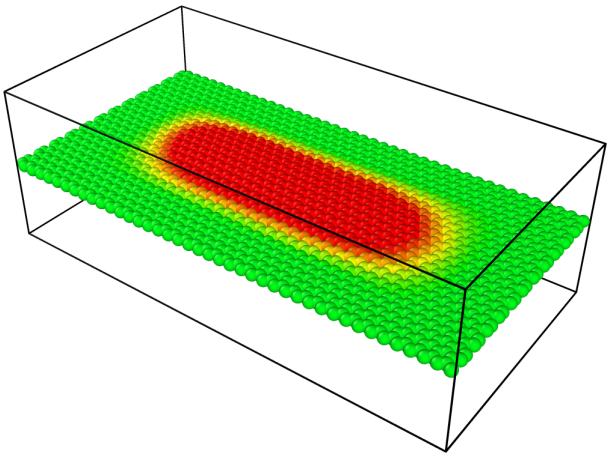

Figure 5.23: The SLGSA model with CCCC boundary condition after application of velocity excitation function, first mode shape ($m = 1, n = 1$)

As seen from Fig. 5.23 it can be noticed that the displaced region is indicated by the red color while the green region represents atoms without any displacement. This displacement of atoms represents the first mode shape that was generated using Eq.(5.10).

5.4.2 Influence of graphene sheet size on their natural frequencies

One of the hypotheses was to investigate the influence of size on the natural frequencies of the SLGS structure. Several research papers [175, 133, 158] reported the influence of the size of graphene sheets on their natural and resonant frequencies. In Tab. 5.6 the list of SLGS that will be used to investigate the influence of size in terms of width and length on their natural frequencies is shown.

Table 5.6: The structure sizes and temperatures in vibration simulation using velocity excitation method

Structure Type	Interatomic Potential	$L_a \times L_b$ [nm]	Temperature [K]
SLGSA	REBO	20×10	233.15
		30×15	273.15
		40×20	313.15
SLGSB	REBO	20×10	233.15
		30×15	273.15
		40×20	313.15

As seen from Tab. 5.6 there are two different nanostructure types and these are SLGSA and SLGSB. For each nanostructure type, three different models were generated in terms of size from 20×10 up to 40×20 so there is a total of 6 different models. Before investigating vibrations using the velocity excitation method each model must be equilibrated. The equilibration simulation consists of two different simulations. Before these simulations, the XLO, XHI, YLO, YHI, and MID regions are defined. First, the minimization simulation is performed to achieve a state of minimum energy. Then the boundary conditions are applied on previously defined regions by setting force in each direction to zero except for the MID region. The MID region was equilibrated with NVT ensemble using the Nose-Hoover thermostat with fixed walls of the simulation box. The equilibration using the aforementioned ensemble was performed for 100000 iterations or (100 ps).
The vibration simulation for each structure consists of two different simulations. The investigation of natural frequencies is performed using NVE ensemble since by definition the system that is excited to the specific natural frequency does not exchange the energy with the environment. In this simulation the MID region of SLGS structure was excited using velocity excitation function given in Eq.(5.10) for 200000 iterations (200 ps). After excitation simulation of MID structure the simulation of vibration using NVE ensemble for 1000000 iterations (1000 ps). In this final simulation, the average displacement and average velocity of atoms in the MID region were recorded in each iteration. After vibration simulation of each structure, the average displacement or average velocity of atoms was used to perform FFT analysis to calculate the natural frequency since both of them generate the same natural frequency value.
Each of the vibration simulations of each model at 233.15, 273.15, and 313.15 was repeated 10 times so the total number of simulations is 180. After all, simulations are done the FFT was used to obtain the natural frequency. Since for each model the simulation is repeated 10 times, there is a total of 10 natural frequencies obtained. These 10 nat-

ural frequency values were used to calculate the averaged frequency value and standard deviation value. For all averaged natural frequencies the standard deviation value did not exceed 0.8 GHz. In Figs. 5.24 and 5.25 the frequency variation versus SLGSA and SLGSB size with CCCC boundary condition is shown at different temperatures.

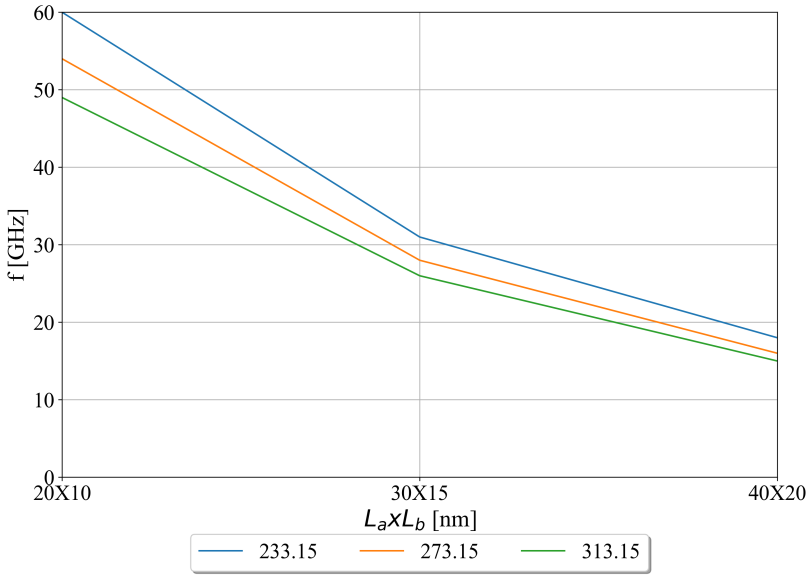

Figure 5.24: Frequency variation versus SLGSA size with CCCC boundary condition excited using velocity excitation method

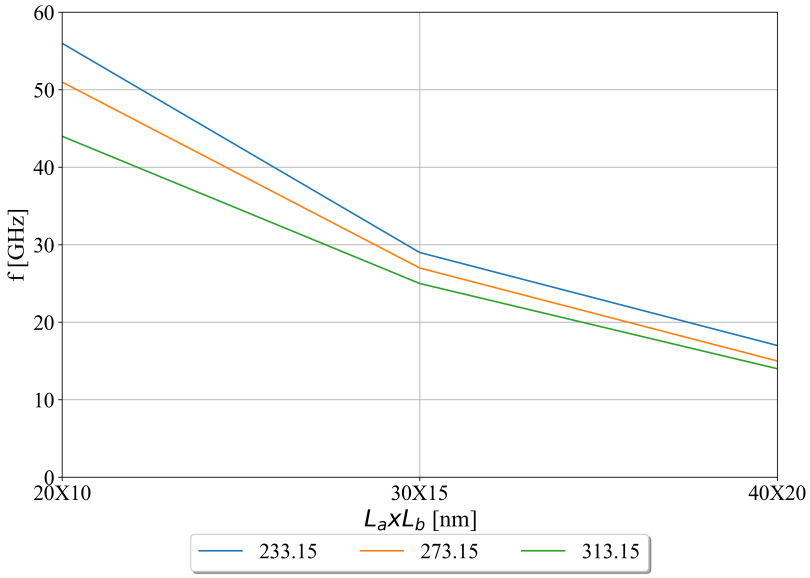

Figure 5.25: Frequency variation versus SLGSB size with CCCC boundary condition excited using velocity excitation method

As seen from Figs. 5.24 and 5.25, as the size of SLGSA and SLGSB model increases the natural frequency decreases. The most rapid drop in natural frequency for both model

types occurs when the size of both models increases from 20×10 to 30×15 nm. This decrease in natural frequency value is almost 50 %. As the SLGS sheet size increases from 30×15 up to 40×20 nm, the natural frequency value slowly decreases. It can also be noticed that the difference between natural frequencies of SLGSA and SLGSB models with size 20×10 nm obtained at different temperatures is much larger when compared to SLGS models with size 30×15 and 40×20 nm. From this observation, it can be concluded that the temperature has also some influence on natural frequency values but much smaller when compared to the influence of size on natural frequencies.

5.5 Determining Base Frequencies of Graphene Sheet

To calculate the absolute and relative frequency shift caused by gas/vapor molecules attached at SLGSA and SLGSB models surface the base natural frequencies must be obtained first. The term base natural frequency refers to the first natural frequency of the SLGSA and SLGSB models when the system vibrates freely without the presence of molecules attached to its surface. In these analyses, the REBO interatomic potential was used, and the temperature range from 233.15 K up to 313.15 K, and pressure of 0 bar. However, due to the small temperature difference in previous investigations in these analyses the temperature difference was set to 40 K so there are only three temperature levels.

The 10 equilibration and vibration simulations were performed for SLGSA and SLGSB model with dimensions 20×10 nm, and with CCCC boundary conditions at each temperature. So a total of 60 equilibrations and 60 vibration simulations were performed. The procedure of performing equilibration and vibration simulation is identical as in the previous case.

The average displacement and average velocity of MID region atoms in both models were calculated and recorded in each timestep and after the simulation was completed the FFT algorithm was used on recorded average displacement and/or velocity to obtain natural frequency. After all, simulations are completed average natural frequencies and standard deviation were calculated for each model at a specific temperature. For all averaged values of natural frequencies, the standard deviation did not exceed 0.8 GHz. The frequency versus temperature for SLGSA and SLGSB model with CCCC boundary condition is shown in Figs. 5.26.

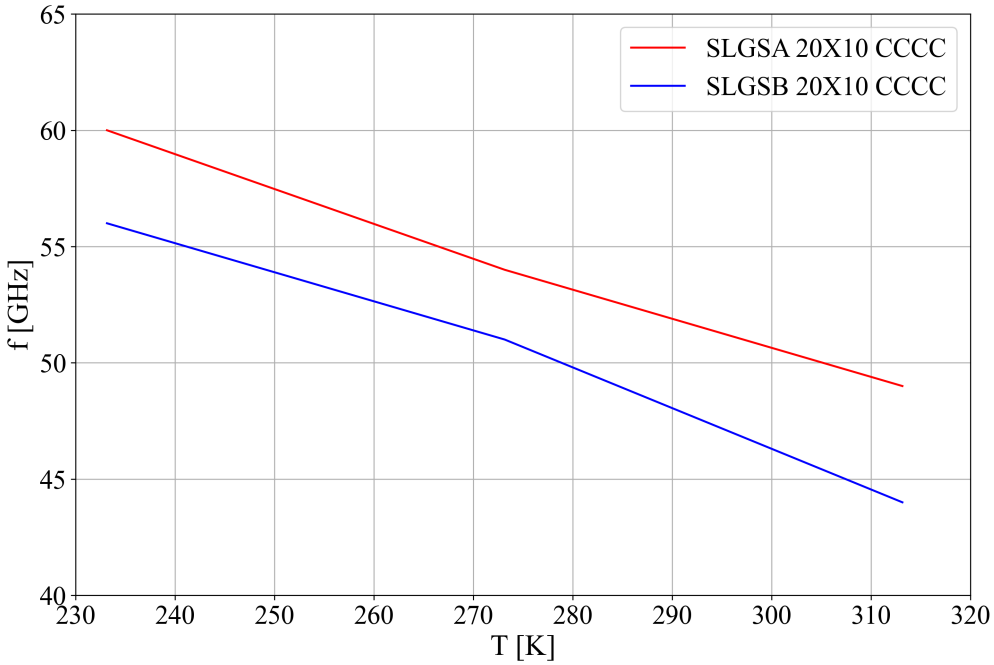

Figure 5.26: The frequency variation versus temperature of the SLGSA model with CCCC boundary condition.

As seen from Figs. 5.26, the natural frequencies of SLGSA and SLGSB model are temperature dependent. As the temperature rises the value of natural frequencies also decreases. When natural frequency values of the SLGSA and SLGSB model are compared it can be noticed that the natural frequency values of the SLGSA model are higher than those obtained with the SLGSB model.

5.6 Absolute Frequency Shift Caused by CWA

For absolute frequency shift first, the frequency of SLGSA and SLGSB model without attached gas/vapor molecule must be determined. Then the frequency of the SLGSA and SLGSB models with attached gas molecule is determined. The difference between those two frequencies represents the absolute frequency shift value. The absolute frequency shift value can be written in the following form

$$\Delta f = f - f_0, \tag{5.11}$$

where f_0 is the frequency of the SLGSA or SLGSB model without the attached gas molecule. The f is the frequency that is caused by the attached molecule at the center of SLGSA or SLGSB model.

In these analyses, the SLGSA and SLGSB model with a size of 20×10 nm were used

with the attached carbon atom at the center. All the simulations were performed at a temperature of 313.15 K. These central, attached carbon atoms are simplifications representing molecules, and the mass of that carbon atom was changed to the mass of the corresponding CWA molecule. In Tab. 2.5 the list of all CWA molecules used in these analyses with the corresponding mass in g/mol is given. Since the initial length between the modified carbon atom and graphene sheet in z direction was 1.5 Å, the modified carbon atom was classified as the second structure (label 2) while the graphene sheet as the first structure (label 1) and the REBO potential is activated to simulate the interaction between those two structures. In these analyses, there are a total of 3 different CWA molecules that were used in order to investigate if SLGS nanostructure is capable of detecting these molecules. But before performing natural vibration simulation using the velocity excitation method the SLGSA and SLGSB model containing these molecules must be equilibrated. The equilibration of each structure is conducted using the same procedure as in previous analyses. However, the only modification made is that the central carbon atom that represents the attached mass was excluded from the MID region and on this atom, the movement is restricted only in the z direction. The procedure of equilibration/vibration simulation of the SLGSA and SLGSB structure with an attached mass was repeated 10 times. After the simulations were performed the FFT algorithm was used on recorded averaged displacement of MID region in order to calculate the natural frequency. When all the natural frequencies from all simulations are obtained the averaged natural frequency was calculated for each model. It should be noted that the standard deviation of average values of natural frequencies was below 0.1 GHz, as in the previous analysis. In Figs. 5.27, the variation of average absolute frequency shift for SLGSA and SLGSB model with CCCC boundary condition considering 3 different gas/vapor molecules, are shown.

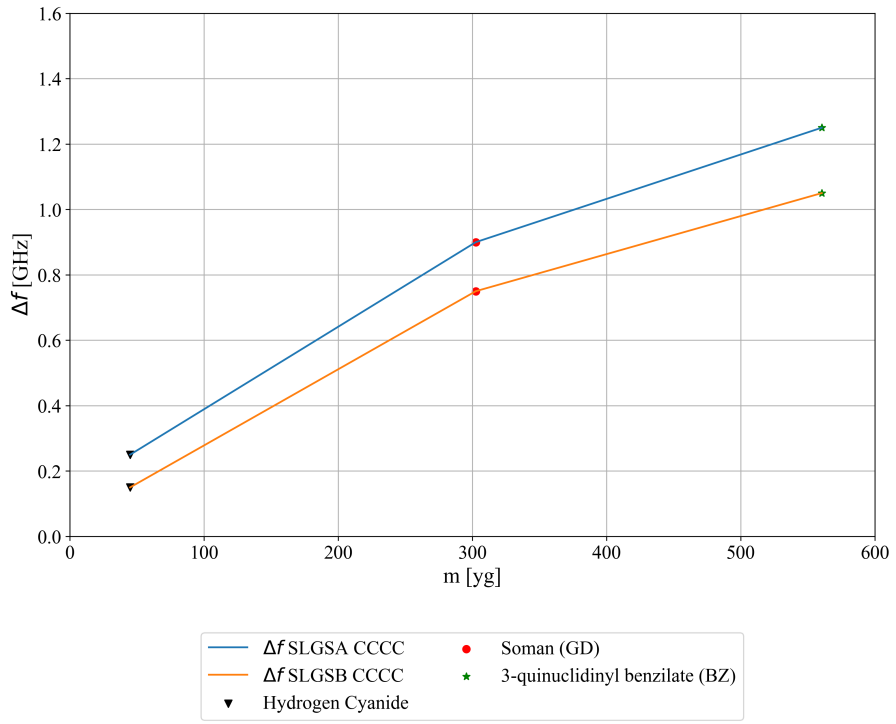

Figure 5.27: The change of average absolute frequency shift for SLGSA and SLGSB model with size (20×10 nm) CCCC boundary condition considering 3 different gas molecules.

As seen from Fig. 5.27 the average absolute frequency shift of SLGSA and SLGSB model has a similar trend. As the mass of the attached CWA molecule increases the value of average absolute frequency shift also increases. The smallest difference between average absolute frequency shift values can be noticed in the case when hydrogen cyanide molecule is attached at the surface center of SLGSA and SLGSB model respectively. The largest difference in the average absolute frequency shift values is noticed in the case where the 3-quinuclidinyl benzilate (BZ) molecule is attached at the surface of the SLGSA and SLGSB model. The highest increase in average absolute frequency shift value for both models can be noticed when instead of hydrogen cyanide molecule attached at the center of both models is soman molecule.

5.6.1 Relative frequency shift of SLGS at constant temperature caused by CWA molecule

The relative frequency shift value can be obtained with the formula:

$$f_{relative} = \frac{f - f_0}{f}, \tag{5.12}$$

where f_0 is the frequency of the SLGSA or SLGSB model without attached gas/vapor molecule and the f is the frequency that is caused by gas/vapor molecule attached at the surface of SLGSA or SLGSB model. The procedure for obtaining the natural frequencies caused by these gas/vapor molecules was described in the previous subsection. In Figs. 5.28, the variation of average relative frequency versus temperature of SLGSA and SLGSB model with CCCC boundary condition, considering 3 different gas/vapor molecules, are shown.

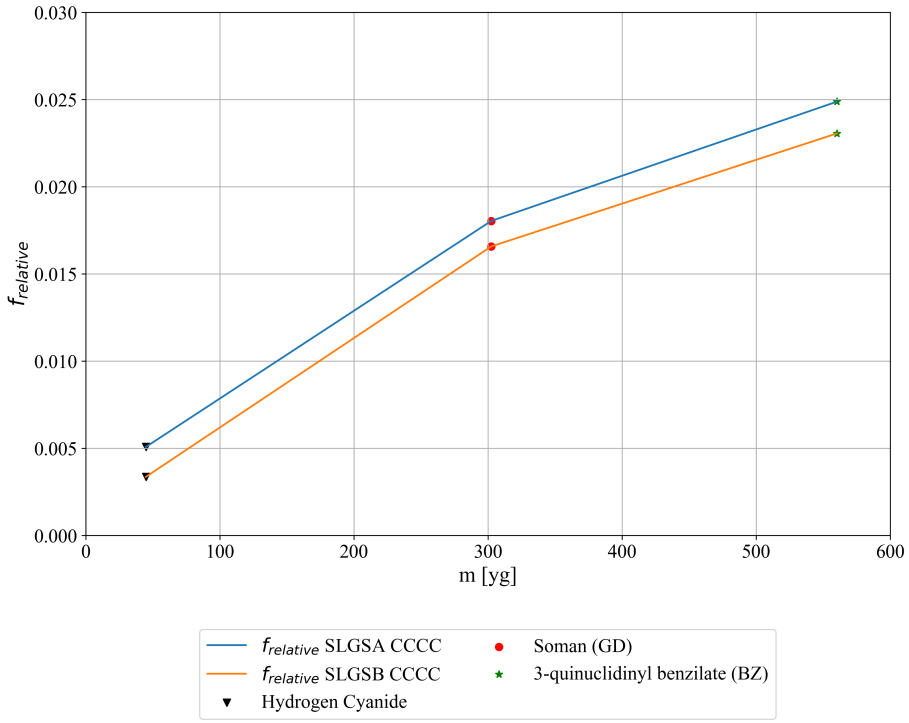

Figure 5.28: The variation of average relative frequency shift for SLGSA model with CCCC boundary conditions considering 3 different gas molecules.

As seen in Fig. 5.28 the trend in average relative frequency shift value is similar to average absolute frequency shift. As the mass value of the attached atom at the center of both models increases the value of the average relative frequency shift also increases. The difference in average relative frequency shift value between the two models is practically the same. The highest average relative frequency shift value for both models can be noticed in the case when the mass of the attached molecule is changed from hydrogen cyanide to soman.

6. Results Obtained Using Non-local Theory

In this chapter, the results obtained using non-local plate theory for SLGSA and SLGSB model are shown. The mechanical and thermodynamic parameters in the previous chapter are used for calculating the natural frequencies of SLGS plate models. In these analyses as in the case of MD simulation, only the CCCC boundary condition is considered. The following investigations were performed using non-local plate theory:

- the influence of non-local parameter variation on natural frequencies of SLGS with CCCC boundary condition,
- the influence of temperature and non-local parameter on natural frequencies of SLGS with CCCC boundary condition,
- the influence of temperature and pressure on natural frequencies of SLGS with CCCC boundary condition,
- the influence of SLGS size on its natural frequencies with CCCC boundary condition,
- the absolute and relative frequency shift method will be applied to determine the frequency shift caused by attached gas/vapor molecules at the center of SLGS plate models.

The investigation of the influence of non-local parameter, temperature, pressure, graphene sheet size on natural frequency using non-local theory was conducted with mechanical and thermodynamic parameters that were obtained using MD simulations and REBO interatomic potential.
It should be noted that the dimensions of the plates are slightly smaller than those considered in MD simulation, Tab. 6.1. In these simulations on each edge of the SLGSA and SLGSB model, the four rows were fixed during the simulation. So the real size of these models in terms of length and width is the size of the MID region that was freely oscillating during the vibration simulation. In Tab. 6.1 the actual lengths of the SLGSA and SLGSB models, are shown.

Table 6.1: The SLGSA and SLGSB sizes used in MD simulation and the actual sizes that will be used in non-local plate analysis.

	SLGSA $L_a \times L_b$ [nm]			SLGSB $L_a \times L_b$ [nm]		
Size in MD simulation	20×10	30×15	40×20	20×10	30×15	40×20
Actual Size	19.1×9.4	29.2×14.5	39.1×19.5	19.5×9.2	29.3×14.2	39.5×19.2

Unless otherwise specified, in the majority of natural frequency investigation using non-local plate theory the SLGSA and SLGSB model with plate dimensions of 19.1×9.4 and 19.5×9.2 nm, will be utilized.

6.1 Influence of Non-local Parameter on Natural Frequencies of Graphene Sheet

In these investigations, the influence of non-local parameter value on natural frequencies of SLGSA and SLGSB models with CCCC boundary condition were investigated. The external forces acting on the system and the temperature variation were neglected in these analyses. The frequency Eq.(3.41) for SLGS system with CCCC boundary conditions is reduced to:

$$f_{mnCCCC} = \frac{1}{2\pi}\sqrt{\frac{D_{11}\frac{3m^4\pi^4}{L_a^4} + 2(D_{12}+2D_{66})\frac{m^2n^2\pi^4}{L_a^2L_b^2} + D_{22}\frac{3n^4\pi^4}{L_b^4}}{\frac{3h\rho}{4}\left(\frac{3}{4} + (e_0a)^2\pi^2\left(\frac{m^2}{L_a^2}+\frac{n^2}{L_b^2}\right)\right)}}. \tag{6.1}$$

The materials characteristics and geometry of SLGS that will be used in these analyses are shown in Tabs. 5.3 and 5.4.

6.1.1 Influence of Non-local Parameter on Natural Frequencies of SLGS

The results of the influence investigation of the non-local parameter on natural frequencies of SLGSA and SLGSB model with CCCC boundary condition is shown. In these investigations, multiple mode shapes were considered. The mode shapes are defined with mode numbers m and n and they are in a range from 1 to 3. The influence of non-local

parameter on natural frequencies of SLGSA and SLGSB models with CCCC boundary condition are shown in Figs. 6.1 and 6.2.

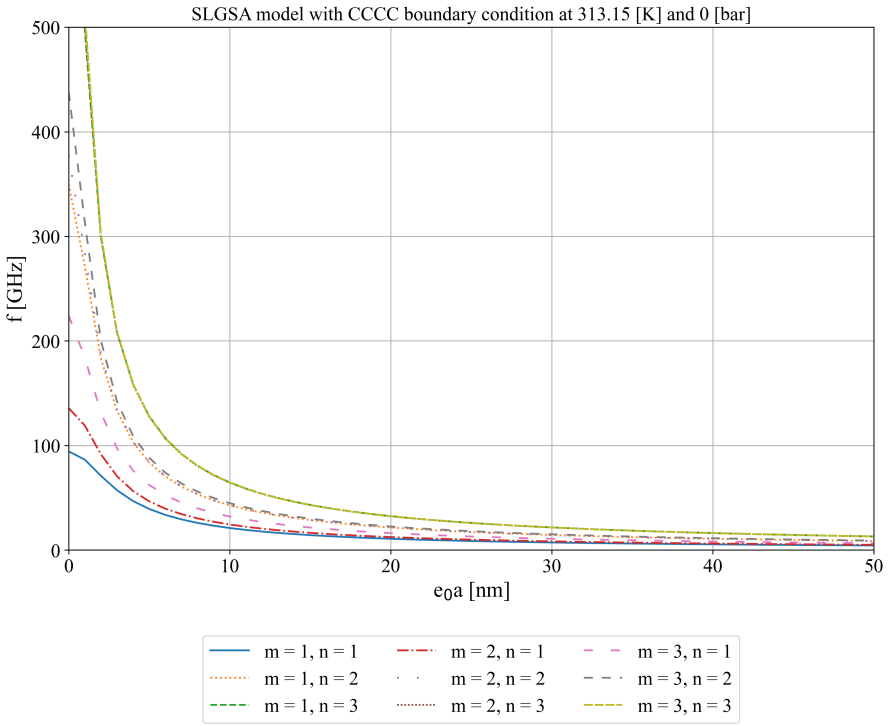

Figure 6.1: The influence of non-local parameter on natural frequencies of SLGSA model with CCCC boundary condition.

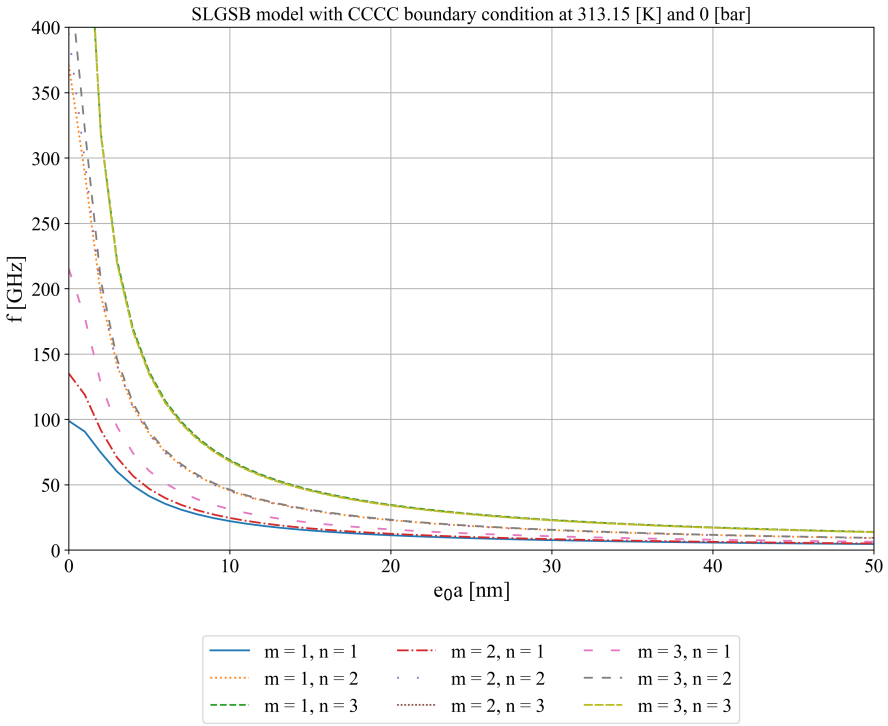

Figure 6.2: The influence of non-local parameter on natural frequencies of SLGSB with CCCC boundary condition.

From Figs. 6.1 and 6.2 it can be seen that as the value of non-local parameter increases the frequency value decreases. If the value of the non-local parameter is zero the frequency equation reduces to the equation from classical plate theory and the natural frequencies have maximum values. These values are too high and could not be achieved using MD simulation with dimensions of SLGSA and SLGSB models. When the value of the non-local parameter is in a range from 1 to 10 nm the values of natural frequencies for all mode shapes of SLGSA and SLGSB plate model drastically drops below 100 GHz. As the value of non-local parameter increases beyond 10 nm the natural frequency values for all mode shapes slowly decrease below 50 GHz. Generally, the high values of natural frequencies can be attributed to two things and these are:

- the size of SLGSA and SLGSB plate model used in these investigations are 19.1×9.4 and 19.5×9.2 nm, respectively. In the previous chapter when the influence of SLGS size on natural frequencies was investigated using MD simulation as the size of SLGS increased the values of natural frequency drastically dropped, and
- exact value of the non-local parameter is unknown.

6.2 Influence of Temperature and Pressure on Natural Frequencies of SLGS

In this section, the influence of temperature and pressure on natural frequencies of the SLGSA and SLGSB plate model with CCCC boundary condition. First, the influence of temperature and non-local parameter variation on natural frequencies are investigated. Then the influence of pressure, temperature variation on natural frequencies of SLGSA and SLGSB plate models are investigated.

6.2.1 Influence of Temperature Variation on Natural Frequencies of SLGS

In these investigations the mechanical parameters obtained using MD simulation for temperatures in range from 233.15 K up to 313.15 K with the step of 10 K will be used in order to investigate the influence of temperature and non-local parameter on natural frequencies of SLGSA and SLGSB model with CCCC boundary condition. There are total of 9 temperature levels that will be used in these investigations. The temperature in these investigations is used in terms of mechanical parameters obtained in Chapter 5 at previously mentioned temperature range. The Eq.(3.42) used in investigation of temperature and non-local parameter variation, can be written in following form

$$f_{mnCCCCT} = \frac{1}{2\pi}\sqrt{\frac{D_{11}\frac{4m^4\pi^4}{L_a^4} + 2(D_{12}+2D_{66})\frac{4m^2n^2\pi^4}{3L_a^2L_b^2} + D_{22}\frac{4n^4\pi^4}{L_b^4}}{\frac{3h\rho}{4}\left(\frac{3}{4} + (e_0a)^2\pi^2\left(\frac{m^2}{L_a^2}+\frac{n^2}{L_b^2}\right)\right)}}. \tag{6.2}$$

The influence of temperature and non-local parameter variation on first natural frequency ($m = 1, n = 1$) of SLGSA and SLGSB plate model with CCCC boundary condition are shown in Figs. 6.3 and 6.4.

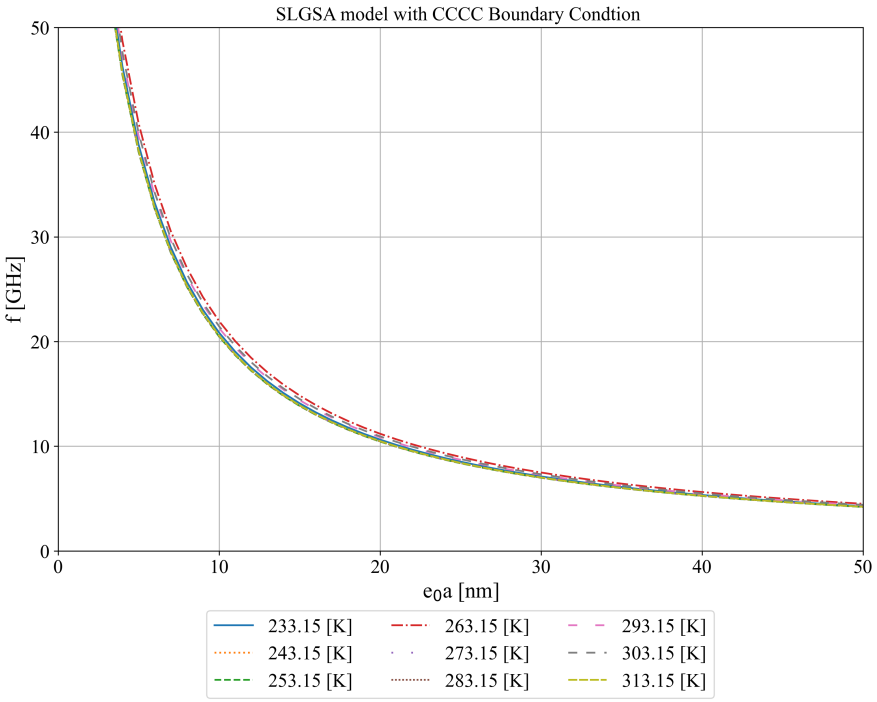

Figure 6.3: The influence of temperature and non-local parameter variation on the first natural frequency $(m = 1, n = 1)$ of SLGSA model with CCCC boudnary condtion.

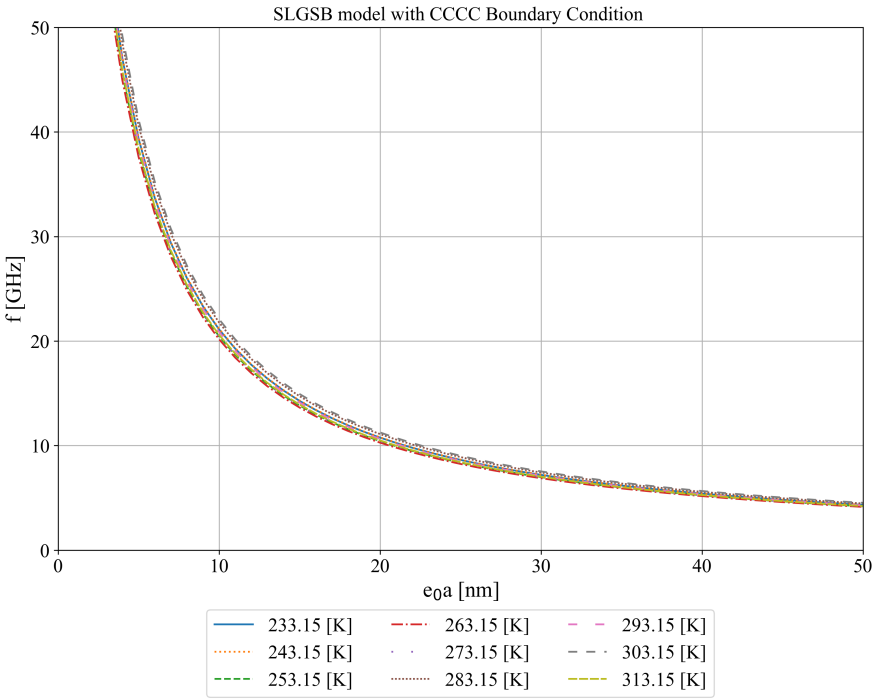

Figure 6.4: The influence of temperature and non-local parameter variation on the first natural frequency $(m = 1, n = 1)$ of SLGSB model with CCCC boudnary condtion.

As seen from Figs. 6.3 and 6.4 the non-local parameter is the most influencing parameter

when compared to the temperature. As the non-local parameter increases the values of natural frequencies decreases. When all curves are compared it can be noticed that as the temperature rises, there is a small change in the natural frequency value.

6.2.2 Influence of Temperature and Pressure Variation on Natural Frequencies of SLGS

For these analyses the temperature is set in range from 233.15 to 313.15 K while pressure is in range from 0 to 1.01325 bar and value of the non-local parameter is set to 1 nm, respectively. The temperature was not directly applied in the frequency equations but the mechanical parameters obtained at these temperatures shown in Tabs. 5.3 and 5.4, were used. The influence of temperature and pressure variation on natural frequencies of SLGSA and SLGSB plate model are calculated using Eq.(3.42) which can be written in following form:

$$f_{mnCCCCPT} = \frac{1}{2\pi}\sqrt{\frac{D_{11}\frac{4m^4\pi^4}{L_a^4} + 2(D_{12}+2D_{66})\frac{4m^2n^2\pi^4}{3L_a^2L_b^2} + D_{22}\frac{4n^4\pi^4}{L_b^4}}{\frac{3PA}{4}\left(\frac{3}{4} + (e_0a)^2\pi^2\left(\frac{m^2}{L_a^2}+\frac{n^2}{L_b^2}\right)\right)}} \tag{6.3}$$

As in the temperature analysis the influence of temperature in this cases is introduced in form of the mechanical parameters obtained in Chapter 5 for different temperature values. The results of influence of pressure and temperature on first natural vibration of SLGSA and SLGSB system with CCCC boundary condition, are shown in Figures 6.5 and 6.6.

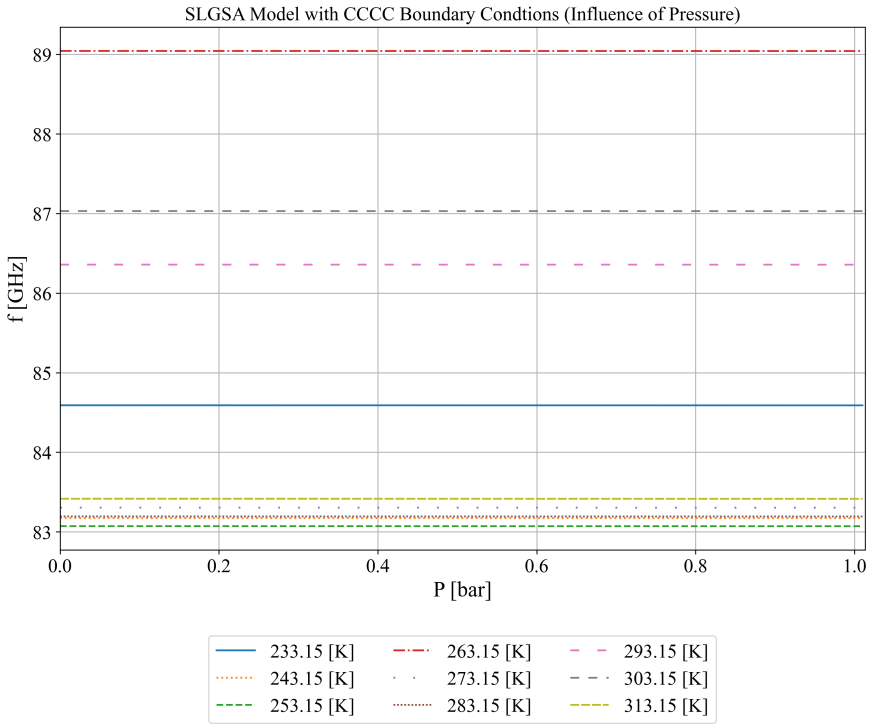

Figure 6.5: The influence of temperature and pressure on frequency of SLGSA model with CCCC boundary condition.

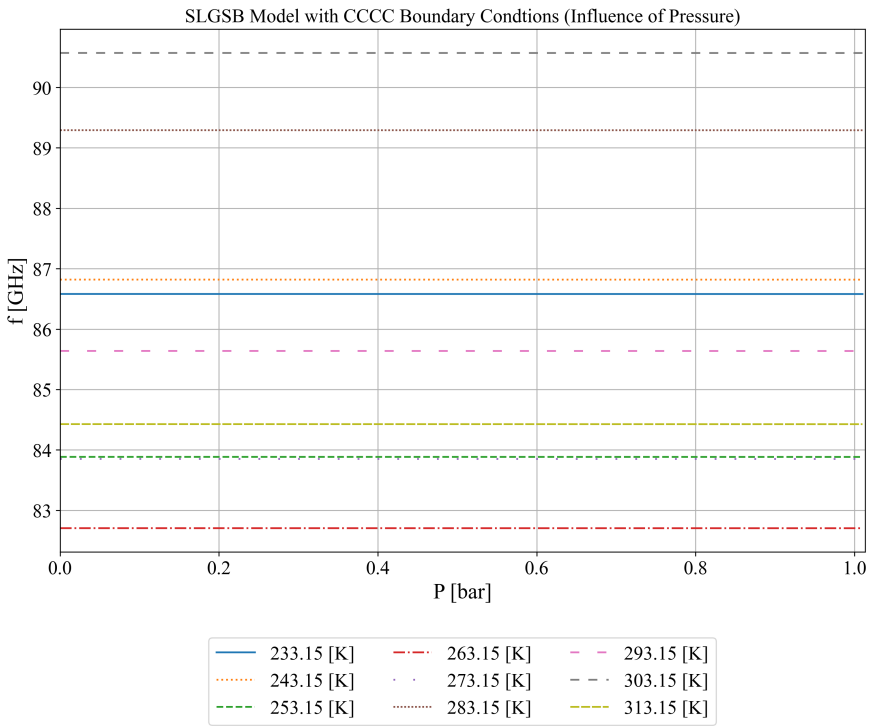

Figure 6.6: The influence of temperature and pressure on frequency of SLGSB model with CCCC boundary condition.

As seen from Figs. 6.5 and 6.6 the pressure has not any visible influence on natural frequencies when compared to temperature influence. However, the pressure influence on the natural vibration of SLGS plates still exists. For example, the frequency of the SLGSA plate model with CCCC boundary condition at 233.15 K and 0 bar is equal to 84.59 GHz, while the same plate at 233.15 K and 1.01325 bar have the natural frequency equal to 84.589 GHz. This means that the total difference of natural frequency due to the pressure influence is equal to 0.001 GHz. The reason why the influence of pressure is almost negligible is due to the small size of the SLGS plate model and boundary condition used in this investigation. As mentioned in the previous chapter the size of the SLGS model has a huge influence on natural frequency. As the size of the SLGS model increases the values of natural frequencies decrease. Since the size of the SLGS model is 19.1×9.4 and 19.5×9.2 nm is very small it will generate a very high natural frequency. In the previous chapter, it was also concluded that the influence of pressure will be omitted from the MD analyses due to the high-pressure fluctuation during the equilibration and vibration simulations. So, due to the negligible influence of pressure on natural vibrations in non-local plate theory and high fluctuations of pressure in MD simulation the influence of pressure will be omitted from further analyses.

6.2.3 Influence of SLGS Size on Their Natural Frequencies

In this section, the influence of SLGSA and SLGSB plate model size on their natural frequencies is investigated. The size of the plate will be varied in x and y direction while the plate thickness will remain constant. The range of SLGS plate size is from 19.1×9.2 nm up to 2000×1000 nm. The technical specification of each model used in these investigations is given in Tab. 6.2. In these analyses, the mechanical parameters obtained using REBO potential in the previous chapter in the temperature range from 233.15 K up to 313.15 K was used. In these analyzes, the value of the non-local parameter was set to 1 nm and the first mode shape $(m = 1, n = 1)$ is taken into account.

Table 6.2: The dimensions of SLGS used in investigation of size influence on natural frequencies of SLGSA and SLGSB plate model in temperature range 233.15 - 313.15 [K]

Case number	1	2	3	4	5	6	7	8	9	10	11
Size of	20	30	40	50	100	200	300	400	500	1000	2000
SLGSA/	×	×	×	×	×	×	×	×	×	×	×
SLGSB [nm]	10	15	20	25	50	100	150	200	250	500	1000

However, it should be noted that in these analyses instead of dimensions 20×10, 30×15 and 40×20 nm the actual dimensions of SLGSA and SLGSB plate model shown in Tab.

6.1 will be used. The results of size influence on natural frequencies of SLGSA and SLGSB model with CCCC boundary conditions is shown in Figures 6.7 and 6.8.

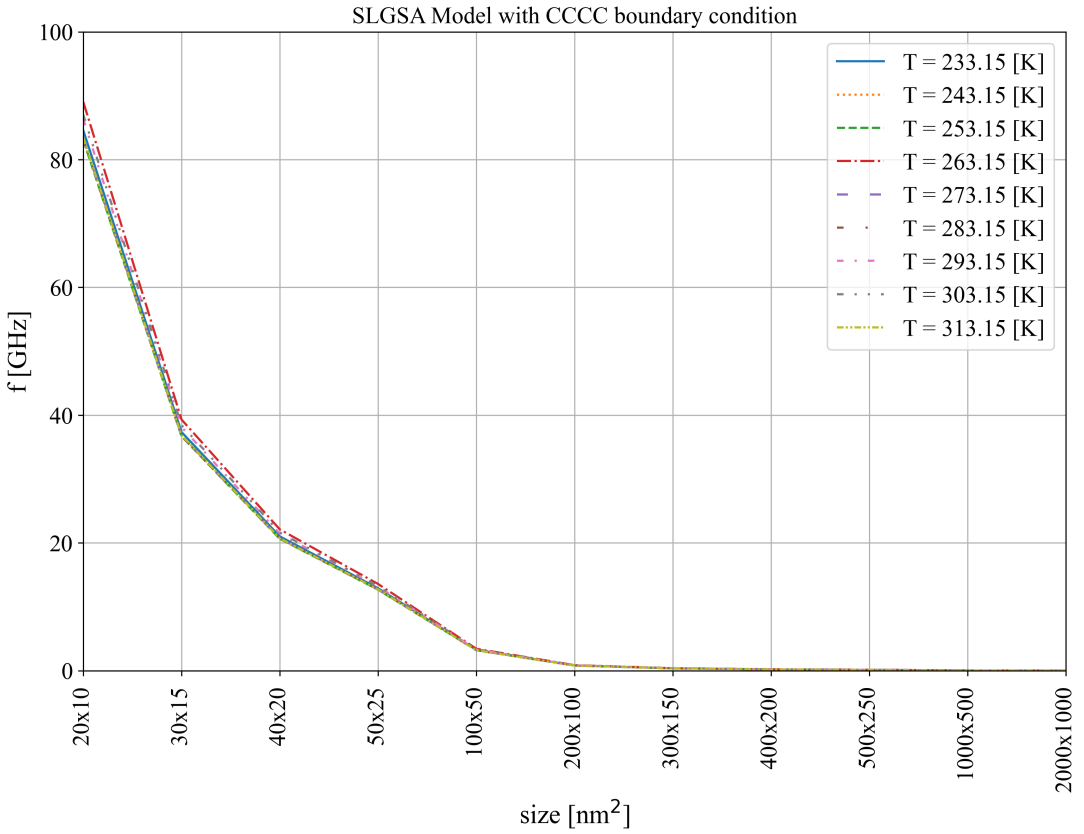

Figure 6.7: The influence of non-local parameter on natural frequencies of SLGSA model with CCCC boundary condition.

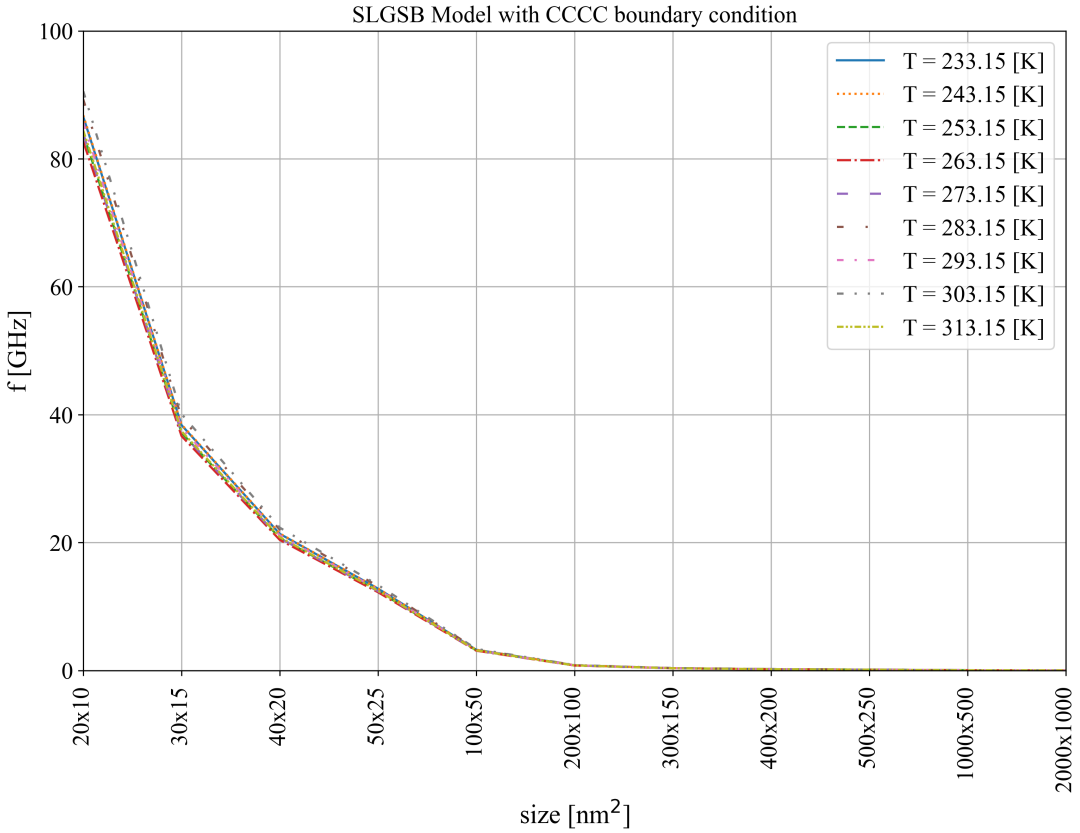

Figure 6.8: The influence of non-local parameter on natural frequencies of SLGSB model with CCCC boundary condition.

As seen from Figures 6.7 and 6.8 as the size of plate model increases the value of natural frequency rapidly decreases. The highest frequencies are obtained for SLGS with size of 20×10 nm and as the size increases beyond 200×100 nm the value of natural frequency drops down to MHz range. The size used in [32] was 1100×1930 nm and they achieved frequency of 70.5 MHz. For analyses with the SLGS size of 1000×500 nm achieves natural frequency of 33.6 MHz while SLGS with size of 2000×1000 nm achieves natural frequency of 8.4 MHz. The frequency difference between those obtained in [32] and non-local plate theory can be attributed primarily to uncertainty of the non-local parameter and to mechanical and thermodynamic parameters used in these analyses. Another important factor is that the non-local parameter has extremely low influence on structures with large dimensions, and the solution will automatically converge to ones obtained by the local model.

6.3 Absolute and Relative Frequency Shift Analysis

In this section, the absolute and relative frequency shift caused by gas/vapor molecules attached at the surface of the SLGS plate model will be described. To determine the absolute and frequency shift caused by the attached gas/vapor molecule to the surface of the SLGS plate first the natural frequencies of the SLGS plate model must be determined. These natural frequencies for the SLGS plate model with CCCC boundary conditions were obtained in the previous section.

6.3.1 Absolute Frequency Shift

For these analyses the values of non-local parameter were 0,1,2,3 and 4 nm, and the temperature was set to 313.15 K. The general formula used to obtain the absolute frequency shift is defined in Chapter 5 with the Eq.(5.11). The mechanical and thermodynamic parameters used to obtain the natural frequencies of the SLGSA plate model and natural frequencies of the SLGSA model with attached gas/vapor molecules at the SLGSA center are those obtained with MD Simulations using REBO potential at the previously mentioned temperature. The first natural frequency of SLGSA and SLGSB plate without attached nanoparticle at the center of SLGSA and SLGSB plates are obtained using the Eq.(6.1). After the natural frequencies of SLGSA and SLGSB plates with CCCC boundary conditions are obtained for different values of non-local parameter at the temperature of 313.15 K the next step is to obtain the natural frequencies of SLGSA and SLGSB plate with CCCC boundary condition with attached nanoparticle with mass equal to those molecules given in Tab. 2.5. The influence of attached nanoparticle mass attached at the center of SLGSA and SLGSB plate model with CCCC boundary condition on the first natural frequency is calculated using the Eq.(3.42) which can be written in the following form

$$f_{mnCCCCCPATM} = \frac{1}{2\pi}\sqrt{\frac{D_{11}\frac{4m^4\pi^4}{L_a^4} + 2(D_{12}+2D_{66})\frac{4m^2n^2\pi^4}{3L_a^2L_b^2} + D_{22}\frac{4n^4\pi^4}{L_b^4}}{X_{CCCCPATM}}}, \tag{6.4}$$

where the full form of coefficient $X_{CCCCPATM}$ is defined in Eq.(3.43). Since the nanoparticle is attached at the center the x and y coordinates of the attached nanoparticle are equal to $0.5L_a$ and $0.5L_b$, respectively. The position of attached nanoparticle is usually introduced into the coefficient $X_{CCCCPATM}$ as two non-dimensional positional variables $\xi = \frac{x}{L_a}$, and $\eta = \frac{y}{L_b}$, respectively. In this investigation the value of these two variables is equal to 0.5 since the attached nanoparticle is located at the center of SLGSA and SLGSB plate model. In Fig. 6.9 and 6.10 the absolute frequency shift change versus the attached mass of gas/vapor molecules at the center of SLGSA and SLGSB plate model with CCCC boundary condition are shown.

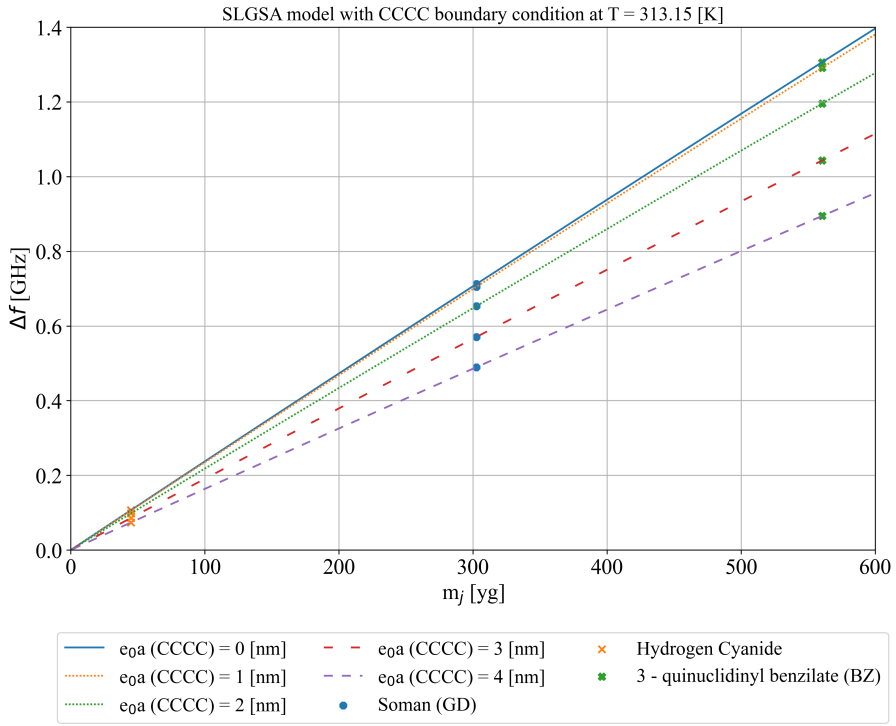

Figure 6.9: The absolute frequency shift of SLGSA plate model with CCCC boundary condition versus mass of attached mass at SLGS center ($\xi = 0.5, \eta = 0.5, m = 1, n = 1$, $T = 313.15$ K).

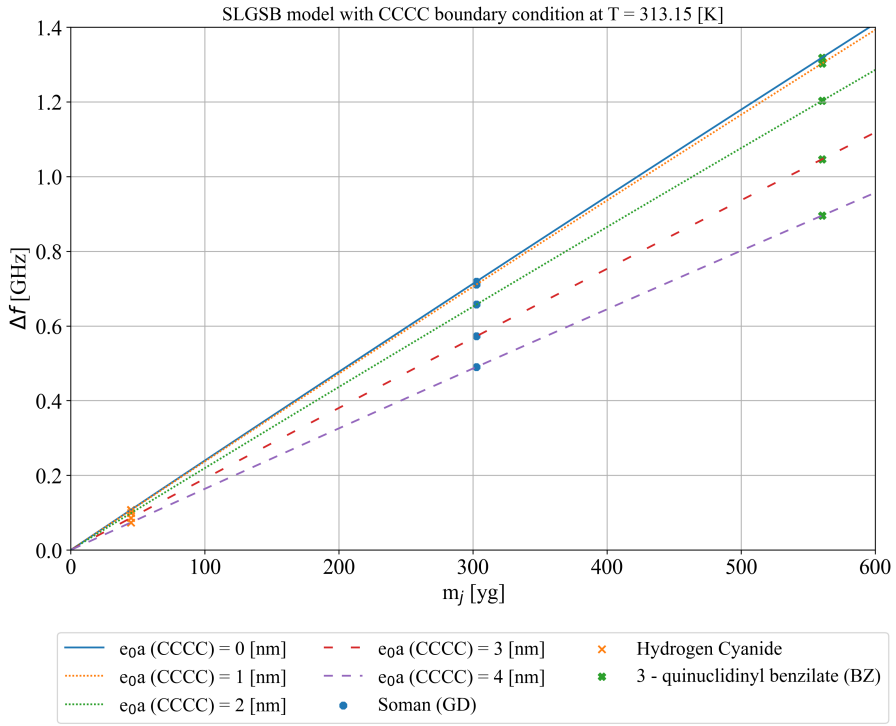

Figure 6.10: The absolute frequency shift of SLGSB plate model with CCCC boundary condition versus mass of attached mass at SLGS center ($\xi = 0.5, \eta = 0.5, m = 1, n = 1$, $T = 313.15$ K).

From Figs. 6.9 and 6.10 the absolute frequency shift versus attached mass at the center of SLGSA and SLGSB plate model with CCCC boundary conditions for different values of the non-local parameter are shown. Generally, the absolute frequency shift increases as the mass of the attached gas molecule increases. The non-local parameter has a decreasing effect on absolute frequency shift curves. As the non-local parameter rises the slope of the absolute frequency shift curve decreases. A total of 3 gas/vapor molecules were used to investigate if SLGSA and SLGSB model could detect these molecules. For each value of the non-local parameter, the absolute frequency shift is calculated that is caused by each gas/vapor molecule attached at the center of the SLGSA and SLGSB plate model. If the absolute frequency shift value caused by each molecule lies on the absolute frequency shift curve this means that the SLGSA and SLGSB model are capable of detecting this molecule. From Figs. 6.9, and 6.10 it can be seen that all these molecules could be detected by the SLGSA and SLGSB plate model for different values of non-local parameter.

6.3.2 Relative Frequency Shift

To calculate the relative frequency shift first the absolute frequency shift must be determined. The relative frequency shift can be described as the ratio between the absolute frequency shift and the natural frequency of the model with the attached mass. The equation for calculating relative frequency shift is defined by Eq.(5.12) in the previous chapter. The results of relative frequency shift analysis were obtained for the SLGSA and SLGSB plates at the temperature of 313.15 K for 3 different molecules attached at the center of these plates. The mechanical and thermodynamic parameters used for these analyses were those obtained using MD Simulation with REBO potential. In Figures, 6.11 and 6.12 the relative frequency shift versus attached mass at the center of SLGSA and SLGSB plate model with CCCC boundary condition are shown.

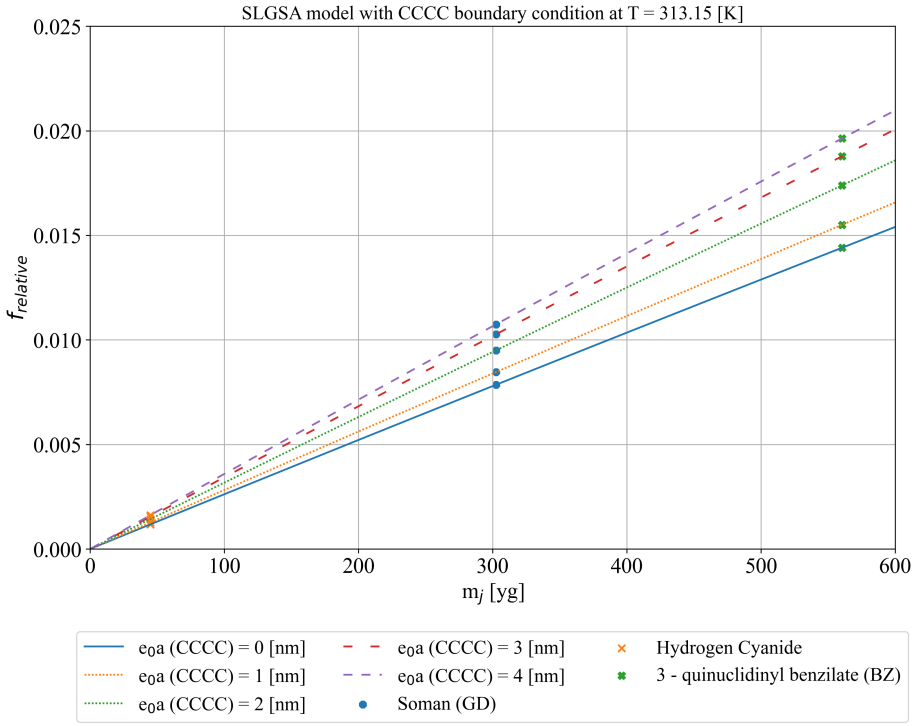

Figure 6.11: The relative frequency shift of SLGSA plate model with CCCC and SSSS boundary conditions versus mass attached at its center ($\xi = 0.5, \eta = 0.5, m = 1, n = 1$, $T = 313.15$ K).

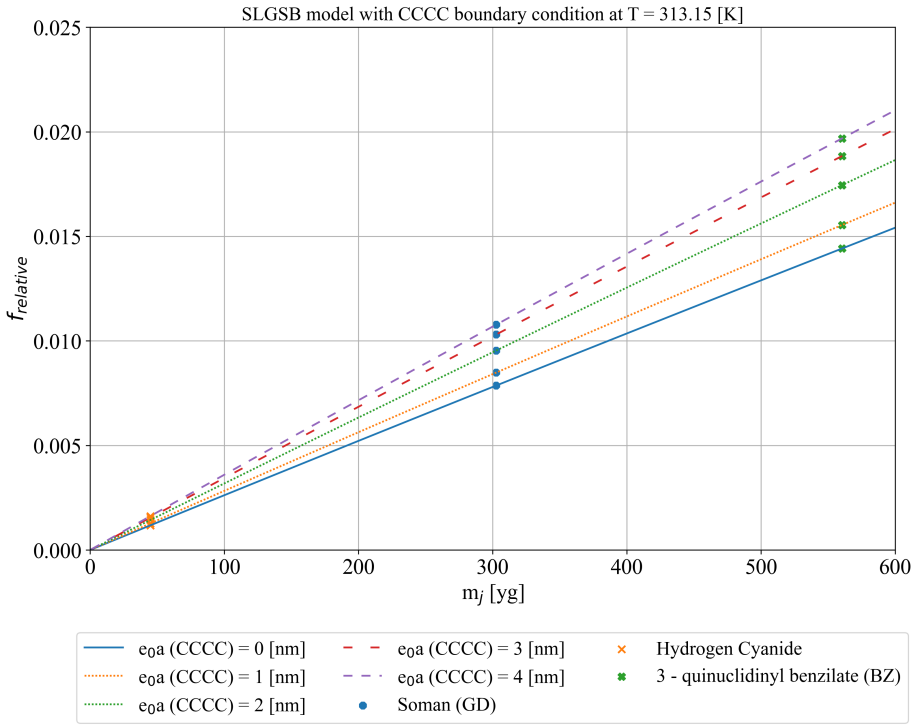

Figure 6.12: The relative frequency shift of SLGSB plate model with CCCC boundary condition versus mass of attached at its center($\xi = 0.5, \eta = 0.5, m = 1, n = 1$, $T = 313.15$ K).

From Figs. 6.11 and 6.12 it can be seen that relative frequency shift curves increase as the mass of attached gas/vapor molecule at the center of SLGSA and SLGSB plate model increases. The non-local parameter in the case of relative frequency shift has the opposite effect when compared to the absolute frequency shift analysis. As the value of non-local parameters increases the slope of relative frequency shift curves also increases. As in the case of absolute frequency shift analysis if the relative frequency shift value caused by the attached gas/vapor molecule lies on the relative frequency shift curve this means that the SLGS structure could detect the gas/vapor molecule.

7. Estimation of the Non-local Parameter of Graphene Sheet Nanosensor Using Genetic Programming Algorithm

In this chapter, the creation of the dataset using MD simulation and non-local plate theory, and implementation of the GP algorithm to obtain the mathematical expression for calculation of the non-local parameter is described. To create the dataset, the MD vibration simulations of different SLGS structures must be performed. The natural frequencies obtained with MD simulations will be used as the reference natural frequencies. In order to obtain the natural frequencies using MD simulations, 3 different SLGS models were used in terms of size, ranging from 20×10 nm up to 40×20 nm. So the total number of SLGS models is 6. Each structure was equilibrated using the same procedure described in Chapter 5 at temperatures of 233.15, 273.15, and 313.15 K. To obtain the natural frequencies of SLGSA and SLGSB model with CCCC boundary condition total of 60 simulations were performed using the same procedure as described in Chapter 5. The obtained natural frequencies using MD were used to tune the natural frequency values of non-local theory by adjusting the non-local parameter value. The mechanical parameters used in this dataset are those obtained in Chapter 5 at previously mentioned temperatures. After the dataset was obtained the GP algorithm was utilized to obtain the symbolic expression that correlates input variables such as: natural frequency, mechanical parameters (E_{xx}, E_{yy}, G_{xy}, and ν_{xy}), temperature (T) with output variable (non-local parameter).

7.1 Tuning the non-local parameter

To obtain the output value the natural frequencies from the non-local plate theory must be equalized with those obtained from MD simulation. The mechanical parameters obtained from MD simulations as well as dimensions of models used in the aforementioned

simulations were used in the non-local plate theory. The natural frequencies of SLGS plate models obtained using the non-local plate theory were adjusted with those obtained using MD simulations by adjusting the value of the non-local parameter. After the natural frequencies were adjusted the values of the non-local parameter were obtained which will be used as the output values in the dataset. The entire dataset consists of 60 instances which were divided into training and testing portions in a ratio of 80:20. The testing dataset was used in the GP algorithm to obtain symbolic expressions while the testing dataset was used to test the obtained symbolic expressions to measure their accuracy in terms of the R^2 score. The first 10 instances of the dataset are shown in Table 7.1.

Table 7.1: The example of the dataset used to obtain symbolic expression using GP algorithm

T [K]	f [GHz]	E_{xx} [TPa]	E_{yy} [TPa]	G_{xy} [TPa]	ν_{xy}	L_a [nm]	L_b [nm]	e_0a [nm]
313.15	14	0.90429	0.895278	0.391707	0.1769	40	20	5.451
313.15	15	0.9093	0.8978	0.3783	0.2522	40	20	4.79
273.15	15.5	0.98842	0.890565	0.393303	0.144	40	20	4.112
273.15	16	0.9616	0.8855	0.3562	0.2715	40	20	4.154
233.15	17	1.06092	0.955185	0.39467	0.147	40	20	3.834
233.15	18	1.0609	0.923	0.3611	0.2541	40	20	3.126
313.15	25	0.9093	0.8978	0.3783	0.2522	30	15	3.862
313.15	26	0.90429	0.895278	0.391707	0.1769	30	15	4.197
273.15	27	0.98842	0.890565	0.393303	0.144	30	15	3.604
273.15	28	0.9616	0.8855	0.3562	0.2715	30	15	3.321

As seen from Tab. 7.1 the E_{xx}, E_{yy}, and G_{xy} parameters are in TPa, the natural frequency obtained using the MD simulation and non-local plate theory is in GHz, and dimensions of SLGSA and SLGSB model are in nm. These values are not transformed into Pa and Hz because it would generate very large numbers. If such large numbers were used as an input in the GP algorithm it would generate extremely large output values and the algorithm would not be able to produce an accurate estimation of output value. The variation of the non-local parameter versus natural frequency is shown in Fig. 7.1.

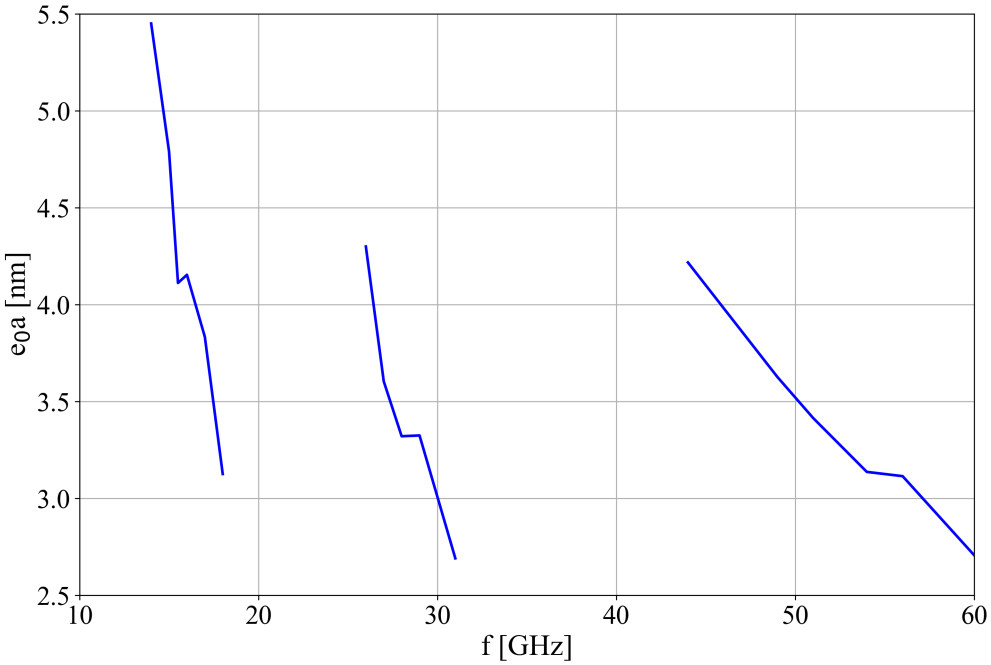

Figure 7.1: The variation of the non-local parameter versus natural frequency obtained using MD simulation.

As seen from Fig. 7.1 it can be noticed that for low natural frequency values the value of non-local parameter is high. It should be noted that the low natural frequency values were obtained for large SLGS models (40×20 nm), the natural frequencies of SLGS models 30×15 nm are in range from 25 to 33 GHz while the highest natural frequencies are obtained for SLGS models 20×10 nm. The obtained natural frequencies are in accordance with the investigation conducted in Chapters 5, and 6 where the investigation of SLGS size influence on natural frequencies showed that as the size of SLGS model increased the value of natural frequency decreases. As the values of natural frequencies increases the value of non-local parameter decreases.

For better visualization of the dataset the non-local parameter versus width (L_b) of SLGS model in y-direction is shown in Fig. 7.2.

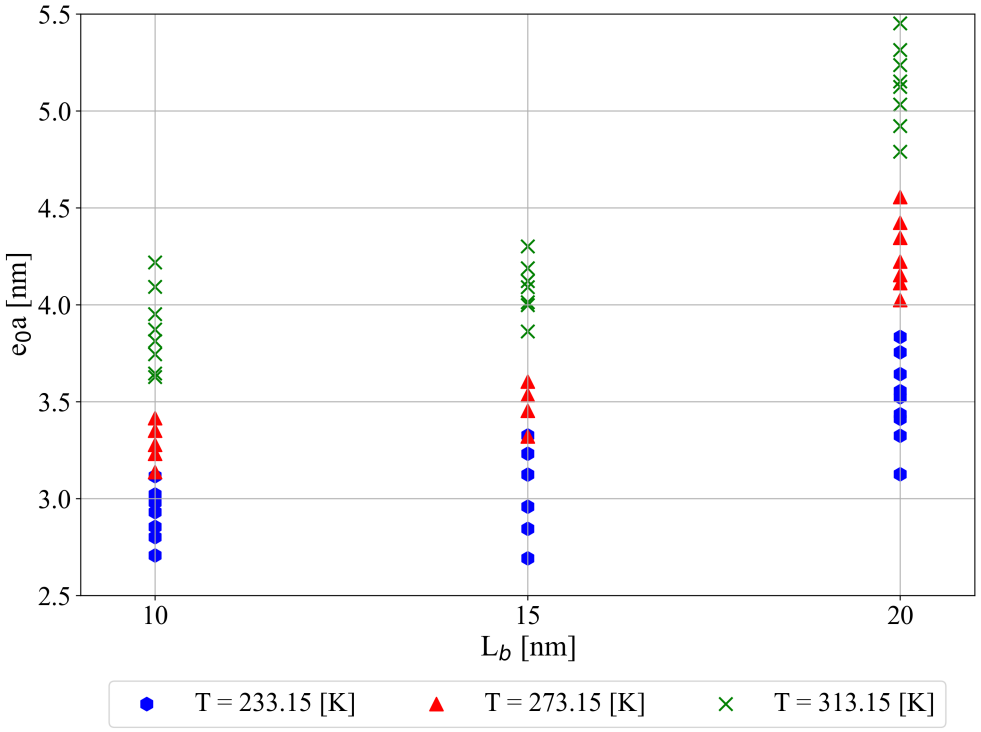

Figure 7.2: The variation of non-local parameter versus width of SLGS model in y-direction.

As seen from Fig. 7.2 as the value of the SLGS width (L_b) increases the value of the non-local parameter also increases. So, the highest values of the non-local parameter are those obtained in the case of SLGSA and SLGSB model with size 40×20 nm. From Fig.7.2 it can also be noticed that the temperature also influences the non-local parameter. For each width of the SLGS model (L_b) as the temperature increases, the value of the non-local parameter also increases. When the range of the non-local parameter for widths of 10 and 15 nm are compared it can be noticed that the non-local parameter range for the SLGS width of 15 nm is slightly higher than the non-local parameter range for the SLGS width of 10 nm. However, the highest increase in the non-local parameter range can be noticed when the non-local parameter range for SLGS width of 20 nm is compared with the previous two.

When the values of the non-local parameter shown in Figs. 7.1, and 7.2 are compared to the values given in Tab. 3.1 it can be noticed that the values of non-local parameter in this investigation (2.5 - 5.5 nm) are higher than those listed in Tab. 3.1 (0 - 2.1 nm). Only one research paper [158] used the non-local parameter range from 0 - 45 nm to investigate the natural vibrations of the SLGS plate model. Most of the non-local parameter values presented in the Tab. 7.2 were used in investigations where the temperature was 0 K. However, in [157], the influence of temperature on non-local parameter was performed in the range from 0 to 100 K, and the results showed that as the temperature increases

the value of non-local parameter also increases. This means that the non-local parameter is also temperature-dependent. Due to the small temperature range used in [157] the values of the non-local parameter are in a range from 0 to 2 nm. If the temperature range was higher the values of the non-local parameter would be higher. However, the results presented in [157] are in accordance with the previously obtained results.

7.2 Results obtained with GP Algorithm

To obtain the symbolic expression for estimation of the non-local parameter value the parameters of the GP algorithm were initially set in a specific range. In each execution of the GP algorithm, the parameters were randomly chosen and used in the analysis. The parameters range of the GP algorithm is shown in Tab. 7.2.

Table 7.2: The range of GP parameters used to obtain the symbolic expression for estimation of non-local parameter value

Parameter name	Lower Bound	Upper Bound
Population size	500	1000
Number of generations	100	1000
Tournament size	50	100
Tree depth	3-6	7-12
Crossover coefficient	0.9	1
Subtree mutation coefficient	0.01	0.1
Hoist mutation coefficient	0.01	0.1
Point mutation coefficient	0.01	0.1
Stopping Criteria	1×10^{-5}	0.01
Maximum number of samples	0.9	1
Constant range	-1000	1000
Parsimony coefficient	1×10^{-5}	0.01

As seen from Tab. 7.2 there is a total of 12 GP parameters range were defined and the GP algorithm in each execution randomly selects parameters values from prespecified parameters range. The population size range was set from 500 to 1000 population members. These population members were evolved for several generations in the range from 100 to 1000. In each generation, the 50 to 100 population members were competing to become members of the next generation. This means that on the best population members that were selected in tournament selection the crossover and mutation operations were

performed to generate new population members of the next generation. As described in Chapter 4 the ramped half-and-half method was used to create the initial population represented as tree structures. This means that half of the population was created using the full method and half of the population was created using the grow method. Initially, this method is good enough to achieve diversity in the initial population. However, to achieve even higher diversity between population members the tree depth range was utilized.
As seen from Tab. 7.2 the prespecified tree depth range is from 3 to 12. So, for example, if the randomly selected tree depth is (3,12) this means that the initial population represented as tree structures will be created with three depths ranging from 3 to 12. In these analyses, the dominant genetic operator is crossover since the value of this coefficient is in the range from 0.9 to 1. However, the sum of all genetic operator coefficients must be equal to 1 so the value of the crossover coefficient was never equal to 1. The other three mutation coefficient values were set in a prespecified range from 0.01 to 0.1. The stopping criteria value was set in a prespecified range from 1×10^{-5} up to 0.01. This value is the lowest value that can be achieved during GP algorithm execution, and if this value is achieved by one of the population members the execution of the GP algorithm is terminated. It should be noted that the fitness function used in all these analyses is the MAE value. However, this value was never achieved and the execution of the GP algorithm was terminated after the GP algorithm reached the maximum number of generations.
The maximum number of samples value is the value of the percentage of the training dataset which is used for the evaluation of population members in each generation. The prespecified range of this value was in the range from 0.9 to 1 or in other words the prespecified portion range of the training dataset used in the GP algorithm was between 90 % to 100 %. The prespecified range of constants is from -1000 to 1000 which is used for the construction of the initial population and during the genetic operations on population members. This range consists of numeric values which are used in combination with input variables and mathematical functions to formulate symbolic expressions (population members). The parsimony coefficient value is responsible for penalizing large programs by making them less favorable for tournament selection. In the case of GP algorithm execution when the fitness value is unable to decreases the size of population members tends to rapidly grow in terms of length. This phenomenon in the GP algorithm is called the bloat phenomenon. To prevent the rapid growth of population members from generation to generation, the parsimony coefficient is introduced. The higher the value of this coefficient the slower growth of population members in terms of length will occur. In this case, the range of parsimony coefficient value is low (1×10^{-5} to 0.01), since with higher values the population members were unable to evolve which did not generate accurate symbolic expression in terms of non-local parameter estimation.

Besides GP parameters range the mathematical functions that will be used in the GP algorithm to obtain symbolic expression must be defined. In these analyses the used mathematical functions were: addition, subtraction, multiplication, division, square root, absolute value, and natural logarithm.
After the symbolic expressions were obtained they were evaluated on the testing portion of the dataset using the coefficient of determination R^2 value that is calculated with Eq.(5.7). The best symbolic expression can be written in the following form

$$y_{e_0a1} = \left(|\nu_{xy}|(-(|L_b - \frac{T}{f}| + 5.46812)) - \frac{-L_b + T + 7.71868}{\sqrt{\nu_{xy} 59.5781 - f} - f} + \sqrt{-\frac{T}{\sqrt{\frac{L_b+T}{\frac{\nu_{xy}+T}{\sqrt[4]{7.71868-f}} - \nu_{xy} + 7.71868}} - f} - \sqrt[4]{\frac{T}{f} - 0.0894976} - f + \nu_{xy}} \right)^{\frac{1}{2}}, \tag{7.1}$$

As seen in Eq.(7.1) the input variable E_{xx}, E_{yy}, G_{xy} and L_a are not included in these symbolic expressions. The only input parameters included in both symbolic expressions are T, f, ν_{xy} and L_b. In Tab. 7.3 the two symbolic expressions obtained using GP algorithm, with corresponding R^2 value are shown.

Table 7.3: The GP parameters used to obtain two symbolic expressions with corresponding R^2 score achieved in estimation of the non-local parameter

Equation	GP Parameters	R^2 score
y_{e_0a1}	977, 650, 89, (4, 8), 0.94, 0.013, 0.019, 0.0102, 0.0023, 0.959, (-645.54, 276.79), 0.00032	0.9688

In Tab. 7.3 the size of population members that were randomly selected from the prespecified range shown in Tab.7.2 is 977. These population members were evolved for 650 generations. In these analyses, the maximum number of generations was used as the primary stopping criteria of the GP algorithm since the stopping criteria value was never achieved. In each generation total of 89 population members were competing to become members of the next generation which means that on the population members that passed tournament selection the genetic operations (crossover and mutation) were performed. The initial population was generated with tree depth in the range (4,8). When the coefficient of genetic operators are compared it can be noticed that the crossover coefficient value is much higher than the mutation coefficient value which means that the dominant genetic operation was a crossover. The stopping criteria value was randomly chosen and is equal to 0.0023. However, this value was never achieved during the GP

execution so the GP algorithm was stopped after the maximum number of generations are reached. The maximum number of samples was randomly chosen value of 0.959. This means that 95.9 % of the training portion of the dataset was used to evaluate population members in each generation. The values of the constant range that was used to create the initial population and later in genetic operations from generation to generation were (-645.54, 276.79). The randomly chosen parsimony coefficient value from the prespecified range was very low (0.00032). Although this value is extremely low the bloat phenomenon during the execution of the GP algorithm did not occur.
The comparison of the real data with the data obtained with symbolic expression is shown in Fig. 7.3.

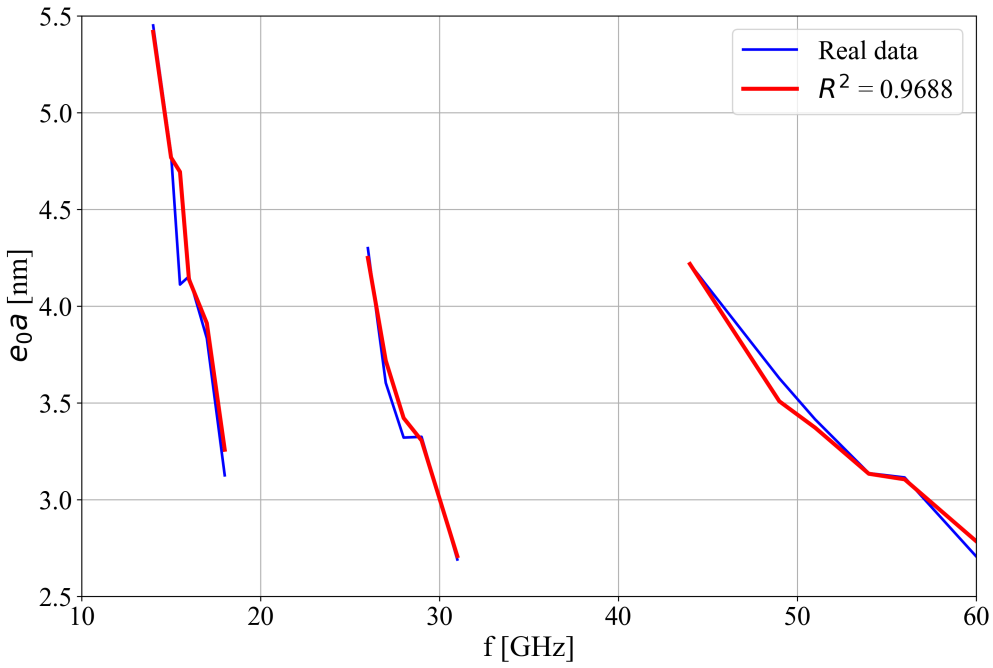

Figure 7.3: The comparison of non-local estimation obtained with two symbolic expressions with the non-local values from the dataset.

As seen in Fig. 7.3 the symbolic expression follow the real data with smaller deviations.

7.2.1 Validation of Obtained Symbolic Expressions

The obtained symbolic expression is given in Eq. (7.1) will be used to calculate the absolute and relative frequency shift caused by attached molecules from Tab. 2.5 at the center of SLGSA and SLGSB plate model with CCCC boundary conditions. First, the values of natural frequencies obtained in Chapter 6 for SLGSA and SLGSB model with and without attached gas/vapor molecules are used alongside mechanical parameters and dimensions in Eq.(7.1) to obtain values of the non-local parameter. These values are then

used to calculate the natural frequencies of SLGSA and SLGSB plate models without added mass using Eq. (6.1) while the natural frequencies of SLGSA and SLGSB plate models with attached gas/vapor molecule were calculated using the Eq. (6.4), respectively. After all-natural frequency values were obtained the absolute and relative frequency shift were calculated using the Eqs. (5.11), and (5.12), respectively. The variation of absolute and relative frequency shift caused by attached CWA molecules is shown in Figs. 7.4 and 7.5.

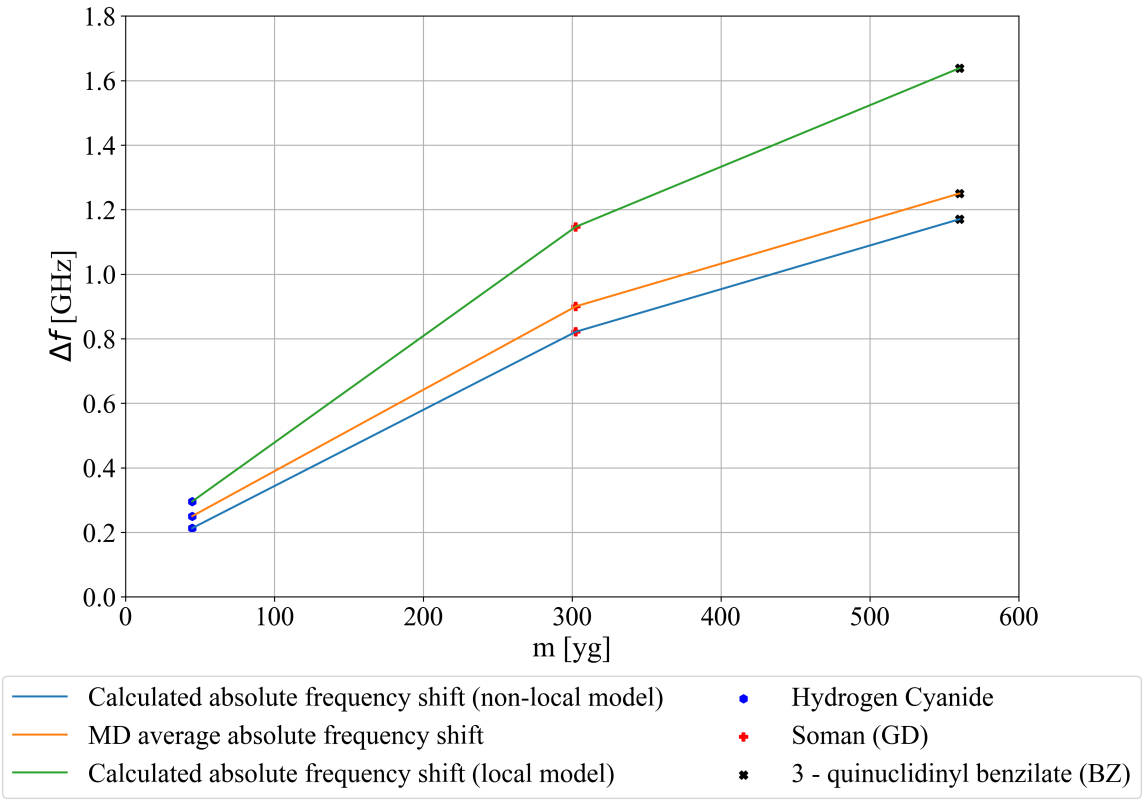

Figure 7.4: The comparison of estimated absolute frequency shift with the average MD absolute frequency shift versus mass of the attached gas/vapor molecules at the center of SLGSA plate with CCCC boundary condition.

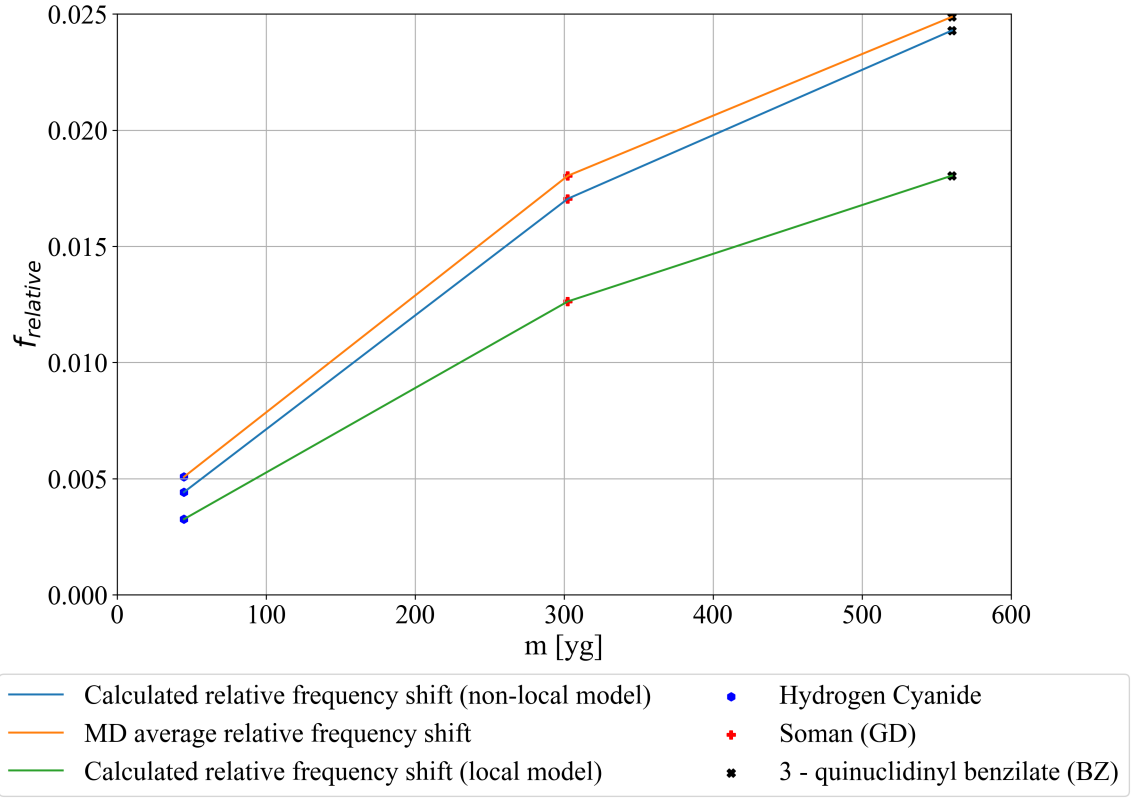

Figure 7.5: The comparison of estimated relative frequency shift with the average MD relative frequency shift versus mass of the attached gas/vapor molecules at the center of SLGSA plate with CCCC boundary condition.

In Figs. 7.4 and 7.5 it can be noticed that the calculated absolute and relative frequency shift for which the values of the non-local parameter were obtained using Eq. (7.1) have the same trend as the average absolute frequency shift values obtained with MD. However, the calculated values of absolute frequency shift are on average 5% lower than the average absolute frequency shift values obtained using MD simulations. From Fig. 7.4 it can also be noticed that as the value of the non-local parameter rises the slope of absolute frequency shift curves decreases. The calculated absolute frequency shift for the local model ($e_0a = 0$ nm) has much higher values than the absolute frequency shift values obtained using MD simulations and those obtained with non-local plate theory in which the value of the non-local parameter is calculated using Eq. (7.1). The smallest deviation between absolute frequency shift values can be noticed in the case of the SLGSA plate model with the attached nanoparticle whose mass is equal to the mass Hydrogen Cyanide molecule. The highest deviation between absolute frequency shift values can be noticed in the case of the SLGSA model with an attached nanoparticle whose mass is equal to the mass of 3-quinuclidinyl benzilate (BZ).

As the value of the non-local parameter increases the slope of calculated relative frequency

shift curves increases as well, Fig. 7.5. The smallest values of relative frequency shift are those obtained in the case of a non-local plate theory in which the value of the non-local parameter is 0. The highest values of relative frequency shift are those obtained using the MD simulations. The relative frequency shift values obtained with the non-local plate theory in which Eq. (7.1) is used to calculate the non-local parameter value are near those obtained using the MD simulations. As the mass of the attached nanoparticle increases it can be noticed that the relative frequency shift values obtained with the non-local plate theory in which the non-local parameter value is 0 nm highly deviations from the other two relative frequency shift curves.

The same procedure is used to calculate the absolute and relative frequency shift values caused by CWA molecules attached at the center of SLGSB plate with CCCC boundary condition in which the non-local parameter was obtained using the Eq. (7.1). In Figs. 7.6 and 7.7 the comparison of the calculated absolute and relative frequency shift for different values of the non-local parameter with averaged absolute and relative frequency shift values obtained using MD simulations shown.

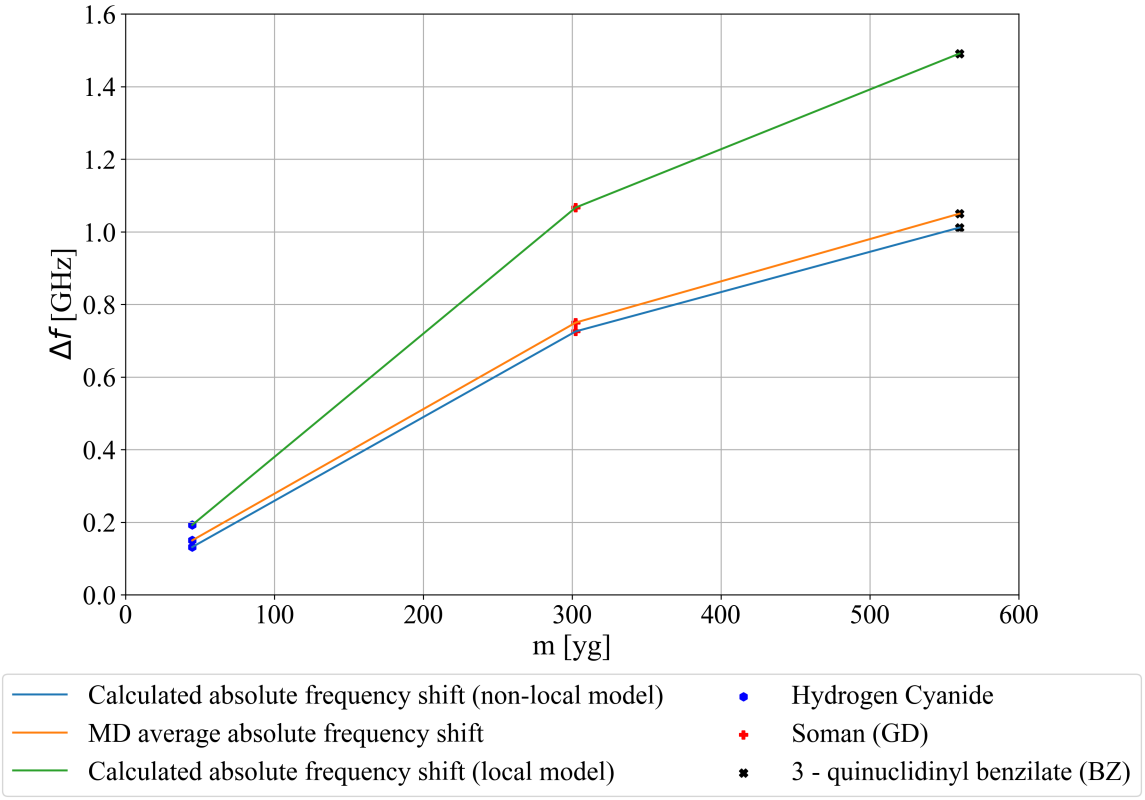

Figure 7.6: The comparison of calculated absolute frequency shift with average absolute frequency shift obtained using MD simulations for gas/vapor molecules attached at the center of SLGSB model with CCCC boundary condition.

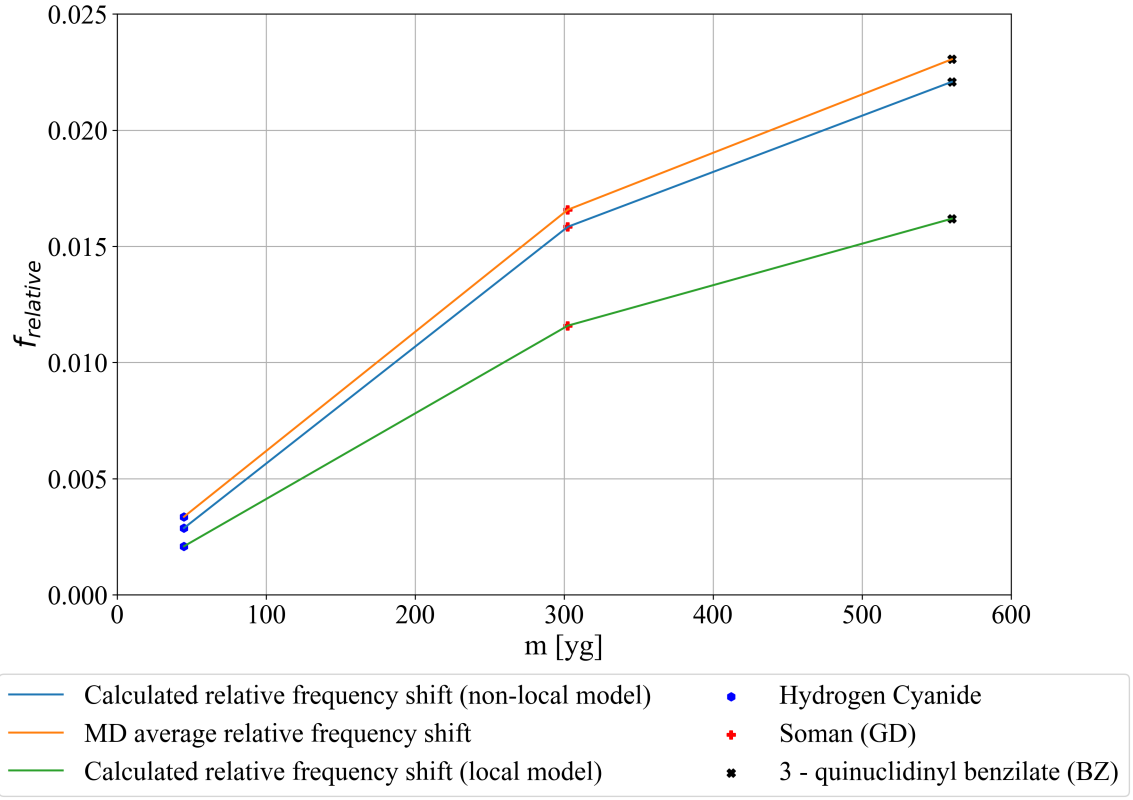

Figure 7.7: The comparison of calculated relative frequency shift with average relative frequency shift obtained using MD simulations for gas/vapor molecules attached at the center of SLGSB model with CCCC boundary condition.

Figs. 7.6, and 7.7 shows that the calculated absolute and relative frequency shift in which non-local parameter was obtained using Eq. (7.1) have a similar trend as the average absolute and relative frequency shift values obtained with MD simulations. However, the values of the calculated absolute and relative frequency shift values are on average 5 % lower than those obtained using MD simulations. It should be noted that the absolute and relative frequency shift values obtained using the non-local plate theory with the non-local parameter value of 0 nm have the same trend as in the case of the SLGSA model with CCCC boundary condition.

8. Conclusions and Further Research

8.1 Conclusions

In this thesis, the idea was to investigate the possibility of the implementation of graphene sheets as a sensing element for the detection of gas molecules using MD simulation and non-local theory of elasticity in combination with the theory of thin plates. For the purposes of MD simulations, SLGSA and SLGSB models were created using VMD software. In order to investigate if SLGS could detect gas molecules using the frequency shift method, it was necessary to obtain mechanical and thermodynamic properties at different temperatures. The sensing capabilities of the SLGS model were investigated at the temperature of 313.15 K. All molecules that were used in these investigations and at the previously mentioned temperature are in the gas/vapor form. The mechanical and thermodynamic parameters were obtained using REBO interatomic potential. The use of non-local theory was to obtain frequency equations that could be used to determine the natural frequencies for different cases of SLGSA and SLGSB model. Since the main disadvantage of this theory is unknown value of the non-local parameter the frequencies obtained using non-local theory were adjusted to those obtained using MD simulations. Based on that adjustment the dataset was created which was used in the Genetic Programming algorithm to obtain the symbolic expression for determining the non-local parameter. Based on the hypothesis mentioned in the introduction and results obtained in later chapters the following conclusions can be drawn:

- The investigation of mechanical parameters using MD showed that all mechanical parameters are temperature dependent and as the temperature increases the values of mechanical parameters such as E_{xx}, E_{yy} decreases from 1 to 0.9 TPa.
- The investigation of mechanical parameters showed that the tensile test in the direction of zigzag edge produced higher stress values than an armchair edge,
- The thermal expansion coefficient was negative due to shrinking of the graphene sheet during the equilibration simulations.

- The investigation of mechanical parameters and vibrations was initially performed on the SLGS structure with size 10×5 nm. The investigation of mechanical parameters did generate consistent results due to the fact that the simulation box was periodic in every direction and that the simulation walls coincided with the edges of graphene sheet. By performing MD simulations with such modification the mechanical parameters of infinite graphene sheet were obtained. However, such a small model in vibration simulation generated natural frequencies in almost 100 GHz range. For this reason, the model was omitted from further investigations and only models with sizes 20×10, 30×15 and 40×20 nm were considered.

- The size of the graphene sheet is one of the key components that influence the vibration frequency. Since the frequencies reported in [32] are currently impossible to obtain using MD simulations due to the enormous size of the graphene sheet and calculation costs involved, the non-local theory showed that graphene sheet size used in this thesis can generate frequency in the MHz range. In the rest of the thesis, the default size of SLGSA and SLGSB models was 20×10 nm in order to reduce computation time.

- The pressure in MD simulation showed large fluctuations even in the application of Nose-Hover barostat (NPT ensemble). Thus it was difficult to differentiate between 0 and 1 bar, so the influence of pressure was omitted from further investigation. However, in the non-local theory, the atmospheric pressure has negligible impact on natural frequencies.

- The utilization of the GP algorithm showed that artificial intelligence can provide new solutions to specific problems. In this case, the symbolic expression is obtained which can be used to calculate the value of the non-local parameter using mechanical parameters at different temperatures, the geometry of the structure, and natural frequencies obtained using MD simulations. In order to generate a more general symbolic expression, a larger dataset is required which will be created in further investigations.

- The investigation showed that the value of the non-local parameter is temperature dependent. As the the temperature increases the value of the non-local parameter also increases. This observation is in accordance with the results presented in [157].

8.2 Further research

Based on the research conducted in this doctoral dissertation, future research will be focused on:

- examination of the influence of the attached molecule position, and the number of molecules on natural vibrations of graphene sheet,
- examination of non-linear vibrations of the graphene sheet,
- examination of the influence of temperature, pressure, dimensions, different interatomic potentials on the mechanical and thermodynamic characteristics of single-layer and multi-layer graphene,
- examination of the influence of temperature, pressure, dimensions, different interatomic potentials, boundary conditions and the method of excitation on the natural frequencies of single-layer and multilayer graphene, and
- creating the larger dataset using MD simulations and the non-local theory in order to obtain the general symbolic expression for determining the non-local parameter value with higher accuracy.

Besides the investigation of the non-local parameter equation, the investigation will also be focused on the interaction between gas/vapor molecules and sensing elements (SLGS) using MD and the non-local theory.

Acknowledgment

This research has been (partly) supported by the CEEPUS network CIII-HR-0108, European Regional Development Fund under the grant KK.01.1.1.01.0009 (DATACROSS), project CEKOM under the grant KK.01.2.2.03.0004, CEI project COVIDAi (305.6019-20), project Metalska jezgra Čakovec (KK.01.1.1.02.0023), University of Rijeka scientific grant uniri-tehnic-18-275-1447, Croatian Science Foundation under the project IP-2019-04-4703 and University of Rijeka under the project number uniri-technic 18-37.

Bibliography

[1] Rudolf Peierls. Quelques propriétés typiques des corps solides. In *Annales de l'institut Henri Poincaré*, volume 5, pages 177–222, 1935.

[2] LD Landau. Zur Theorie der Phasenumwandlungen ii. *Phys. Z. Sowjet union*, 11(545):26–35, 1937.

[3] LD Landau and EM Lifshitz. Statistical physics, part 1: Volume 5 (course of theoretical physics, volume 5). *Publisher: Butterworth-Heinemann*, 3, 1980.

[4] JA Venables and GDT Spiller. Nucleation and growth of thin films. In *Surface Mobilities on Solid Materials*, pages 341–404. Springer, 1983.

[5] JW Evans, PA Thiel, and Maria C Bartelt. Morphological evolution during epitaxial thin film growth: Formation of 2d islands and 3d mounds. *Surface Science Reports*, 61(1-2):1–128, 2006.

[6] Kostya S Novoselov, Andre K Geim, Sergei V Morozov, D Jiang, Y_ Zhang, Sergey V Dubonos, Irina V Grigorieva, and Alexandr A Firsov. Electric field effect in atomically thin carbon films. *science*, 306(5696):666–669, 2004.

[7] KI Bolotin, KJ Sikes, J Hone, HL Stormer, and Ph Kim. Temperature-dependent transport in suspended graphene. *Physical review letters*, 101(9):096802, 2008.

[8] Alexander A Balandin, Suchismita Ghosh, Wenzhong Bao, Irene Calizo, Desalegne Teweldebrhan, Feng Miao, and Chun Ning Lau. Superior thermal conductivity of single-layer graphene. *Nano letters*, 8(3):902–907, 2008.

[9] Changgu Lee, Xiaoding Wei, Jeffrey W Kysar, and James Hone. Measurement of the elastic properties and intrinsic strength of monolayer graphene. *science*, 321(5887):385–388, 2008.

[10] F Schedin, AK Geim, SV Morozov, EW Hill, P Blake, MI Katsnelson, and KS Novoselov. Detection of individual gas molecules adsorbed on graphene. *Nature materials*, 6(9):652, 2007.

[11] RB Heimann, SE Evsyukov, and Y Koga. Carbon allotropes: a suggested classification scheme based on valence orbital hybridization. *Carbon*, 35(10-11):1654–1658, 1997.

[12] Andrey N Enyashin and Alexander L Ivanovskii. Graphene allotropes. *physica status solidi (b)*, 248(8):1879–1883, 2011.

[13] Ihsan Boustani. New quasi-planar surfaces of bare boron. *Surface science*, 370(2-3):355–363, 1997.

[14] Zhuhua Zhang, Yang Yang, Guoying Gao, and Boris I Yakobson. Two-dimensional boron monolayers mediated by metal substrates. *Angewandte Chemie International Edition*, 54(44):13022–13026, 2015.

[15] Andrew J Mannix, Xiang-Feng Zhou, Brian Kiraly, Joshua D Wood, Diego Alducin, Benjamin D Myers, Xiaolong Liu, Brandon L Fisher, Ulises Santiago, Jeffrey R Guest, et al. Synthesis of borophenes: Anisotropic, two-dimensional boron polymorphs. *Science*, 350(6267):1513–1516, 2015.

[16] Baojie Feng, Jin Zhang, Qing Zhong, Wenbin Li, Shuai Li, Hui Li, Peng Cheng, Sheng Meng, Lan Chen, and Kehui Wu. Experimental realization of two-dimensional boron sheets. *Nature chemistry*, 8(6):563, 2016.

[17] Pantelis Bampoulis, Lijie Zhang, A Safaei, Raoul van Gastel, Bene Poelsema, and H J W Zandvliet. Germanene termination of ge2pt crystals on ge110. *Journal of physics: Condensed matter*, 26(44):442001, 2014.

[18] Junji Yuhara, Hiroki Shimazu, Kouichi Ito, Akio Ohta, Masaaki Araidai, Masashi Kurosawa, Masashi Nakatake, and Guy Le Lay. Germanene epitaxial growth by segregation through ag111 thin films on ge111. *ACS nano*, 12(11):11632–11637, 2018.

[19] Kangho Lee, Hye-Young Kim, Mustafa Lotya, Jonathan N Coleman, Gyu-Tae Kim, and Georg S Duesberg. Electrical characteristics of molybdenum disulfide flakes produced by liquid exfoliation. *Advanced materials*, 23(36):4178–4182, 2011.

[20] Bernard Aufray, Abdelkader Kara, Sébastien Vizzini, Hamid Oughaddou, Christel Léandri, Benedicte Ealet, and Guy Le Lay. Graphene-like silicon nanoribbons on ag110: A possible formation of silicene. *Applied Physics Letters*, 96(18):183102, 2010.

[21] Boubekeur Lalmi, Hamid Oughaddou, Hanna Enriquez, Abdelkader Kara, Sébastien Vizzini, Bénidicte Ealet, and Bernard Aufray. Epitaxial growth of a silicene sheet. *Applied Physics Letters*, 97(22):223109, 2010.

[22] Antonis N Andriotis, Ernst Richter, and Madhu Menon. Prediction of a new graphenelike si 2 bn solid. *Physical Review B*, 93(8):081413, 2016.

[23] Junji Yuhara, Yuya Fujii, Kazuki Nishino, Naoki Isobe, Masashi Nakatake, Lede Xian, Angel Rubio, and Guy Le Lay. Large area planar stanene epitaxially grown on ag111. *2D Materials*, 5(2):025002, 2018.

[24] Likai Li, Yijun Yu, Guo Jun Ye, Qingqin Ge, Xuedong Ou, Hua Wu, Donglai Feng, Xian Hui Chen, and Yuanbo Zhang. Black phosphorus field-effect transistors. *Nature nanotechnology*, 9(5):372, 2014.

[25] Shengli Zhang, Zhong Yan, Yafei Li, Zhongfang Chen, and Haibo Zeng. Atomically thin arsenene and antimonene: semimetal–semiconductor and indirect–direct band-gap transitions. *Angewandte Chemie International Edition*, 54(10):3112–3115, 2015.

[26] Pablo Ares, Fernando Aguilar-Galindo, David Rodríguez-San-Miguel, Diego A Aldave, Sergio Díaz-Tendero, Manuel Alcamí, Fernando Martín, Julio Gómez-Herrero, and Félix Zamora. Mechanical isolation of highly stable antimonene under ambient conditions. *Advanced Materials*, 28(30):6332–6336, 2016.

[27] Pablo Ares, Juan José Palacios, Gonzalo Abellán, Julio Gómez-Herrero, and Félix Zamora. Recent progress on antimonene: a new bidimensional material. *Advanced Materials*, 30(2):1703771, 2018.

[28] Kin Fai Mak, Changgu Lee, James Hone, Jie Shan, and Tony F Heinz. Atomically thin mos 2: a new direct-gap semiconductor. *Physical review letters*, 105(13):136805, 2010.

[29] Lu Hua Li and Ying Chen. Atomically thin boron nitride: unique properties and applications. *Advanced Functional Materials*, 26(16):2594–2608, 2016.

[30] Seba S Varghese, Sunil Lonkar, KK Singh, Sundaram Swaminathan, and Ahmed Abdala. Recent advances in graphene based gas sensors. *Sensors and Actuators B: Chemical*, 218:160–183, 2015.

[31] Changyao Chen and James Hone. Graphene nanoelectromechanical systems. *Proceedings of the IEEE*, 101(7):1766–1779, 2013.

[32] J Scott Bunch, Arend M Van Der Zande, Scott S Verbridge, Ian W Frank, David M Tanenbaum, Jeevak M Parpia, Harold G Craighead, and Paul L McEuen. Electromechanical resonators from graphene sheets. *Science*, 315(5811):490–493, 2007.

[33] Arend M van der Zande, Robert A Barton, Jonathan S Alden, Carlos S Ruiz-Vargas, William S Whitney, Phi HQ Pham, Jiwoong Park, Jeevak M Parpia, Harold G Craighead, and Paul L McEuen. Large-scale arrays of single-layer graphene resonators. *Nano letters*, 10(12):4869–4873, 2010.

[34] Simone Pisana, Patrick M. Braganca, Ernesto E. Marinero, and Bruce A. Gurney. Tunable nanoscale graphene magnetometers. *Nano Letters*, 10(1):341–346, 2010.

[35] King Wai Chiu Lai, Ning Xi, Hongzhi Chen, Bo Song, and LiangLiang Chen. The development of an infrared camera using graphene: Achieving efficient high-resolution infrared images. *IEEE Nanotechnology Magazine*, 6(1):4–7, 2012.

[36] J. Scott Bunch, Scott S. Verbridge, Jonathan S. Alden, Arend M. van der Zande, Jeevak M. Parpia, Harold G. Craighead, and Paul L. McEuen. Impermeable atomic membranes from graphene sheets. *Nano Letters*, 8(8):2458–2462, 2008.

[37] Md WK Nomani, Razib Shishir, Muhammad Qazi, Devendra Diwan, VB Shields, MG Spencer, Gary S Tompa, Nick M Sbrockey, and Goutam Koley. Highly sensitive and selective detection of no2 using epitaxial graphene on 6h-sic. *Sensors and Actuators B: Chemical*, 150(1):301–307, 2010.

[38] Jack Chan, Archana Venugopal, Adam Pirkle, Stephen McDonnell, David Hinojos, Carl W Magnuson, Rodney S Ruoff, Luigi Colombo, Robert M Wallace, and Eric M Vogel. Reducing extrinsic performance-limiting factors in graphene grown by chemical vapor deposition. *ACS nano*, 6(4):3224–3229, 2012.

[39] AK Singh, MA Uddin, JT Tolson, H Maire-Afeli, N Sbrockey, GS Tompa, MG Spencer, T Vogt, TS Sudarshan, and G Koley. Electrically tunable molecular doping of graphene. *Applied Physics Letters*, 102(4):043101, 2013.

[40] Md.W.K. Nomani, Razib Shishir, Muhammad Qazi, Devendra Diwan, V.B. Shields, M.G. Spencer, Gary S. Tompa, Nick M. Sbrockey, and Goutam Koley. Highly sensitive and selective detection of no2 using epitaxial graphene on 6h-sic. *Sensors and Actuators B: Chemical*, 150(1):301 – 307, 2010.

[41] Md. W. K. Nomani, V. Shields, G. Tompa, N. Sbrockey, M. G. Spencer, R. A. Webb, and G. Koley. Correlated conductivity and work function changes in epitaxial graphene. *Applied Physics Letters*, 100(9):092113, 2012.

[42] Muhammad Qazi, Mohammad W. K. Nomani, M. V. S. Chandrashekhar, Virgil B. Shields, Michael G. Spencer, and Goutam Koley. Molecular adsorption behavior of epitaxial graphene grown on 6h-SiC faces. *Applied Physics Express*, 3(7):075101, jul 2010.

[43] Sergey Rumyantsev, Guanxiong Liu, Michael S. Shur, Radislav A. Potyrailo, and Alexander A. Balandin. Selective gas sensing with a single pristine graphene transistor. *Nano Letters*, 12(5):2294–2298, 2012.

[44] Priscilla Kailian Ang, Wei Chen, Andrew Thye Shen Wee, and Kian Ping Loh. Solution-gated epitaxial graphene as ph sensor. *Journal of the American Chemical Society*, 130(44):14392–14393, 2008.

[45] Tao Zhang, Zengguang Cheng, Yibing Wang, Zhongjun Li, Chenxuan Wang, Yibao Li, and Ying Fang. Self-assembled 1-octadecanethiol monolayers on graphene for mercury detection. *Nano letters*, 10(11):4738–4741, 2010.

[46] Huifeng Xu, Hong Dai, and Guonan Chen. Direct electrochemistry and electrocatalysis of hemoglobin protein entrapped in graphene and chitosan composite film. *Talanta*, 81(1-2):334–338, 2010.

[47] Xinhuang Kang, Jun Wang, Hong Wu, Ilhan A Aksay, Jun Liu, and Yuehe Lin. Glucose oxidase–graphene–chitosan modified electrode for direct electrochemistry and glucose sensing. *Biosensors and Bioelectronics*, 25(4):901–905, 2009.

[48] Ke-Jing Huang, De-Jun Niu, Jun-Yong Sun, Cong-Hui Han, Zhi-Wei Wu, Yan-Li Li, and Xiao-Qin Xiong. Novel electrochemical sensor based on functionalized graphene for simultaneous determination of adenine and guanine in dna. *Colloids and Surfaces B: Biointerfaces*, 82(2):543–549, 2011.

[49] Qin Wei, Kexia Mao, Dan Wu, Yuxue Dai, Jian Yang, Bin Du, Minghui Yang, and He Li. A novel label-free electrochemical immunosensor based on graphene and thionine nanocomposite. *Sensors and Actuators B: Chemical*, 149(1):314–318, 2010.

[50] Ying Wang, Yueming Li, Longhua Tang, Jin Lu, and Jinghong Li. Application of graphene-modified electrode for selective detection of dopamine. *Electrochemistry Communications*, 11(4):889–892, 2009.

[51] Ramendra Sundar Dey and C Retna Raj. Development of an amperometric cholesterol biosensor based on graphene- pt nanoparticle hybrid material. *The Journal of Physical Chemistry C*, 114(49):21427–21433, 2010.

[52] F. Schedin, A. K. Geim, S. V. Morozov, E. W. Hill, P. Blake, M. I. Katsnelson, and K. S. Novoselov. Detection of individual gas molecules adsorbed on graphene. *Nature Materials*, 6(9):652–655, 2007.

[53] Yaping Dan, Ye Lu, Nicholas J Kybert, Zhengtang Luo, and AT Charlie Johnson. Intrinsic response of graphene vapor sensors. *Nano letters*, 9(4):1472–1475, 2009.

[54] G Ko, H-Y Kim, J Ahn, Y-M Park, K-Y Lee, and J Kim. Graphene-based nitrogen dioxide gas sensors. *Current Applied Physics*, 10(4):1002–1004, 2010.

[55] Gugang Chen, Tereza M Paronyan, and Avetik R Harutyunyan. Sub-ppt gas detection with pristine graphene. *Applied Physics Letters*, 101(5):053119, 2012.

[56] Sergey Rumyantsev, Guanxiong Liu, Michael S Shur, Radislav A Potyrailo, and Alexander A Balandin. Selective gas sensing with a single pristine graphene transistor. *Nano letters*, 12(5):2294–2298, 2012.

[57] KR Nemade and SA Waghuley. Chemiresistive gas sensing by few-layered graphene. *Journal of electronic materials*, 42(10):2857–2866, 2013.

[58] Shishir Kumar, Swati Kaushik, Rudra Pratap, and Srinivasan Raghavan. Graphene on paper: A simple, low-cost chemical sensing platform. *ACS applied materials & interfaces*, 7(4):2189–2194, 2015.

[59] Stefano Prezioso, Francesco Perrozzi, Luca Giancaterini, Carlo Cantalini, Emanuele Treossi, Vincenzo Palermo, Michele Nardone, Sandro Santucci, and Luca Ottaviano. Graphene oxide as a practical solution to high sensitivity gas sensing. *The Journal of Physical Chemistry C*, 117(20):10683–10690, 2013.

[60] Jianwei Wang, Budhi Singh, Jin-Hyung Park, Servin Rathi, In-yeal Lee, Sunglyul Maeng, Han-Ik Joh, Cheol-Ho Lee, and Gil-Ho Kim. Dielectrophoresis of graphene oxide nanostructures for hydrogen gas sensor at room temperature. *Sensors and Actuators B: Chemical*, 194:296–302, 2014.

[61] S. Drewniak, T. Pustelny, M. Setkiewicz, E. Maciak, M. Urbańczyk, M. Procek, Z. Opilski, J. Jagiello, and L. Lipinska. Investigations of saw structures with oxide graphene layer to detection of selected gases. *Acta Physica Polonica A*, 124(3):402–405, 2013.

[62] T. Pustelny, S. Drewniak, M. Setkiewicz, E. Maciak, M. Urbańczyk, M. Procek, K. Gut, Z. Opilski, J. Jagiello, L. Lipinska, and et al. The sensitivity of sensor structures with oxide graphene exposed to selected gaseous atmospheres. *Bulletin of the Polish Academy of Sciences: Technical Sciences*, 61(3):705–710, 2013.

[63] Surajit Some, Yang Xu, Youngmin Kim, Yeoheung Yoon, Hongyi Qin, Atul Kulkarni, Taesung Kim, and Hyoyoung Lee. Highly sensitive and selective gas sensor using hydrophilic and hydrophobic graphenes. *Scientific Reports*, 3(1), 2013.

[64] Jeremy T. Robinson, F. Keith Perkins, Eric S. Snow, Zhongqing Wei, and Paul E. Sheehan. Reduced graphene oxide molecular sensors. *Nano Letters*, 8(10):3137–3140, 2008.

[65] Jesse D. Fowler, Matthew J. Allen, Vincent C. Tung, Yang Yang, Richard B. Kaner, and Bruce H. Weiller. Practical chemical sensors from chemically derived graphene. *ACS Nano*, 3(2):301–306, 2009.

[66] Jukka Hassinen, Jussi Kauppila, Jarkko Leiro, Anni Määttänen, Petri Ihalainen, Jouko Peltonen, and Jukka Lukkari. Low-cost reduced graphene oxide-based conductometric nitrogen dioxide-sensitive sensor on paper. *Analytical and Bioanalytical Chemistry*, 405(11):3611–3617, 2013.

[67] Jianwei Wang, Budhi Singh, Sunglyul Maeng, Han-Ik Joh, and Gil-Ho Kim. Assembly of thermally reduced graphene oxide nanostructures by alternating current dielectrophoresis as hydrogen-gas sensors. *Applied Physics Letters*, 103(8):083112, 2013.

[68] Jianwei Wang, Youngreal Kwak, In-Yeal Lee, Sunglyul Maeng, and Gil-Ho Kim. Highly responsive hydrogen gas sensing by partially reduced graphite oxide thin films at room temperature. *Carbon*, 50(11):4061–4067, 2012.

[69] Le-Sheng Zhang, Wei D. Wang, Xian-Qing Liang, Wang-Sheng Chu, Wei-Guo Song, Wei Wang, and Zi-Yu Wu. Characterization of partially reduced graphene oxide as room temperature sensor for h2. *Nanoscale*, 3(6):2458, 2011.

[70] TO Wehling, KS Novoselov, SV Morozov, EE Vdovin, MI Katsnelson, AK Geim, and AI Lichtenstein. Molecular doping of graphene. *Nano letters*, 8(1):173–177, 2008.

[71] O Leenaerts, B Partoens, and FM Peeters. Adsorption of h 2 o, n h 3, co, n o 2, and no on graphene: A first-principles study. *Physical Review B*, 77(12):125416, 2008.

[72] M Darvish Ganji, SM Hosseini-Khah, and Z Amini-Tabar. Theoretical insight into hydrogen adsorption onto graphene: a first-principles b3lyp-d3 study. *Physical Chemistry Chemical Physics*, 17(4):2504–2511, 2015.

[73] Zheyuan Chen, Pierre Darancet, Lei Wang, Andrew C Crowther, Yuanda Gao, Cory R Dean, Takashi Taniguchi, Kenji Watanabe, James Hone, Chris A Marianetti, et al. Physical adsorption and charge transfer of molecular br2 on graphene. *ACS nano*, 8(3):2943–2950, 2014.

[74] Kun-Joon Lee and Seung-Joon Kim. Theoretical investigation of co 2 adsorption on graphene. *Bulletin of the Korean Chemical Society*, 34(10):3022–3026, 2013.

[75] Bing Huang, Zuanyi Li, Zhirong Liu, Gang Zhou, Shaogang Hao, Jian Wu, Bing-Lin Gu, and Wenhui Duan. Adsorption of gas molecules on graphene nanoribbons and its implication for nanoscale molecule sensor. *The Journal of Physical Chemistry C*, 112(35):13442–13446, 2008.

[76] Jiayu Dai, Jianmin Yuan, and Paolo Giannozzi. Gas adsorption on graphene doped with b, n, al, and s: a theoretical study. *Applied Physics Letters*, 95(23):232105, 2009.

[77] Hong-ping Zhang, Xue-gang Luo, Xiao-yang Lin, Xiong Lu, Yang Leng, and Hong-tao Song. Density functional theory calculations on the adsorption of formaldehyde and other harmful gases on pure, ti-doped, or n-doped graphene sheets. *Applied surface science*, 283:559–565, 2013.

[78] Behrouz Arash, Quan Wang, and Wen Hui Duan. Detection of gas atoms via vibration of graphenes. *Physics Letters A*, 375(24):2411–2415, 2011.

[79] Behrouz Arash and Quan Wang. Detection of gas atoms with graphene sheets. *Computational Materials Science*, 60:245–249, 2012.

[80] Jin-Wu Jiang, Harold S Park, and Timon Rabczuk. Enhancing the mass sensitivity of graphene nanoresonators via nonlinear oscillations: the effective strain mechanism. *Nanotechnology*, 23(47):475501, 2012.

[81] S. Kamal Jalali, M. Hassan Naei, and Nicola Maria Pugno. Graphene-based resonant sensors for detection of ultra-fine nanoparticles: Molecular dynamics and nonlocal elasticity investigations. *Nano*, 10(02):1550024, 2015.

[82] Wu Qin, Xin Li, Wen-Wen Bian, Xiu-Juan Fan, and Jing-Yao Qi. Density functional theory calculations and molecular dynamics simulations of the adsorption of biomolecules on graphene surfaces. *Biomaterials*, 31(5):1007–1016, 2010.

[83] Toshiaki Natsuki, Jin-Xing Shi, and Qing-Qing Ni. Vibration analysis of nanomechanical mass sensor using double-layered graphene sheets resonators. *Journal of Applied Physics*, 114(9):094307, 2013.

[84] Toshiaki Natsuki. Theoretical analysis of vibration frequency of graphene sheets used as nanomechanical mass sensor. *Electronics*, 4(4):723–738, 2015.

[85] SC Pradhan and JK Phadikar. Nonlocal elasticity theory for vibration of nanoplates. *Journal of Sound and Vibration*, 325(1-2):206–223, 2009.

[86] H. P. Boehm, R. Setton, and E. Stumpp. Nomenclature and terminology of graphite intercalation compounds (iupac recommendations 1994). *Pure and Applied Chemistry*, 66(9):1893–1901, 1994.

[87] Hans-Peter Boehm, A Clauss, GO Fischer, and U Hofmann. Das adsorptionsverhalten sehr dünner kohlenstoff-folien. *Zeitschrift für anorganische und allgemeine Chemie*, 316(3-4):119–127, 1962.

[88] Andre Konstantin Geim. Graphene: status and prospects. *science*, 324(5934):1530–1534, 2009.

[89] Daniel R Cooper, Benjamin D'Anjou, Nageswara Ghattamaneni, Benjamin Harack, Michael Hilke, Alexandre Horth, Norberto Majlis, Mathieu Massicotte, Leron Vandsburger, Eric Whiteway, et al. Experimental review of graphene. *ISRN Condensed Matter Physics*, 2012, 2012.

[90] SM-M Dubois, Zeila Zanolli, Xavier Declerck, and J-C Charlier. Electronic properties and quantum transport in graphene-based nanostructures. *The European Physical Journal B*, 72(1):1–24, 2009.

[91] Qiang Cao, Xiao Geng, Huaipeng Wang, Pengjie Wang, Aaron Liu, Yucheng Lan, and Qing Peng. A review of current development of graphene mechanics. *Crystals*, 8(9):357, 2018.

[92] Haider I Rasool, Colin Ophus, William S Klug, A Zettl, and James K Gimzewski. Measurement of the intrinsic strength of crystalline and polycrystalline graphene. *Nature communications*, 4:2811, 2013.

[93] Peng Zhang, Lulu Ma, Feifei Fan, Zhi Zeng, Cheng Peng, Phillip E Loya, Zheng Liu, Yongji Gong, Jiangnan Zhang, Xingxiang Zhang, et al. Fracture toughness of graphene. *Nature communications*, 5:3782, 2014.

[94] Konstantin N Kudin, Gustavo E Scuseria, and Boris I Yakobson. C 2 f, bn, and c nanoshell elasticity from ab initio computations. *Physical Review B*, 64(23):235406, 2001.

[95] Fang Liu, Pingbing Ming, and Ju Li. Ab initio calculation of ideal strength and phonon instability of graphene under tension. *Physical Review B*, 76(6):064120, 2007.

[96] Jian-Gang Guo, Li-Jun Zhou, and Yi-Lan Kang. Chirality-dependent anisotropic elastic properties of a monolayer graphene nanosheet. *Journal of nanoscience and nanotechnology*, 12(4):3159–3164, 2012.

[97] G Kalosakas, NN Lathiotakis, C Galiotis, and K Papagelis. In-plane force fields and elastic properties of graphene. *Journal of Applied Physics*, 113(13):134307, 2013.

[98] Dongshan Wei, Yang Song, and Feng Wang. A simple molecular mechanics potential for μm scale graphene simulations from the adaptive force matching method. *The Journal of chemical physics*, 134(18):184704, 2011.

[99] Huijuan Zhao, K Min, and Narayana R Aluru. Size and chirality dependent elastic properties of graphene nanoribbons under uniaxial tension. *Nano letters*, 9(8):3012–3015, 2009.

[100] Bin Zhang, Lanjv Mei, and Haifeng Xiao. Nanofracture in graphene under complex mechanical stresses. *Applied Physics Letters*, 101(12):121915, 2012.

[101] Pavol Lengvarskỳ and Jozef Bocko. Prediction of youngs modulus of graphene sheets by the finite element method. *American Journal of Mechanical Engineering*, 3(6):225–229, 2015.

[102] A Sakhaee-Pour. Elastic properties of single-layered graphene sheet. *Solid State Communications*, 149(1-2):91–95, 2009.

[103] Yu-Kuei Yeh and Chyanbin Hwu. A modified molecular-continuum model for estimating the strength and fracture toughness of graphene and carbon nanotube. *Engineering Fracture Mechanics*, 176:326–342, 2017.

[104] Xiao Liu, Thomas H Metcalf, Jeremy T Robinson, Brian H Houston, and Fabrizio Scarpa. Shear modulus of monolayer graphene prepared by chemical vapor deposition. *Nano letters*, 12(2):1013–1017, 2012.

[105] Yujie Wei, Baoling Wang, Jiangtao Wu, Ronggui Yang, and Martin L Dunn. Bending rigidity and gaussian bending stiffness of single-layered graphene. *Nano letters*, 13(1):26–30, 2012.

[106] Tarek Ragab, Julia McDonald, and Cemal Basaran. Aspect ratio effect on shear modulus and ultimate shear strength of graphene nanoribbons. *Diamond and Related Materials*, 74:9–15, 2017.

[107] K Min and Narayana R Aluru. Mechanical properties of graphene under shear deformation. *Applied Physics Letters*, 98(1):013113, 2011.

[108] Q Wang. Simulations of the bending rigidity of graphene. *Physics Letters A*, 374(9):1180–1183, 2010.

[109] JH Los, A Fasolino, and MI Katsnelson. Scaling behavior and strain dependence of in-plane elastic properties of graphene. *Physical review letters*, 116(1):015901, 2016.

[110] Jin-Wu Jiang, Tienchong Chang, Xingming Guo, and Harold S Park. Intrinsic negative poisson's ratio for single-layer graphene. *Nano letters*, 16(8):5286–5290, 2016.

[111] Binghui Deng, Jie Hou, Hanxing Zhu, Sheng Liu, Emily Liu, Yunfeng Shi, and Qing Peng. The normal-auxeticity mechanical phase transition in graphene. *2D Materials*, 4(2):021020, 2017.

[112] Ch Androulidakis, G Tsoukleri, N Koutroumanis, G Gkikas, P Pappas, J Parthenios, K Papagelis, and C Galiotis. Experimentally derived axial stress–strain relations for two-dimensional materials such as monolayer graphene. *Carbon*, 81:322–328, 2015.

[113] Georgia Tsoukleri, John Parthenios, Konstantinos Papagelis, Rashid Jalil, Andrea C Ferrari, Andre K Geim, Kostya S Novoselov, and Costas Galiotis. Subjecting a graphene monolayer to tension and compression. *small*, 5(21):2397–2402, 2009.

[114] SC Pradhan. Buckling of single layer graphene sheet based on nonlocal elasticity and higher order shear deformation theory. *Physics Letters A*, 373(45):4182–4188, 2009.

[115] SC Pradhan and T Murmu. Small scale effect on the buckling of single-layered graphene sheets under biaxial compression via nonlocal continuum mechanics. *Computational materials science*, 47(1):268–274, 2009.

[116] Marko Canadija, Marino Brcic, and Josip Brnic. Bending behaviour of single-layered graphene nanosheets with vacancy defects. *Engineering Review*, 33(1):9–14, 2013.

[117] Ömer Civalek. Elastic buckling behavior of skew shaped single-layer graphene sheets. *Thin Solid Films*, 550:450–458, 2014.

[118] Makoto Ashino and Roland Wiesendanger. Atomic-site-specific analysis on out-of-plane elasticity of convexly curved graphene and its relationship to sp 2 to sp 3 re-hybridization. *Crystals*, 8(2):102, 2018.

[119] Maria JB Moura and Michael Marder. Tearing of free-standing graphene. *Physical Review E*, 88(3):032405, 2013.

[120] Jihoon Han, Seunghwa Ryu, and Dongwoo Sohn. A feasibility study on the fracture strength measurement of polycrystalline graphene using nanoindentation with a cylindrical indenter. *Carbon*, 107:310–318, 2016.

[121] KV Zakharchenko, MI Katsnelson, and Annalisa Fasolino. Finite temperature lattice properties of graphene beyond the quasiharmonic approximation. *Physical review letters*, 102(4):046808, 2009.

[122] Jia-Lin Tsai and Jie-Feng Tu. Characterizing mechanical properties of graphite using molecular dynamics simulation. *Materials & Design*, 31(1):194–199, 2010.

[123] David Halpern, Howard B Wilson, and Louis H Turcotte. *Advanced mathematics and mechanics applications using MATLAB*. Chapman and Hall/CRC, 2002.

[124] Hongwei Zhang, Zhengrong Guo, Hong Gao, and Tienchong Chang. Stiffness-dependent interlayer friction of graphene. *Carbon*, 94:60–66, 2015.

[125] Yang Cheng, Pengzhe Zhu, and Rui Li. The influence of vertical vibration on nanoscale friction: A molecular dynamics simulation study. *Crystals*, 8(3):129, 2018.

[126] A Sakhaee-Pour, MT Ahmadian, and R Naghdabadi. Vibrational analysis of single-layered graphene sheets. *Nanotechnology*, 19(8):085702, 2008.

[127] K Hashemnia, M Farid, and R Vatankhah. Vibrational analysis of carbon nanotubes and graphene sheets using molecular structural mechanics approach. *Computational Materials Science*, 47(1):79–85, 2009.

[128] M Sadeghi and R Naghdabadi. Nonlinear vibrational analysis of single-layer graphene sheets. *Nanotechnology*, 21(10):105705, 2010.

[129] SS Gupta and RC Batra. Elastic properties and frequencies of free vibrations of single-layer graphene sheets. *Journal of Computational and Theoretical Nanoscience*, 7(10):2151–2164, 2010.

[130] R Ansari, S Sahmani, and B Arash. Nonlocal plate model for free vibrations of single-layered graphene sheets. *Physics Letters A*, 375(1):53–62, 2010.

[131] Fabrizio Scarpa, Rajib Chowdhury, Kenneth Kam, Sondipon Adhikari, and Massimo Ruzzene. Dynamics of mechanical waves in periodic graphene nanoribbon assemblies. *Nanoscale research letters*, 6(1):430, 2011.

[132] Jaber Rezaei Mianroodi, Sina Amini Niaki, Reza Naghdabadi, and Mohsen Asghari. Nonlinear membrane model for large amplitude vibration of single layer graphene sheets. *Nanotechnology*, 22(30):305703, 2011.

[133] R Chowdhury, S Adhikari, F Scarpa, and MI Friswell. Transverse vibration of single-layer graphene sheets. *Journal of Physics D: Applied Physics*, 44(20):205401, 2011.

[134] Bekir Akgöz and Ömer Civalek. Free vibration analysis for single-layered graphene sheets in an elastic matrix via modified couple stress theory. *Materials & Design*, 42:164–171, 2012.

[135] Cengiz Baykasoglu and Ata Mugan. Dynamic analysis of single-layer graphene sheets. *Computational Materials Science*, 55:228–236, 2012.

[136] VV Alyokhin, BD Annin, AV Babichev, and SN Korobeynikov. Free vibrations and buckling of graphene sheets. In *Doklady Physics*, volume 58, pages 487–490. Springer, 2013.

[137] Mina Mirparizi and FarshadShakeri Aski. Interlayer shear effect on vibrational behavior of bilayer graphene using the molecular mechanics simulation. *Propulsion and Power Research*, 5(3):250–260, 2016.

[138] Georg Kresse and Jürgen Furthmüller. Efficient iterative schemes for ab initio total-energy calculations using a plane-wave basis set. *Physical review B*, 54(16):11169, 1996.

[139] Huijuan Zhao and Narayana R Aluru. Temperature and strain-rate dependent fracture strength of graphene. *Journal of Applied Physics*, 108(6):064321, 2010.

[140] K Ganesan, SK Raza, and R Vijayaraghavan. Chemical warfare agents. *Journal of pharmacy and bioallied sciences*, 2(3):166, 2010.

[141] Daan Frenkel and Berend Smit. *Understanding molecular simulation: from algorithms to applications*, volume 1. Elsevier, 2001.

[142] Richard LeSar. *Introduction to computational materials science: fundamentals to applications*. Cambridge University Press, 2013.

[143] Donald W Brenner. The art and science of an analytic potential. *physica status solidi (b)*, 217(1):23–40, 2000.

[144] Kholmirzo Kholmurodov, Ermuhammad Dushanov, Kenji Yasuoka, Hagar Khalil, Ahmed Galal, Sameh Ahmed, Nasser Sweilam, and Hatem Moharram. Molecular dynamics simulation of the interaction of ethanol-water mixture with a pt surface. *Natural Science*, 3(12):1011, 2011.

[145] Jerry Tersoff. New empirical approach for the structure and energy of covalent systems. *Physical Review B*, 37(12):6991, 1988.

[146] GC Abell. Empirical chemical pseudopotential theory of molecular and metallic bonding. *Physical Review B*, 31(10):6184, 1985.

[147] Donald W Brenner. Empirical potential for hydrocarbons for use in simulating the chemical vapor deposition of diamond films. *Physical review B*, 42(15):9458, 1990.

[148] Donald W Brenner. Erratum: Empirical potential for hydrocarbons for use in simulating the chemical vapor deposition of diamond films. *Physical Review B*, 46(3):1948, 1992.

[149] Donald W Brenner, Olga A Shenderova, Judith A Harrison, Steven J Stuart, Boris Ni, and Susan B Sinnott. A second-generation reactive empirical bond order (rebo) potential energy expression for hydrocarbons. *Journal of Physics: Condensed Matter*, 14(4):783, 2002.

[150] Danilo Karlicic, Tony Murmu, Sondipon Adhikari, and Michael McCarthy. *Non-local structural mechanics*. John Wiley & Sons, 2015.

[151] A Cemal Eringen. On differential equations of nonlocal elasticity and solutions of screw dislocation and surface waves. *Journal of applied physics*, 54(9):4703–4710, 1983.

[152] Lifeng Wang and Haiyan Hu. Flexural wave propagation in single-walled carbon nanotubes. *Physical Review B*, 71(19):195412, 2005.

[153] WH Duan and Chien Ming Wang. Exact solutions for axisymmetric bending of micro/nanoscale circular plates based on nonlocal plate theory. *Nanotechnology*, 18(38):385704, 2007.

[154] WH Duan, Chien Ming Wang, and YY Zhang. Calibration of nonlocal scaling effect parameter for free vibration of carbon nanotubes by molecular dynamics. *Journal of applied physics*, 101(2):024305, 2007.

[155] Quan Wang, QK Han, and BC Wen. Estimate of material property of carbon nanotubes via nonlocal elasticity. *Adv. Theor. Appl. Mech*, 1(1):1–10, 2008.

[156] Q Wang and CM Wang. The constitutive relation and small scale parameter of nonlocal continuum mechanics for modelling carbon nanotubes. *Nanotechnology*, 18(7):075702, 2007.

[157] S Ahmad Fazelzadeh and Esmaeal Ghavanloo. Nanoscale mass sensing based on vibration of single-layered graphene sheet in thermal environments. *Acta Mechanica Sinica*, 30(1):84–91, 2014.

[158] Nikola Anđelić, Zlatan Car, and Marko Čanađija. Nems resonators for detection of chemical warfare agents based on graphene sheet. *Mathematical Problems in Engineering*, 2019, 2019.

[159] Raffaele Barretta, Marino Brčić, Marko Čanađija, Raimondo Luciano, and Francesco Marotti de Sciarra. Application of gradient elasticity to armchair carbon nanotubes: Size effects and constitutive parameters assessment. *European Journal of Mechanics-A/Solids*, 65:1–13, 2017.

[160] Pin Lu, HP Lee, C Lu, and PQ Zhang. Dynamic properties of flexural beams using a nonlocal elasticity model. *Journal of applied physics*, 99(7):073510, 2006.

[161] S Graham Kelly. *Mechanical vibrations: theory and applications*. Cengage learning Stamford, USA, 2012.

[162] Riccardo Poli, William B Langdon, Nicholas F McPhee, and John R Koza. *A field guide to genetic programming*. Lulu. com, 2008.

[163] Eric W Weisstein. *CRC concise encyclopedia of mathematics*. CRC press, 2002.

[164] John R Koza and John R Koza. *Genetic programming: on the programming of computers by means of natural selection*, volume 1. MIT press, 1992.

[165] Introduction to genetic programming algorithm in python programming language.

[166] Seyyedeh Newsha Ghoreishi, Anders Clausen, and Bo Nørregaard Jørgensen. Termination criteria in evolutionary algorithms: A survey. In *IJCCI*, pages 373–384, 2017.

[167] Steve Plimpton. Fast parallel algorithms for short-range molecular dynamics. *Journal of computational physics*, 117(1):1–19, 1995.

[168] William Humphrey, Andrew Dalke, and Klaus Schulten. VMD: visual molecular dynamics. *Journal of molecular graphics*, 14(1):33–38, 1996.

[169] Marcus D Hanwell, Donald E Curtis, David C Lonie, Tim Vandermeersch, Eva Zurek, and Geoffrey R Hutchison. Avogadro: an advanced semantic chemical editor, visualization, and analysis platform. *Journal of cheminformatics*, 4(1):17, 2012.

[170] Large-scale atomic,molecular massively parallel simulator (LAMMPS) version 24th december documentation.

[171] KGS Dilrukshi, MAN Dewapriya, and UGA Puswewala. Size dependency and potential field influence on deriving mechanical properties of carbon nanotubes using molecular dynamics. *Theoretical and Applied Mechanics Letters*, 5(4):167–172, 2015.

[172] OA Shenderova, DW Brenner, A Omeltchenko, X Su, and LH Yang. Atomistic modeling of the fracture of polycrystalline diamond. *Physical Review B*, 61(6):3877, 2000.

[173] Hamid Ghasemi and Ali Rajabpour. Thermal expansion coefficient of graphene using molecular dynamics simulation: A comparative study on potential functions. In *Journal of Physics: Conference Series*, volume 785, page 012006. IOP Publishing, 2017.

[174] Xing Xiao, Shang-Chun Fan, Cheng Li, and Wei-Wei Xing. Stress-insensitive resonant graphene mass sensing via frequency ratio. *Sensors*, 19(13):3027, 2019.

[175] Reza Ansari, Saeed Rouhi, and Ayoub Shahnazari. Vibrational analysis of single-walled carbon nanotube/graphene junctions using finite element modeling. *The European Physical Journal Applied Physics*, 76(2):20402, 2016.

List of Figures

List of Tables

List of Symbols

Latin letters:

A	-	graphene sheet surface
A_{mn}	-	vibration amplitude
a	-	distance between two carbon atoms
C_{klmn}	-	elastic modulus tensor
$D_{11}, D_{12}, D_{66}, D_{22}$	-	bending rigidity coefficients
G_{xy}	-	shear modulus
E_{xx}	-	elastic modulus in x direction
E_{yy}	-	elastic modulus in y direction
E_{ij}^{LJ}	-	energy of Lennard -Jones potential
$E_{ij}^{TORSION}$	-	energy of Torsion potential
$e_0 a$	-	non-local parameter
$f_A(r_{ij})$	-	attractive force
$f_C(r_{ij})$	-	cutoff radius function
f_{mnCCCC}	-	frequency of SLGS with CCCC boundary condition
$f_{mnCCCCT}$	-	frequency of SLGS with CCCC boundary condition (temperature influence)
$f_{mnCCCCPT}$	-	frequency of SLGS with CCCC boundary condition (pressure and temperature influence)
$f_{mnCCCCPTAM}$	-	frequency of SLGS with CCCC boundary condition (influence of pressure, temperature and attached nanoparticle mass)
f_l	-	body force density
$f_R(r_{ij})$	-	repulsive force
Δf	-	absolute frequency shift
$f_{relative}$	-	relative frequency shift

$G(\theta_{ijk})$	-	function of angles between bonds of atoms $i-j$ and $i-k$
h	-	thickness of graphene sheet
L_0	-	linear differential operator
L_a	-	length of graphene sheet along x axis
L_b	-	length of graphene sheet along y axis
m_j	-	nanoparticle mass
m	-	mode shape number
n	-	mode shape number
N_i^C	-	number of carbon atoms
N_{ij}^{conj}	-	number of bonds between carbon atoms i and j are part of conjugated system
N_i^H	-	number of hydrogen atoms
N_i^t	-	total number of neighbors of atom i
N_{xx}^T	-	thermal resultant force due to temperature difference in x direction
N_{yy}^T	-	thermal resultant force due to temperature difference in y direction
P_{atm}	-	atmospheric pressure
T	-	temperature
$q(x,y,t)$	-	transverse force per unit area
$\left\|sp_1^2\right\rangle, \left\|sp_2^2\right\rangle, \left\|sp_3^2\right\rangle$	-	three quantum mechanical states
u_l, u_k	-	displacement vectors at a reference point x
$V_A(r_{ij})$	-	attractive function
$V_R(r_{ij})$	-	repulsive function
$W(x,y)$	-	mode shape function

Greek letters:

α	-	number of atoms in the system
$\alpha(\lvert\mathbf{x}-\mathbf{x}'\rvert,\xi)$	-	influencing kernel function or non-local modulus
α_x	-	thermal expansion coefficient in x direction
α_y	-	thermal expansion coefficient in y direction
γ_0	-	nearest-neighbor hopping energy
$\delta_1, \delta_2, \delta_3$	-	three vectors that connect sublattice A to sublattice B
$\delta(x-x_j, y-y_j)$	-	Dirac delta function
ε	-	depth of the potential well
ε_{kl}	-	classical strain
η	-	non-dimensional parameter for molecule position
λ	-	first Lame parameter
μ	-	second Lame parameter
ν_{xy}, ν_{yx}	-	Poisson's coefficients
ξ	-	non-dimensional parameter for molecule position
ρ	-	mass density
σ	-	distance at which potential well is zero
σ_{kl}	-	classical stress
σ_{kl}^c	-	non-local stress
σ_{xx}	-	stress in x direction
σ_{yy}	-	stress in y direction
σ_{xy}	-	shear stress
ω_{mn}	-	general variable of circular frequency

List of Abbreviations

AA	-	ascorbic acid
AFM	-	atomic force microscopy
AFP	-	anti-alpha-fetoprotein
AI	-	artificial intelligence
BZ	-	3 - qinucldinyl benzilate
CCCC	-	completely clamped boundary condtion
chem-FETs	-	chemical field-effect transistors
CVD	-	chemical vapor deposition
CX	-	dichloroformoxime
DFT	-	density functional theory
DFT	-	Discrete Fourier Transform
DMMP	-	dymethyl methyl phosphonate
DNA	-	deoxyribonucleic acid
DNT	-	2,4-dinitrotoulene
FFT	-	Fast Fourier Transform
GD	-	soman
GO	-	graphene oxide
GP	-	genetic programming
HCN	-	hydrogen cyanide
IQ	-	Integral quadrature method
IR	-	Infra red
LA	-	logitudinal acoustic mode
LAMMPS	-	Large-scale Atomic/Molecular Massively Parallel Simulator
LJ	-	Lennard Jonnes
LPG	-	liquified petrolium gas

MD	-	molecular dynamics
NEMS	-	Nano electro mechanical sensor
NP	-	nano particles
PG	-	pristine graphene
PS	-	pseudo-spectral
REBO	-	Reactive Empirical Bond Order interatomic potential
RGO	-	reduce graphene oxide
SAW	-	surface acoustic waves
SLGS	-	single layer graphene sheet
TA	-	transverse acoustic mode
UA	-	uric acid
VMD	-	Visual Molecular Dynamics

Appendices

A. LAMMPS MD Codes

A.1 Mechanical Parameters obtained using MD simulation

In this section the Python script is shown that are used to generate LAMMPS scripts equilibration scripts at certain temperature and pressure. After Python equilibration script generator the example of LAMMPS equilibration script is shown. Then the Python script for generating LAMMPS uniaxal in X, Y direction and shear test at specific temperature and pressure is shown. After the Python script the example of LAMMPS scripts for performing uniaxal test in X, Y and shear test are shown.

A.1.1 Example of LAMMPS equilibration script

```
1       log       log.equilSLGSAREBO233150
2       units      metal
3       dimension     3
4       boundary     p p p
5       atom_style     atomic
6       newton      on
7       read_data     SLGSA10X5.data
8       pair_style     rebo
9       pair_coeff     * * CH.rebo C
10      shell      mkdir EquilSLGS_A_REBO_233.15_0_
11      shell      cd EquilSLGS_A_REBO_233.15_0_
12      reset_timestep    0
13      timestep     0.001
14      compute      1 all stress/atom NULL
15      compute      2 all reduce sum c_1[1] c_1[2]
16      variable     Lx equal lx
17      variable     Ly equal ly
```

```
18        variable     Lz equal lz
19        variable     Vol equal vol
20        variable     thickn equal 3.4
21        fix       1 all npt temp 233.15 233.15 $(100*dt) x 0 0 0.5 y 0 0
             0.5 drag 1
22        thermo      1000
23        thermo_style    custom step temp lx ly lz pe etotal press vol
24        dump      1 all atom 10000 equil*.lammpstrj
25        run       1000000
26        unfix      1
27        undump      1
28        shell      cd ..
29        write_restart    restart.equilSLGSAREBO233150
```

A.1.2 Example of LAMMPS input script for uniaxial test in X direction

```
1  log        log.UniXDirSLGSAREBO2331501
2  read_restart     restart.equilSLGSAREBO233150
3  variable      ts equal 0.001
4  compute       1 all stress/atom NULL
5  compute       2 all reduce sum c_1[1] c_1[2]
6  variable      tmp1 equal "lx"
7  variable      L0x equal ${tmp1}
8  variable      tmp2 equal "ly"
9  variable      L0y equal ${tmp2}
10 variable      Lx equal lx
11 variable      Ly equal ly
12 variable      Lz equal lz
13 variable      Vol equal vol
14 variable      thickn equal 6.8
15 pair_style      rebo
16 pair_coeff      * * CH.rebo C
17 shell       mkdir DeformXSLGSAREBO233150_1
18 shell       cd DeformXSLGSAREBO233150_1
19 reset_timestep     0
20 timestep      0.001
21 fix        1 all npt temp 233.15 233.15 $(100*dt) y 0 0 0.5
```

```
22 fix        2 all ave/time 1 100 100 c_2[1] c_2[2]
23 fix        3 all ave/time 1 100 100 v_Lx v_Ly v_Lz v_Vol
24 variable      srate equal 10e9
25 variable      srate1 equal "v_srate/10e12"
26 fix        4 all deform 1 x erate ${srate1} units box remap x
27 run        100
28 variable      CorVol equal f_3[4]*v_thickn/(f_3[3])
29 variable      ConvoFac equal 1/1.0e4
30 variable      sigmaxx equal f_2[1]*v_ConvoFac/v_CorVol
31 variable      sigmayy equal f_2[2]*v_ConvoFac/v_CorVol
32 variable      StrainPerTs equal v_srate1*v_ts
33 variable      strainx equal v_StrainPerTs*step
34 variable      strain22 equal "(ly - v_L0y)/v_L0y"
35 variable      strainy equal ${strain22}
36 variable      nuxy equal "-v_strainy/v_strainx"
37 thermo       1000
38 thermo_style     custom step temp v_strainx v_sigmaxx v_strainy v_sigmayy
       v_nuxy pe ke ly ly vol
39 fix        def1 all print 100 "${strainx} ${strainy} ${nuxy} ${sigmaxx} $
      {sigmayy}" file Uni_X_DirSLGS_A_REBO_233.15_0_1.data screen no
40 dump       1 all atom 1000 TTDLGS_A_REBO_233.15_0_1*.lammpstrj
41 run        300000
42 shell       cd ..
43 print       "Tensile Test SLGS_A_REBO_233.15_0_1 in X Direction Done !!!"
```

A.1.3 Example of LAMMPS input script for uniaxail test in Y direction

```
1  log        log.UniYDirSLGSAREBO2331501
2  read_restart     restart.equilSLGSAREBO233150
3  variable      ts equal 0.001
4  compute       1 all stress/atom NULL
5  compute       2 all reduce sum c_1[1] c_1[2]
6  variable      tmp1 equal "lx"
7  variable      L0x equal ${tmp1}
8  print       "Initial length in x direction, L0x: ${L0x}"
9  variable      tmp2 equal "ly"
10 variable      L0y equal ${tmp2}
```

```
print       "Initial length in y direction, L0y: ${L0y}"
variable      Lx equal lx
variable      Ly equal ly
variable      Lz equal lz
variable      Vol equal vol
variable      thickn equal 3.4
pair_style      rebo
pair_coeff      * * CH.rebo C
shell       mkdir DeformYSLGSAREBO233150_1
shell       cd DeformYDLGSAREBO233150_1
reset_timestep     0
timestep      0.001
fix         1 all npt temp 233.15 233.15 $(100*dt) x 0 0 0.5
fix         2 all ave/time 1 100 100 c_2[1] c_2[2]
fix         3 all ave/time 1 100 100 v_Lx v_Ly v_Lz v_Vol
variable      srate equal 10e9
variable      srate1 equal "v_srate/10e12"
fix         4 all deform 1 y erate ${srate1} units box remap x
run         100
variable      CorVol equal f_3[4]*v_thickn/(f_3[3])
variable      ConvoFac equal 1/1.0e4
variable      sigmaxx equal f_2[1]*v_ConvoFac/v_CorVol
variable      sigmayy equal f_2[2]*v_ConvoFac/v_CorVol
variable      StrainPerTs equal v_srate1*v_ts
variable      strainy equal v_StrainPerTs*step
variable     strain11 equal "(lx - v_L0x)/v_L0x"
variable      strainx equal ${strain11}
variable      nuxy equal "-v_strainy/v_strainx"
thermo       1000
thermo_style     custom step temp v_strainx v_sigmaxx v_strainy v_sigmayy
    v_nuxy pe ke ly ly vol
fix         def1 all print 100 "${strainx} ${strainy} ${nuxy} ${sigmaxx} $
   {sigmayy}" file Uni_Y_DirDLGS_A_REBO_233.15_0_1.data screen no
dump        1 all atom 1000 TTDLGS_A_REBO_233.15_0_1*.lammpstrj
run         300000
shell        cd ..
print       "Tensile Test SLGS_A_REBO_233.15_0_1 in Y Direction Done !!!"
```

A.1.4 Example of LAMMPS input script for shear test (XY)

```
log        log.ShearSLGSAREBO2331501
read_restart     restart.equilSLGSAREBO233150
change_box      all triclinic
variable      ts equal 0.001
compute       1 all stress/atom NULL
compute       2 all reduce sum c_1[4]
variable      Lx equal lx
variable      Ly equal ly
variable      Lz equal lz
variable      Vol equal vol
variable      thickn equal 6.8
pair_style      rebo
pair_coeff      * * CH.rebo C
shell       mkdir SHEARXYSLGSAREBO233150_1
shell       cd SHEARXYSLGSAREBO233150_1
reset_timestep     0
timestep      0.001
fix        1 all npt temp 233.15 233.15 $(100*dt) x 0 0 0.5 y 0 0 0.5
fix        2 all ave/time 1 100 100 c_2
fix        3 all ave/time 1 100 100 v_Lx v_Ly v_Lz v_Vol
variable      srate equal 10e9
variable      srate1 equal "v_srate/1.0e12"
fix        4 all deform 1 xy erate ${srate1} units box remap v
run        100
variable      CorVol equal f_3[4]*v_thickn/(f_3[3])
variable      ConvoFac equal 1/1.0e4
variable      sigmaxy equal f_2*v_ConvoFac/v_CorVol
variable      StrainPerTs equal v_srate1*v_ts
variable      strain equal v_StrainPerTs*step
thermo       1000
thermo_style     custom step temp v_strain v_sigmaxy pe ke lx vol
fix        def1 all print 100 "${strain} ${sigmaxy}" file
   ShearXYDLGS_A_REBO_233.15_0_1.data screen no
dump       1 all atom 1000 sheardeftestDLGS_A_REBO_233.15_0_1*.lammpstrj
run        500000
shell       cd ..
```

```
print       "Shear deformation test DLGS_A_REBO_233.15_0_1 is DONE!!!"
```

A.2 Natural Frequencies obtained using MD simulations

In this section examples of LAMMPS input scripts are given for following investigations:

- influence of size on natural frequencies of SLGS model, and
- natural frequencies of SLGS model with attached gas molecule.

A.2.1 Influence of size on natural frequencies of SLGS model

```
log     log.vibCCCCSLGSAREBO20X102331501111vel
units    metal
dimension   3
boundary   f f f
atom_style   atomic
newton    on
read_data   SLGSAREBO20X10.data
variable   XLO equal xlo
variable   YLO equal ylo
variable   ZLO equal zlo
variable   XHI equal xhi
variable   YHI equal yhi
variable   ZHI equal zhi
variable   XLOB equal "2.86814"
variable   XHIB equal "194.11569"
variable   YLOB equal "3.82419"
variable   YHIB equal "97.64575"
variable   XLOGXMID equal "9.29617"
variable   XHIGXMID equal "187.18768"
variable   YLOGXMID equal "9.917"
variable   YHIGXMID equal "90.761"
print    "XLOB = ${XLOB}"
print    "XHIB = ${XHIB}"
print    "YLOB = ${YLOB}"
print    "YHIB = ${YHIB}"
```

```
region    rxlo block ${XLO} ${XLOB} ${YLO} ${YHI} ${ZLO} ${ZHI} units box
region    rxhi block ${XHIB} ${XHI} ${YLO} ${YHI} ${ZLO} ${ZHI} units box
region    rylo block ${XLOB} ${XHIB} ${YLO} ${YLOB} ${ZLO} ${ZHI} units
   box
region    ryhi block ${XLOB} ${XHIB} ${YHIB} ${YHI} ${ZLO} ${ZHI} units
   box
region    rxmid block ${XLOGXMID} ${XHIGXMID} ${YLOGXMID} ${YHIGXMID} ${
   ZLO} ${ZHI} units box
region    rcentral block 97.54192 98.94192 48.93 50.33 ${ZLO} ${ZHI}
   units box
group    gxlo region rxlo
group    gxhi region rxhi
group    gylo region rylo
group    gyhi region ryhi
group    boundary union gxlo gxhi gylo gyhi
group    gxmid subtract all boundary
group    gcentral region rcentral
variable   number equal count(gxmid)
print    "number of atoms = ${number}"
pair_style   rebo
pair_coeff   * * CH.rebo C
neigh_modify  every 1 delay 0 check yes
min_style   cg
thermo    100
thermo_style  custom step temp lx ly lz pe etotal press vol pxx pyy pzz
minimize   1.0e-10 1.0e-10 1000 100000
shell    mkdir EquilCCCCSLGSAREBO20X102331501111vel
shell    cd EquilCCCCSLGSAREBO20X102331501111vel
reset_timestep  0
timestep   0.001
fix     1 boundary setforce 0 0 0
velocity   gxmid create 233.15 949028 rot yes dist gaussian
fix     5 all nvt temp 233.15 233.15 $(100*dt)
thermo    10000
thermo_style  custom step temp lx ly lz pe etotal press vol pxx pyy pzz
dump    1 all atom 1000 equilinCCCCSLGSAREBO20X102331501111vel*.lammpstrj
run     100000
```

```
unfix    5
undump    1
shell    cd ..
write_restart        restart.equilinCCCCSLGSAREBO20X102331501111vel
shell    mkdir VelCCCCSLGSAREBO20X102331501111
shell    cd VelCCCCSLGSAREBO20X102331501111
reset_timestep  0
timestep   0.001
compute    1 all displace/atom
compute    2 all reduce ave c_1[3]
compute    3 all vacf
variable    vzz atom (cos((2*1*PI*x)/(${XHI}-${XLO}))-1)*(cos((2*1*PI*y)
   /(${YHI}-${YLO}))-1)
velocity    gxmid set NULL NULL v_vzz sum yes units box
fix     5 all nve
fix     7 all ave/time 1 1 1 c_3[1] c_3[2] c_3[3] c_3[4] file
   vcafvelCCCCSLGSAREBO20X102331501111.data
variable   DACZ equal c_2
fix     8 all print 1 "${DACZ}" file dispVelCCCCSLGSAREBO20X102331501111.
   data screen no
variable   VACZ equal c_3[3]
variable   VACF equal c_3[4]
fix     9 all print 1 "${VACZ} ${VACF}" file
   vacfVelCCCCSLGSAREBO20X102331501111.data screen no
dump    2 all atom 1000 vibSLGSAREBO20X102331501111vel*.lammpstrj
thermo    1000
thermo_style  custom step temp ke pe etotal lx ly lz vol press pxx pyy
   pzz v_DACZ
run     200000
shell    cd ..
write_restart  restart.CCCCSLGSAREBO20X102331501111
undump    2
unfix    5
unfix    7
unfix    8
unfix    9
reset_timestep  0
```

```
timestep   0.001
shell    mkdir FreeCCCCSLGSAREBO20X102331501111
shell    cd FreeCCCCSLGSAREBO20X102331501111
fix     5 all nve
fix     7 all ave/time 1 1 1 c_3[1] c_3[2] c_3[3] c_3[4] file
   vcafvelCCCCSLGSAREBO20X102331501111.data
fix     8 all print 1 "${DACZ}" file dispFREECCCCSLGSAREBO20X102331501111
   .data screen no
fix     9 all print 1 "${VACZ} ${VACF}" file
   vacfFREECCCCSLGSAREBO20X102331501111.data screen no
dump    1 all atom 10000 deform*.lammpstrj
thermo    100
thermo_style  custom step temp ke pe etotal lx ly lz vol press pxx pyy
   pzz v_DACZ
run     1000000
shell    cd ..
print    "Simulation is done!!!"
print     "Vibration Simulation Script in.CCCC_SLGS_A_REBO_20X10_233.15
   _0_1_1_1_1_vel is done!!!"
```

A.2.2 Natural frequencies of SLGS model with attached gas molecule

```
log     log.vibCCCCSLGSAREBO3131503BZ1111vel
units    metal
dimension   3
boundary   f f f
atom_style   atomic
newton    on
read_data   SLGSA20x101.data
mass    1 12.010700
mass    2 337.42
variable   XLO equal xlo
variable   YLO equal ylo
variable   ZLO equal zlo
variable   XHI equal xhi
variable   YHI equal yhi
variable   ZHI equal zhi
variable   XLOB equal "2.86814"
```

```
17 variable   XHIB equal "194.11569"
18 variable   YLOB equal "3.82419"
19 variable   YHIB equal "97.64575"
20 variable   XLOGXMID equal "9.29617"
21 variable   XHIGXMID equal "187.18768"
22 variable   YLOGXMID equal "9.917"
23 variable   YHIGXMID equal "90.761"
24 region    rxlo block ${XLO} ${XLOB} ${YLO} ${YHI} ${ZLO} ${ZHI} units box
25 region    rxhi block ${XHIB} ${XHI} ${YLO} ${YHI} ${ZLO} ${ZHI} units box
26 region    rylo block ${XLOB} ${XHIB} ${YLO} ${YLOB} ${ZLO} ${ZHI} units
      box
27 region    ryhi block ${XLOB} ${XHIB} ${YHIB} ${YHI} ${ZLO} ${ZHI} units
      box
28 group    gxlo region rxlo
29 group    gxhi region rxhi
30 group    gylo region rylo
31 group    gyhi region ryhi
32 group    boundary union gxlo gxhi gylo gyhi
33 group    gcentral id 7873
34 group    gxmid subtract all boundary gcentral
35 group    plate union gxmid boundary
36 variable   number equal count(gxmid)
37 print    "number of atoms = ${number}"
38 pair_style   rebo
39 pair_coeff   * * CH.rebo C C
40 neigh_modify  every 1 delay 0 check yes
41 min_style   cg
42 thermo    100
43 thermo_style  custom step temp lx ly lz pe etotal press vol pxx pyy pzz
44 minimize   1.0e-10 1.0e-10 1000 100000
45 shell    mkdir EquilCCCCSLGSAREBO3131503BZ1111vel
46 shell    cd EquilCCCCSLGSAREBO3131503BZ1111vel
47 reset_timestep  0
48 timestep   0.001
49 fix     1 boundary setforce 0 0 0
50 fix     2 gcentral move linear 0 0 NULL units box
51 velocity   gxmid create 313.15 123456 rot yes dist gaussian
```

```
52 fix     5 plate nvt temp 313.15 313.15 $(100*dt)
53 thermo    1000
54 thermo_style  custom step temp lx ly lz pe etotal press vol pxx pyy pzz
55 dump    1 all atom 1000 equilinCCCCSLGSAREBO3131503BZ1111vel*.lammpstrj
56 run     100000
57 unfix    5
58 undump    1
59 shell    cd ..
60 write_restart  restart.equilinCCCCSLGSAREBO3131503BZ1111vel
61 shell    mkdir VelCCCCSLGSAREBO3131503BZ1111
62 shell    cd VelCCCCSLGSAREBO3131503BZ1111
63 reset_timestep  0
64 timestep   0.001
65 compute    1 all displace/atom
66 compute    2 all reduce ave c_1[3]
67 compute    3 all vacf
68 variable    vzz atom (cos((2*1*PI*x)/(${XHI}-${XLO}))-1)*(cos((2*1*PI*y)
      /(${YHI}-${YLO}))-1)
69 velocity    gxmid set NULL NULL v_vzz sum yes units box
70 fix     6 plate nve
71 fix     7 all ave/time 1 1 1 c_3[1] c_3[2] c_3[3] c_3[4] file
      vcafvelCCCCSLGSAREBO3131503BZ1111.data
72 variable   DACZ equal c_2
73 fix     8 all print 1 "${DACZ}" file dispVelCCCCSLGSAREBO3131503BZ1111.
      data screen no
74 variable   VACZ equal c_3[3]
75 variable   VACF equal c_3[4]
76 fix     9 all print 1 "${VACZ} ${VACF}" file
      vacfVelCCCCSLGSAREBO3131503BZ1111.data screen no
77 dump    2 all atom 1000 vibSLGSAREBO3131503BZ1111vel*.lammpstrj
78 thermo    1000
79 thermo_style  custom step temp ke pe etotal lx ly lz vol press pxx pyy
      pzz v_DACZ
80 run     200000
81 shell    cd ..
82 write_restart  restart.CCCCSLGSAREBO3131503BZ1111
83 undump    2
```

```
84 unfix    6
85 unfix    7
86 unfix    8
87 unfix    9
88 reset_timestep  0
89 timestep   0.001
90 shell    mkdir FreeCCCCSLGSAREBO3131503BZ1111
91 shell    cd FreeCCCCSLGSAREBO3131503BZ1111
92 fix     6 plate nve
93 fix     7 all ave/time 1 1 1 c_3[1] c_3[2] c_3[3] c_3[4] file
      vcafvelCCCCSLGSAREBO3131503BZ1111.data
94 fix     8 all print 1 "${DACZ}" file dispFREECCCCSLGSAREBO3131503BZ1111.
      data screen no
95 fix     9 all print 1 "${VACZ} ${VACF}" file
      vacfFREECCCCSLGSAREBO3131503BZ1111.data screen no
96 dump    1 all atom 1000 deform*.lammpstrj
97 thermo    100
98 thermo_style  custom step temp ke pe etotal lx ly lz vol press pxx pyy
      pzz v_DACZ
99 run     1000000
100 shell    cd ..
101 print    "Simulation is done!!!"
102 print     "Vibration Simulation Script in.CCCC_SLGS_A_REBO_313.15
      _0_3BZ_1_1_1_1_vel is done!!!"
```

B. Python Codes - Genetic Programming Algorithm

Listing B.1: The Genetic Programming Algorithm used to obtained symbolic expression of non-local parameter

```
import inspect
import random
import pandas as pd
import numpy as np
from datetime import datetime
from sklearn.model_selection import train_test_split
from sklearn import metrics
from sklearn.tree import DecisionTreeRegressor
from sklearn.ensemble import RandomForestRegressor
from sklearn.utils import check_random_state
import gplearn.genetic
# Extracting data for GP analysis
df = pd.read_csv(r'DATA2.csv')
Temp = df["Temperature"].tolist();Frekvencija = df["Frequency MD"].tolist
    ()
Exx = df["Exx"].tolist();Eyy = df["Eyy"].tolist();Gxy = df["Gxy"].tolist
    ()
nuxy = df["nuxy"].tolist();La = df["LA "].tolist();Lb = df["Lb "].tolist
    ()
e0a = df["e0a"].tolist()
trainLen = int(0.8*len(Frekvencija))
TempTrain = Temp[:trainLen];TempTest = Temp[trainLen:]
FrekTrain = Frekvencija[:trainLen];FrekTest = Frekvencija[trainLen:]
ExxTrain = Exx[:trainLen]; ExxTest = Exx[trainLen:]
EyyTrain = Eyy[:trainLen]; EyyTest = Eyy[trainLen:]
```

```
GxyTrain = Gxy[:trainLen]; GxyTest = Gxy[trainLen:]
nuxyTrain = nuxy[:trainLen]; nuxyTest = nuxy[trainLen:]
LaTrain = La[:trainLen]; LaTest = La[trainLen:]
LbTrain = Lb[:trainLen]; LbTest = Lb[trainLen:]
# X Train list X Test List
X_train_list = [];X_test_list = []
for i in range(len(FrekTrain)):
    X_train_list.append(TempTrain[i]);X_train_list.append(FrekTrain[i])
    X_train_list.append(ExxTrain[i]);X_train_list.append(EyyTrain[i])
    X_train_list.append(GxyTrain[i]);X_train_list.append(nuxyTrain[i])
    X_train_list.append(LaTrain[i]);X_train_list.append(LbTrain[i])
for i in range(len(FrekTrain)):
    X_test_list.append(TempTest[i]);X_test_list.append(FrekTest[i])
    X_test_list.append(ExxTest[i]);X_test_list.append(EyyTest[i])
        X_test_list.append(GxyTest[i]);X_test_list.append(nuxyTest[i])
    X_test_list.append(LaTest[i]);X_test_list.append(LbTest[i])
X_train = np.asanyarray(X_train_list).reshape(trainLen,8)
X_test = np.asanyarray(X_test_list).reshape(len(TempTest),8)
# Y Train List Y Test List
y_train = e0a[:trainLen];y_test = e0a[trainLen:]
def GeneticProgramming(genes,X_train,Y_train, X_test, Y_test):
    est_gp = gplearn.genetic.SymbolicRegressor(population_size = genes
        [0],\
        generations = genes[1],tournament_size = genes[2],\
    init_depth = genes[3],p_crossover = genes[4],\
    p_subtree_mutation= genes[5],p_hoist_mutation= genes[6],\
    p_point_mutation= genes[7],stopping_criteria = genes[8],\
    max_samples = genes[9], const_range=genes[10],\
    parsimony_coefficient = genes[11],verbose = True,\
    function_set = ('add','sub', 'mul','div','sqrt','abs','log","max",\
                                    "min","sin","cos","tan"))
    est_gp.fit(X_train, Y_train)
    score1 = est_gp.score(X_test,Y_test)
    return str(est_gp._program), score1
k = 0
while True:
    parentGPParameters = generateGPParameters()
```

```
59      program = []
60      try:
61          x1,xsc = GeneticProgramming(parentGPParameters,\
62          X_train,y_train,X_test,y_test)
63          program.append(x1)
64          cleanFormula = []
65          x2 = processingFormulas(program)
66          cleanFormula.append(x2[0])
67          x3 = Calculation(cleanFormula, X_test, y_test)
68          k += 1
69          if xsc > 0.9:
70              if xsc > 0.999:
71                  break
72      except (MemoryError, ZeroDivisionError):
73          parentGPParameters[:] = [];program[:] = []
74          cleanFormula[:] = []
75          continue
```

Circulum Vitae

Nikola Anđelić mag. ing. mech. was born was born March 6th 1988 in Rijeka, Croatia. He received Mag. ing. mech. title in 2012. at Faculty of Engineering Rijeka. That same year he enrolled in Postgraduate doctoral study in engineering sciences, module Computational Mechanics at Faculty of Engineering Rijeka. From 2008 – 2009 he had worked for Alpron company as a CAD designer on isolation panels, handling systems and inox conveyers. In 2012-2013 he had worked at Thermotechnik company as CAD designer on manifolds, stations with floor heating, stations with radiator heating, stations with combine heating. From 2014-2016 he had worked on Faculty of Engineering Rijeka on ADRIA HUB European Project as Engineering Expert in Mechanical Design. The project dealt with investigation of cutting tools in woodworking industry. As of 2016 he's working as research/teaching assistant at Faculty of Engineering, University of Rijeka at Department of Automation and Electronics. He's PhD research is in a field of nanotechnology and artificial intelligence.

List of Publications

Scientific papers in peer-reviewed journals:

1. Anđelić, N., Šegota, S. B., Lorencin, I., Mrzljak, V., and Car, Z. (2021). Estimation of COVID-19 epidemic curves using genetic programming algorithm. *Health Informatics Journal*, 27(1), doi:10.1177/1460458220976728

2. Lorencin, I., Šegota, S. B., Anđelić, N., Blagojević, A., Šušteršić, T., Protić, A., Arsenijević, M., Ćabov, T., Filipović, N., and Car, Z. (2021). Automatic Evaluation of the Lung Condition of COVID-19 Patients Using X-ray Images and Convolutional Neural Networks. *Journal of Personalized Medicine*, 11(1), 28. doi: 10.3390/jpm11010028

3. Anđelić, N., Mrzljak, V., Lorencin, I., and Šegota, S. B. (2020). Comparison of Exergy and Various Energy Analysis Methods for a Main Marine Steam Turbine at Different Loads. *Pomorski zbornik*, 59(1), 9-34. doi: 18048/2020.59.01.

4. Anđelić, N., Šegota, S. B., Lorencin, I., Car, Z. (2020). Estimation of gas turbine shaft torque and fuel flow of a CODLAG propulsion system using genetic programming algorithm. *Pomorstvo*, 34(2), 323-337. doi: 10.31217/p.34.2.13

5. Šegota, S. B., Lorencin, I., Anđelić, N., Mrzljak, V., and Car, Z. (2020). Improvement of Marine Steam Turbine Conventional Exergy Analysis by Neural Network Application. *Journal of Marine Science and Engineering*, 8(11), 884. doi: 10.3390/jmse8110884

6. Medica-Viola, V., Mrzljak, V., Anđelić, N., & Jelić, M. (2020). Analysis of Low-Power Steam Turbine With One Extraction for Marine Applications. *NAŠE MORE: znanstveni časopis za more i pomorstvo*, 67(2), 87-95. doi: 10.17818/NM/2020/2.1

7. Car, Z., Šegota, S. B., Anđelić, N., Lorencin, I., & Mrzljak, V. (2020). Modeling the Spread of COVID-19 Infection Using a Multilayer Perceptron. *Computational and Mathematical Methods in Medicine*, 2020. doi: 10.1155/2020/5714714

8. Šegota, S. B., Anđelić, N., Lorencin, I., Saga, M., and Car, Z. (2020). Path planning optimization of six-degree-of-freedom robotic manipulators using evolutionary algorithms. *International Journal of Advanced Robotic Systems*, 17(2), doi:10.1177/1729881420908076

9. Lorencin, I., Anđelić, N., Španjol, J., & Car, Z. (2020). Using multi-layer perceptron with Laplacian edge detector for bladder cancer diagnosis. *Artificial Intelligence in Medicine*, 102, 101746. doi: 10.1016/j.artmed.2019.101746

10. Šegota, S. B., Anđelić, N., Kudláček, J., and Čep, R. (2019). Artificial neural network for predicting values of residuary resistance per unit weight of displacement. *Pomorski zbornik*, 57(1), 9-22. doi: 10.18048/2019.57.01.

11. Mrzljak, V., Anđelić, N., Lorencin, I., and Car, Z. (2019). Analysis of Gas Turbine Operation before and after Major Maintenance. *Pomorski zbornik*, 57(1), 57-70. doi: 10.18048/2019.57.04.

12. Lorencin, I., Anđelić, N., Mrzljak, V., & Car, Z. (2019). Multilayer Perceptron approach to Condition-Based Maintenance of Marine CODLAG Propulsion System Components. *Pomorstvo*, 33(2), 181-190. doi: 10.31217/p.33.2.8

13. Lorencin, I., Anđelić, N., Mrzljak, V., & Car, Z. (2019). Genetic Algorithm Approach to Design of Multi-Layer Perceptron for Combined Cycle Power Plant Electrical Power Output Estimation. *Energies*, 12(22), 4352. doi: 10.3390/en12224352

14. Mrzljak, V., Blecich, P., Anđelić, N., & Lorencin, I. (2019). Energy and Exergy Analyses of Forced Draft Fan for Marine Steam Propulsion System during Load Change. *Journal of Marine Science and Engineering*, 7(11), 381. doi: 10.3390/jmse7110381

15. Lorencin, I., Anđelić, N., Mrzljak, V., & Car, Z. (2019). Marine Objects Recognition Using Convolutional Neural Networks. *NAŠE MORE: znanstveni časopis za more i pomorstvo*, 66(3), 112-119. doi: 10.17818/NM/2019/3.3

16. Mrzljak, V., Anđelić, N., Poljak, I., and Orović, J. (2019). Thermodynamic analysis of marine steam power plant pressure reduction valves. Pomorski zbornik, 56(1), 9-30. doi: 10.18048/2019.56.01

17. Lorencin, I., Anđelić, N., Mrzljak, V., & Car, Z. (2019). Exergy analysis of marine steam turbine labyrinth (gland) seals. *Pomorstvo*, 33(1), 76-83. doi: 10.31217/p.33.1.8

18. Anđelić, N., Car, Z., & Čanađija, M. (2019). NEMS Resonators for Detection of Chemical Warfare Agents Based on Graphene Sheet. *Mathematical Problems in Engineering*, 2019. doi:10.1155/2019/6451861

19. Blažević, S., Mrzljak, V., Anđelić, N., and Car, Z. (2019). Comparison Of Energy Flow Stream And Isentropic Method For Steam Turbine Energy Analysis. Acta Polytechnica, 59(2), 109-125. doi:10.14311/ap.2019.59.0109

20. Anđelić, N., Braut, S., & Pavlović, A. (2018). Variation of Natural Frequencies by Circular Saw Blade Rotation. *Tehnički vjesnik*, 25(1), 10-17. doi: 10.17559/TV-20160210110559

21. Skoblar, A., Andjelic, N., & Zigulic, R. (2016). Determination of critical rotational speed of circular saws from natural frequencies of annular plate with analogous dimensions. *International Journal for Quality Research*, 10(1). doi: 10.18421/IJQR10.01-09

22. Anđelić, N., Žigulić, R., & Čanađija, M. (2017). On the influence of thermal stresses on eigenvalues of a circular saw blade. *Proceedings of the Institution of Mechanical Engineers, Part C: Journal of Mechanical Engineering Science*, 231(1), 96-108. doi:10.1177/0954406216641148

Scientific papers in conferences:

1. Vedran, M., Ivan, L., Nikola, A., & Zlatan, C. (2020). Dual-flow dissymmetrical low pressure steam turbine energy analysis–comparison of both turbine cylinders. Machines. Technologies. Materials., 14(8), 336-339.

2. Vedran, M., Jasna, P. O., Vedran, M. V., & Nikola, A. (2020). The change in energy flow streams for main marine propulsion steam turbine at different loads. Trans Motauto World, 5(1), 26-29.

3. Mrzljak, V., Prpić-Oršić, J., Lorencin, I., & Anđelić, N. (2020). Thermodynamic analysis of three-cylinder steam turbine from combined cycle power plant. Machines. Technologies. Materials., 14(2), 61-64.

4. Anđelić, N., Čanađija, M., & Car, Z. NEMS resonator for detection of chemical warfare agents based on single layer graphene sheet.*International Conference on Innovative Technologies, IN-TECH 2019.*

5. Mrzljak, V., Orović, J., Poljak, I., & Anđelić, N. Exergy analysis of high-pressure feed water heating system at three power plant loads.*International Conference on Innovative Technologies, IN-TECH 2019.*

6. Anđelić, N., Lorencin, I., Mrzljak, V., & Car, Z. Friction modeling of robot manipulator joints. *International Conference on Innovative Technologies, IN-TECH 2019.*

7. Lorencin, I., Barišić, B., Anđelić, N., Španjol, J., & Car, Z. (2019). Comparison of Edge Detectors for Urinary Bladder Cancer Diagnostic. *International Conference on Innovative Technologies, IN-TECH 2019.*

8. Anđelić, N., Čanađija, M., & Car, Z. (2019, January). NEMS Resonator for detection of Chemical Warfare Agents based on Double Layer Graphene Sheet. In 9. susret Hrvatskog društva za mehaniku: 50 godina Društva.

9. Mrzljak, V., Žarković, B., Prpić-Oršić, J., & Anđelić, N. (2019, January). Numerical analysis of in-cylinder pressure and temperature change for naturally aspirated and upgraded gasoline engine. *In XXVII International scientific conference trans & Motoauto'19.*

10. Anđelić, N., Blažević, S., & Car, Z. (2018, January). Trajectory planning using genetic algorithm for three joints robot manipulator. *In International Conference on Innovative Technologies, IN-TECH 2018.*

11. Brnić, M., Čondrić, E., Blažević, S., Anđelić, N., Borović, E., & Car, Z. (2018, January). Sepsis prediction using artificial intelligence algorithms. *In International Conference on Innovative Technologies, IN-TECH 2018.*

12. Mrzljak, V., Blažević, S., Anđelić, N., & Car, Z. (2018, January). Exhaust gas emissions from turbocharged direct injection diesel engine during the fuel mass flow variation. *In International Conference on Innovative Technologies, IN-TECH 2018.*

13. Blažević, S., Anđelić, N., & Car, Z. (2017, January). Research of Unstable Behavior of Iterative Path Planning Algorithm for Robot Manipulator. *In IN-TECH 2017 International Conference on Innovative Technologies.*

14. Anđelić, N., Čanađija, M., & Car, Z. (2017, January). Determination of Natural Vibrations of Simply Supported Single Layer Graphene Sheet using Non-Local Kirchhoff Plate Theory. *In IN-TECH 2017 International Conference on Innovative Technologies.*